Spring 2017

Studies into the structure and function of various domains of obscurin and titin

Rachel A. Policke
James Madison University

Studies into the Structure and Function of Various Domains of Obscurin and Titin

A Project Presented to

The Faculty of the Undergraduate

College of Chemistry and Biochemistry

James Madison University

In Partial Fulfillment of the Requirements

For the Degree of Bachelor of Sciences

By Rachel A. Policke

April 2017

Accepted by the faculty of the Department of Chemistry and Biochemistry, James Madison University, in partial fulfillment of the requirements for the Degree of Bachelor of Sciences.

FACULTY COMMITTEE:

Project Advisor: Nathan T. Wright, Ph.D Date
Assistant Professor, Chemistry and Biochemistry

Reader: Christopher E. Berndsen, Ph.D Date
Assistant Professor, Chemistry and Biochemistry

Reader: Isaiah Sumner, Ph.D Date
Assistant Professor, Chemistry and Biochemistry

HONORS PROGRAM APPROVAL:

Bradley Newcomer, Ph.D Date
Dean of the Honors College, Honors Program

Table of Contents

List of Tables and Figures

Acknowledgements

I would like to thank Dr. Nathan Wright, Dr. Christopher Berndsen, and Dr. Isaiah Sumner for serving on my senior project committee as well as for all of their help and guidance in writing and editing my senior project. Additionally, I would like to extend thanks to Dr. Nathan Wright for guidance in my four years of undergraduate research, Dr. Christopher Berndsen for help with crystallography, and Dr. Isaiah Sumner for help with simulations, as well as the entire James Madison University Department of Chemistry and Biochemistry for their support and use of instrumentation. This work was supported by the Jeffress Memorial Trust J-1041 (to NTW), Research Corporation 22450 (to NTW) and James Madison University startup funds (to NTW, CEB, and IS).

Abstract

Muscles give our bodies the ability to move by stretching and contracting. While contraction is accomplished by the well-known actin-myosin interaction, not much is known about stretch. Two integral muscle proteins involved in stretch are titin and obscurin; both are long rope-like protein molecules that seem to act as molecular springs. Mutations in these two proteins can lead to diseases such as hypertrophic cardiomyopathy and muscular dystrophy, as well as a variety of cancers. In an effort to understand muscle stretch and signaling on a more fundamental level, here we present the high resolution structure of obscurin Ig59, a domain involved in titin/obscurin binding. We also describe how unbound titin moves when stretched. Last, we describe ongoing work in elucidating the high-resolution structures and activation/inhibition mechanisms of obscurin domains Rho-GEF, Rho-GEF-PH, kinase I (KI), and kinase II (KII).

Preface/Introduction

Muscles, Muscle Proteins, and Structure of the Sarcomere

Muscles give our bodies the ability to move by stretching and contracting. Without them, we would not be able to walk, stand up, or perform any of the motions do throughout our daily lives. Striated muscles, the ones connected to our skeleton, allow for virtually all voluntary movement of our body. As the name implies, this kind of muscle is made up of a series of different bands that are visible in the light microscope, termed the A-band and the I-band. One A-band and half of the neighboring I-band form the sarcomere, the smallest contracting segment of muscle. Hundreds of sarcomeres lie end-to-end, making up the syncytial cell type called the myofibril. These cell types are the largest in the human body; the longest can be more than a foot long. Many myofibrils are bundled together into a single fascicle, which in turn is bundled into a muscle (Fig. 1).

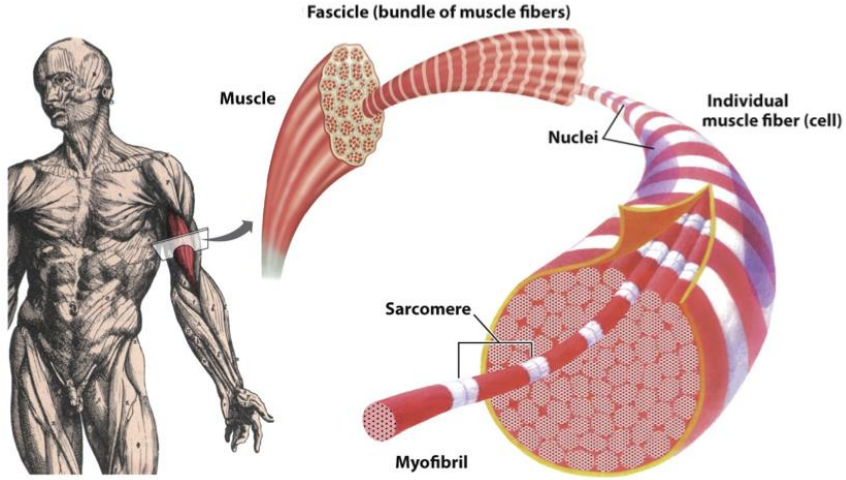

Figure 1. Schematic representation of the muscle, showing its breakdown into fascicles, fibers, and sarcomeres (adapted from John Wiley & Sons, Inc., 2013).

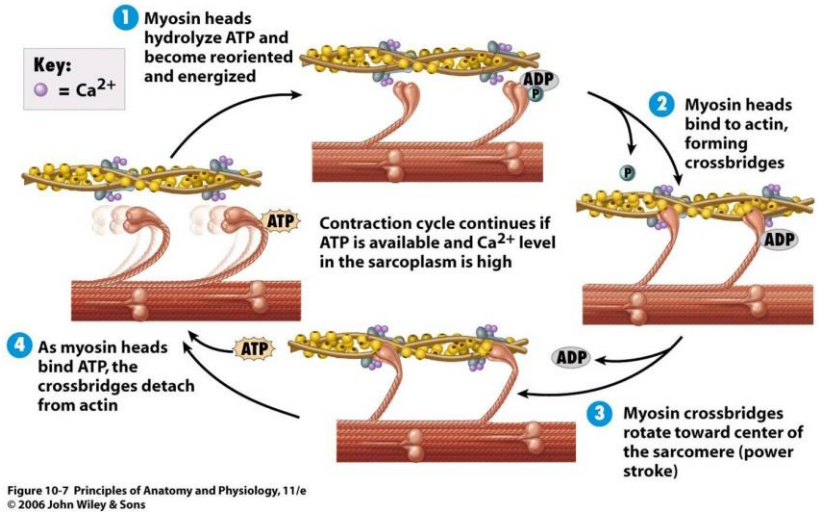

Figure 2. Steps of muscle contraction showing the process of calcium release and binding to troponin, conformation changes of troponin and tropomyosin, hydrolysis of ATP, power stroke, binding of ATP to myosin, and release of bound calcium from troponin (taken from https://mykindofscience.com/2015/01/20/my-awe-of-the-human-body-muscle-movement-2/).

When a muscle contracts, myosin thick filaments slide across F-actin thin filaments in an ATP- and calcium-requiring reaction, resulting in a shortening of the sarcomere. This process, termed the sliding filament model, involves a number of simple steps to produce contraction. When the brain generates an electrical signal in the form of an action potential, it courses along through the somatic nervous system to the axon of a motor neuron, which is connected to a skeletal muscle cell. Acetylcholine is released by neurotransmitters within the

synaptic cleft, which binds to membrane proteins in the outer layer of the muscle cell, depolarizing it. This depolarization allows the action potential to travel into the cell and activate Ryanodine receptor-dependent calcium channels within the sarcoplasmic reticulum. Calcium ions flow into the muscle cell as a result and bind to troponin in the thin filament region of the muscle cell. The calcium binding induces a conformation change in the troponin protein, which in turn alters the tropomyosin-actin interaction. The new conformation of tropomyosin exposes the myosin binding sites on actin (the thin filament). Once the myosin binding sites are exposed, head structures on the myosin molecules hydrolyze bound ATP and reorient to bind to actin. Finally, release of ADP and P_i from the myosin head generates a power stroke (Fig. 2, steps 1 and 2) that brings adjacent Z lines closer to each other, shortening the length of the sarcomere and contracting the cell (Fig. 2, step 3. The cell returns to a relaxed state when ATP binds to myosin and the calcium ion bound to troponin is released (Fig. 2, step 4).

In order for these ultrastructural filaments to perform their jobs and contribute to overall muscle contraction, the sarcomere must be exquisitely well ordered. If the thick filaments did not interdigitate the thin filaments, there would be no contraction. Similarly, if the thick and thin filaments did not overlap, there would be no power stroke. The almost paracrystalline-like array of contractile apparatus is accomplished through the cytoskeleton; particularly, through the involvement of the giant cytoskeletal proteins titin, nebulin, and obscurin.

Titin, the longest known polypeptide at 3-5 MDa, has its N- and C-termini anchored in the Z-disc and M-line, respectively. Titin generates passive elasticity of muscles by acting as a force sensor and regulates the length of the thick filament of the sarcomere (Trinick, 1992; Hsin *et al.*, 2011; Fig. 3, red). Throughout its considerable length, it binds to and anchors many proteins to the surrounding cytoskeleton and acts as a molecular spring, regulating amount of stretch in the sarcomere. Nebulin (600-800 kDa) stabilizes the thin filament and may also have some function in regulating the length of the thin filament, directing actin/myosin interactions, and myofibrillar force generation (Trinick, 1992; Chu *et al.*, 2016; Kontrogianni-Konstantopoulos *et al.*, 2009). Last, obscurin connects the sarcomere to the surrounding sarcoplasmic reticulum via its interaction with titin (Fig. 3) and aids in assembly of myofibrils and the sarcoplasmic reticulum (Meyer and Wright, 2003; Lee *et al.*, 2010; Bang *et al.*, 2001; Young *et al.*, 2001; Armani *et al.*, 2006; Kontrogianni-Konstantopoulos and Bloch, 2009). Obscurin and titin are the focus of my research.

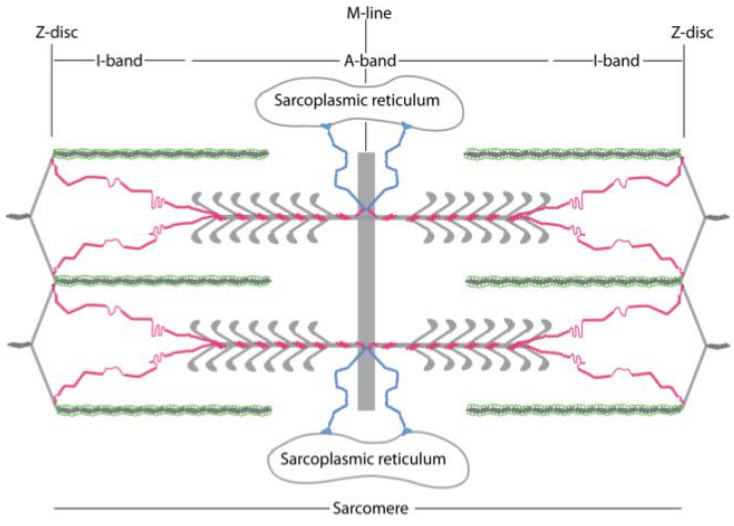

Figure 3. Schematic representation of the sarcomere. Titin (red) anchors the M-line and Z-disc and regulates the length of the sarcomere. Obscurin (blue) tethers titin to the sarcoplasmic reticulum. Nebulin (green) regulates the length of the thin filaments (actin, under the green). Myosin heads (grey) slide across the thin filaments as a muscle contracts (taken from Meyer and Wright, 2013).

Due to their large size and complexity, titin and obscurin have been difficult to study using traditional molecular biology or biochemistry techniques. However, both are highly modular in overall architecture. Titin has approximately 300 independently folded domains while obscurin has at least 70, though the exact number depends on the isoform; each domain of titin consists of approximately 100 amino acids (Meyer and Wright, 2013). The most common folds are the immunoglobulin (Ig) and Fibronectin typeIII-like (FnIII-like) domains, which both fold into variations of a β-sandwich fold.

(Meyer and Wright, 2003; Fig. 4). Rather than trying to discern structure/function relationships of the entire obscurin or titin molecule, we (and others) have instead found it more useful to focus on solving the high-resolution structure of individual domains. In other words, we choose to describe the obscurin and titin structure/function relationship from a bottom-up approach, from domains to whole molecules. To this end, I will begin with an overview of titin and obscurin, their associated diseases and then move onto a more in-depth discussion of obscurin.

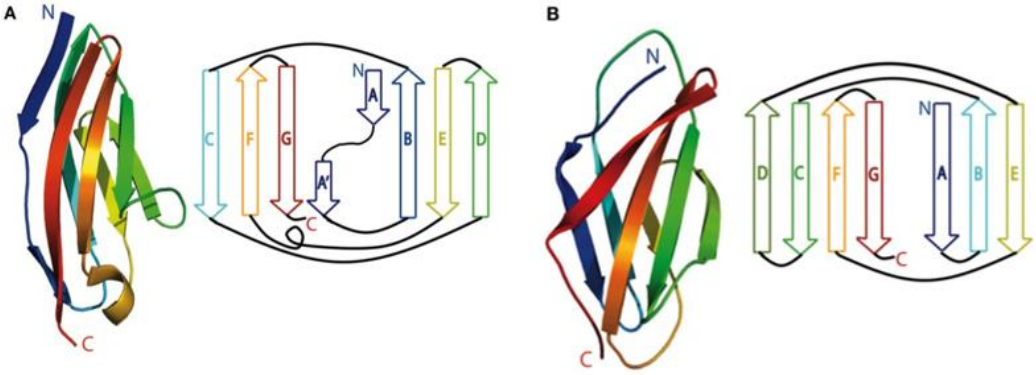

Figure 4. Cartoon representation and schematic of A.) an Ig domain and B.) a FnIII-like domain. The cartoon representations are colored from N-terminus (blue) to C-terminus (red) (adapted from Meyer and Wright).

Titin is found mostly in skeletal and cardiac muscle tissue and spans the sarcomere from the Z-disk to the M-band (Bang *et al*., 2001; Granzier and Wang, 1993; Linke, 1994; Kontrogianni-Konstantopoulos *et al*., 2009). In the body, titin regulates the length of the sarcomere and helps restore the pre-contraction length, protecting the sarcomere from injury caused by overstretching (Lee *et al*., 2010). Titin's ability to both stretch and recoil is fundamental in preventing muscle overstretching, and helps myocytes return to their original length (Gautel, 2011; Improta *et al*. 1998). In this capacity, titin acts as a mechanosensor (Kontrogianni-Konstantopoulos *et al*., 2009; Linke 2008; Meyer and Wright, 2003).

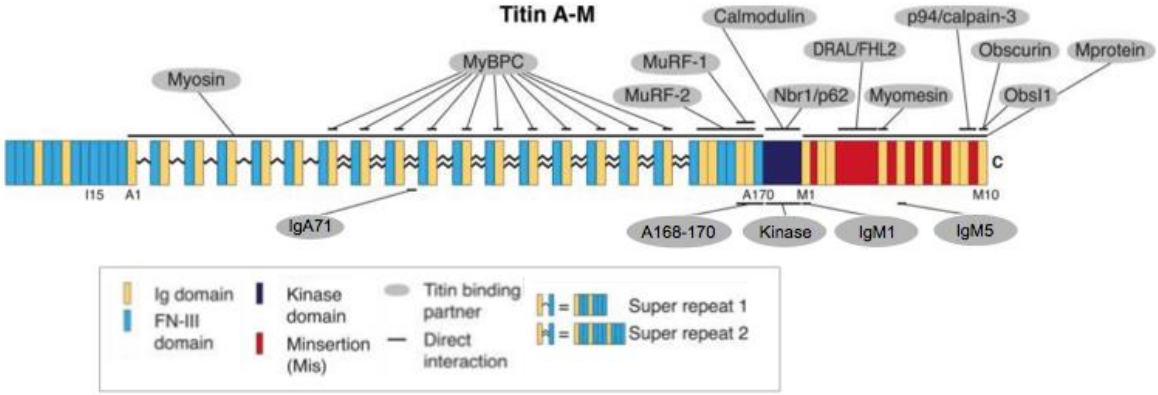

Figure 5. Schematic representation of the structure and binding partners of titin A-M (the portion of titin spanning from the A-line to the M-line). Note that the key provided lists the domain types as well as the meaning of the colors and shapes used in the schematic (adapted from Kontrogianni-Konstantopoulos, 2009).

A decidedly important player in muscle contraction, titin has a multitude of binding partners, one of which is obscurin (Fig. 6). Obscurin (~720-900 kDa) is made up of mostly Ig domains and binds to titin in the Z-disk region of the sarcomere (Young *et al*., 2001; Bang *et al*., 2001) (Fig. 5&6). With titin bound at its N-terminus and small ankyrin bound at its C-terminus, obscurin effectively connects titin to the sarcoplasmic reticulum (Bang *et al*., 2001; Young *et al*., 2001; Armani *et al*., 2006; Kontrogianni-Konstantopoulos *et al*., 2009) (Fig. 6).

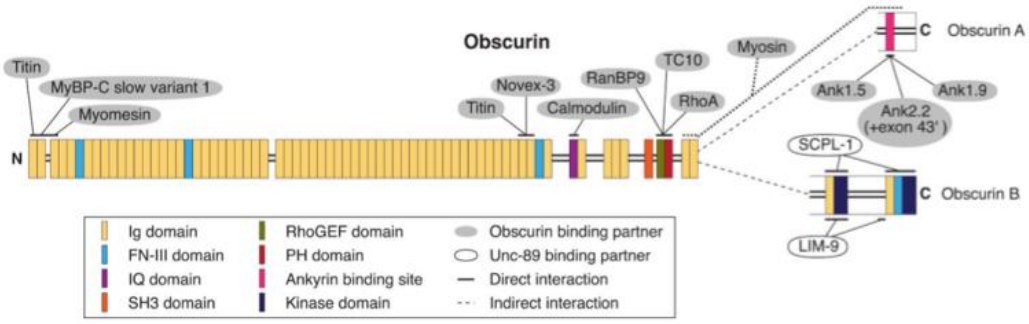

Figure 6. Schematic representation of the structure and binding partners of the two main isoforms of obscurin, isoforms A and B. Note that the key provided lists the domain types as well as the meaning of the colors and shapes used in the schematic (adapted from Kontrogianni-Konstantopoulos, 2009).

The *OBSCN* gene is located on human chromosome 1q42 (Fukuzawa *et al*., 2005). Obscurin A is encoded by this gene and all other obscurin isoforms result from alternative splicing of this gene (Russell *et al.*, 2002; Fukuzawa *et al*., 2005; Kontrogianni-Konstantopoulos *et al*., 2009). Obscurin is found mostly in skeletal and cardiac muscle tissue, though it has also been found in the brain and in breast epithelial tissue (Nagase, 2000 (1-3); Stroka *et al*., 2016; Perry *et al*., 2014; Shriver *et al*., 2016). The two largest, muscle-specific isoforms are obscurin A (~720 kDa) and obscurin B (~870 kDa). These two isoforms differ only at the C-terminus: obscurin has a non-modular C-terminus with binding sites for small adaptor proteins called ankyrin and obscurin B has adhesion motifs superseded by two terminal serine-threonine kinases (Ackermann *et al*., 2014; Fukuzawa *et al*., 2005). Obscurin B has more signaling moieties and, because obscurin has been known to directly phosphorylate substrates in the body, this lab uses obscurin B in its experiments (Shriver *et al*., 2016; Perry *et al.*, 2014; Hu and Kontrogianni-Konstantopoulos, 2013).

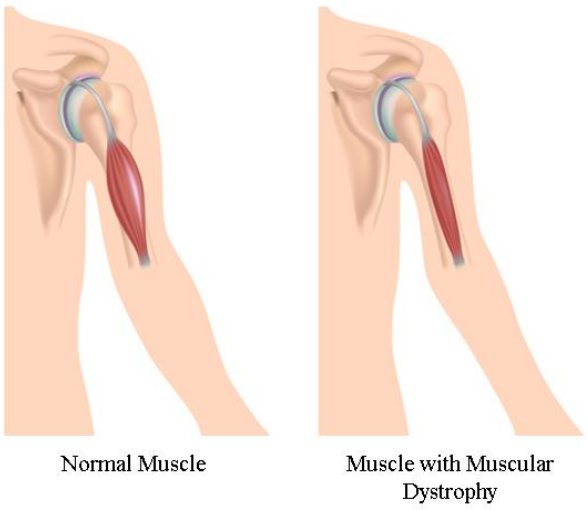

Figure 7. Normal muscle (left) next to a muscle with muscular dystrophy (right). In the muscle with MD, the muscle had begun to atrophy and is smaller in mass.

Mutations in the regions close to obscurin/titin interactions are associated with pathogenesis of muscle diseases, namely muscule wasting diseases such as muscular dystrophy (MD) (Hackman *et al*., 2002; Zheng *et al.*, 2015) and malformed muscle diseases like hypertrophic cardiomyopathy (HCM) (Satoh *et al.*, 1999; Fukuzawa *et al.*, 2005). MD is a group of inherited diseases in which muscles become damaged and progressively weaken. As a result, the body is unable to increase muscle mass or repair damaged muscle and the muscle may eventually die (Fig. 7). Affected muscles can include skeletal and cardiac muscles, which can lead to problems with posture, ambulation (walking), cardiac, and respiratory function (McNally and Pytel, 2007). HCM, on the other hand, is characterized by a left ventricular hypertrophy with diastolic dysfunction, all of which are caused by mutations in genes that code for proteins in the Z-band of the sarcomere (Arimura *et al*., 2006; Frenneaux, 2004). In HCM, there is an asymmetric accumulation of poorly functioning, enlarged, cardiomyocytes, specifically in the left ventricle, which results in a constricted, generally malfunctioning heart (Fig. 8; Elliot and McKenna,

2004; Teekakirikul *et al*., 2012). HCM accounts for 1% of annual mortality rates and can cause death from sudden cardiac death, heart failure, or stroke (Frenneaux, 2004).

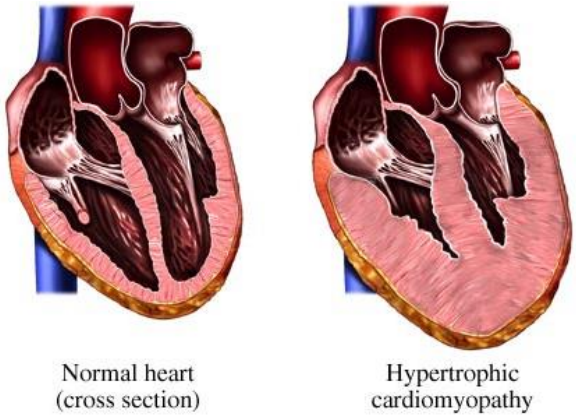

Figure 8. Normal heart (left) next to a heart with hypertrophic cardiomyopathy (right). In the heart with HCM, the cardiac muscles have enlarged and decreased the area available for blood to flow.

Obscurin mutations and pathogenesis of muscle diseases are not as well studied as their counterparts in titin. In fact, only a single study involving a single example has been published (Arimura *et al.,* 2007). In this study, the R8 to Q8 (Arg4344Gln) mutation in Ig58 was linked to HCM. This mutation occurs in the *OBSCN* gene in the region of that codes for the titin/obscurin binding site and, as such, causes a decreased binding affinity of obscurin to titin (Arimura *et al*., 2007; reviewed in Kontrogianni-Konstantopoulos *et al.,* 2009). In an unpublished study, a single mutation in obscurin was linked to MD: R16 to W in Ig59 (Rossi *et al*., submitted).

X-Ray Crystallography

In order to understand the causes of these diseases on the molecular level, the wild-type and mutated structures of these individual domains must be studied, elucidated, and compared. High resolution structures of individual domains can be determined via nuclear magnetic resonance (NMR) spectroscopy and X-ray crystallography.

X-ray crystallography first requires the growth of a single protein crystal, a periodic assembly of protein molecules held together in a regularly-repeating lattice network by weak molecular forces (Rupp, 2010). This can be accomplished through methods such as hanging drop vapor diffusion, sitting drop, or microbatches (Rupp, 2010; Dessau and Modis, 2011). Once the crystals are grown, they are harvested and kept frozen until data collection, generally by use of a synchrotron. The structure of the repeating units within the crystal can be determined by analyzing the diffraction of high energy electromagnetic radiation by the electron density within the crystal lattice in the form of the crystal's X-ray diffraction pattern. When X-ray photons encounter these electrons, they are scattered at specific angles, whose points or positions can be interpreted as reflections from sets of discrete lattice planes. This is partially because the X-ray wavelength used is comparable to the interatomic distances in the molecules studied (Wladawer *et al.,* 2013). The angle of scattering is related to the distance between planes h, k, and l by Bragg's law, given below.

$$n\lambda = 2d_{hkl}\sin\theta$$

In which d_{hkl} is the lattice plane spacing, n is the order of reflection, and θ is the scattering angle.

The scattering function (f_s or F_s) can give the approximate X-ray scattering of an entire system where F_s depends on the direction of scatter and, therefore, on the angle of scatter. For a single atom, the X-ray scattering is very small and is given by:

$$F_s = \int_r^{V(atom)} \rho(r) e^{2\pi S r}\, dr$$

In which ρ(r) is the electron density, r is the position of an electron in the atom, S is the scattering vector— the difference between the incoming and scattered wave vectors— and V(atom) is the volume of the atom. For a larger, repeating structure such as a molecular crystal lattice, the scattering function is described as a sum of the scattering functions of individual atoms:

$$F_s = \sum_{j=1}^{atoms} f_{s,j}^0 \, e^{2\pi i S r j}$$

In which F_s is the scattering function of the crystal and f_s^0 is the atomic scattering factor.

The X-ray diffraction pattern can also be interpreted as transforming the crystal structure's electron density from real space $\mathbb{R}$ (x, y, z) to reciprocal space $\mathbb{R}^*$ (h, k, l). In reciprocal space, the scattering function of a molecular crystal becomes:

$$F_h = \sum_{j=1}^{atoms} f_{s,j}^0 e^{2\pi i h x j}$$

In which F_h is the scattering function in terms of the index vector h, x denotes the position of an atom/electron in an atom in fractional coordinates, and, by extension, x_j denotes the position of the jth atom/electron (Rupp). Such a transformation from real to reciprocal space is termed a Fourier transform and can be generalized with the form:

$$F(k) = \int_{-\infty}^{\infty} G(x) e^{2\pi i k x} dx$$

a complex Fourier integral, derived as an eigenfunction of the Sturm-Liouville eigenvalue problem with periodic boundaries (Rupp, 2010). There is an inverse relationship between the spacing of reflections in a diffraction pattern and the spacing in the original crystal lattice, which can be used to establish the dimensions of a unit cell within the crystal lattice (Rhodes, 2006).

The points of a diffraction pattern give the relative intensities of scattering as well as the position. Because the structure of the unit cells of a crystal repeats periodically to form a lattice, the incoming photon waves that scatter as a result of an electron cloud encounter each other and can interfere constructively, destructively, or partially, resulting in an enhancement or quenching of X-ray radiation that is depending on the direction of the wave vector (Wlodawer *et al*., 2008; Wlodawer *et al*., 2013). These intensities are related to the complex structure factor (F) in the following way:

$$I = FF^* = |F|^2$$

Because F is a wave equation, it must specify the frequency, amplitude, and phase of each diffracted ray (Rhodes, 2006). But, in calculating the amplitude of the structure factor to gain information about the intensities of a reflection, all information about the phase angle of each reflection is lost. This significantly encumbers the reconstruction of molecular structure, which requires an understanding of the phases of a reflection (Rupp, 2010). The remedy to this problem will be discussed later.

The size of the unit cell of a crystal lattice is directly proportional to the number of diffracted beams, and, therefore, is directly proportional to the number of reflections and reflection intensity observed. Also, due to the symmetric nature of crystals, multiple individual measurements of intensity are expected to calculate the same, unique reflection and contribute

to a certain redundancy or multiplicity factor. The higher the multiplicity factor, the more accurate the average reflection intensity, since all individual reflections have an innate degree of random error (Wlodawer *et al*., 2013). The value R_{merge} reports the agreement of all symmetry-equivalent reflections that contribute to the same unique reflection and is given by:

$$R_{merge} = \sum_h \sum_i \left| < I_h > - I_{h,i} \right| \sum_h \sum_i I_{h,i}$$

In which h represents the unique reflections, i represents the symmetry-equivalent contributors to each unique reflection, and $< I_h >$ represents the average intensity of each reflection (Wlodawer *et al*., 2013; Wlodawer *et al.*, 2008). In other words, R_{merge} compares the average intensity of the original model with the intensity of the current model and therefore is an indicator of bias, and, consequently, potential inaccuracies. R_{merge} can also be written as:

$$R_{merge} = \frac{\sum_h \sum_{i=1}^{N} \left| I_{h,i} - < I_h > \right|}{\sum_h \sum_{i=1}^{N} I_{h,i}}$$

In which N represents all redundant measurements for each individual reflection h (Rupp, 2010). Ideally, a high-quality diffraction pattern would have an R_{merge} of ≤5% (Wlodawer *et al*., 2013; Wlodawer *et al.*, 2008). However, in reality, the R_{merge} may be slightly higher, though it is generally less than 20% for large biomolecules (Rupp, 2010). Additionally, the signal to noise ratio, $< I/\sigma(I) >$, is defined as:

$$< \frac{I}{\sigma(I)} > = \frac{1}{N} \sum_h^N \frac{I_h}{\sigma(I_h)}$$

Where an acceptable range of $< I/\sigma(I) >$ is ≤1.5-2.0 (Rupp, 2010).

In short, from the diffraction pattern, it is possible to gain the positions and intensities of individual reflection but not their phases. The inability to garner phases from diffraction data gives rise to the 'phase problem' of crystallography. Phases can be supplied by other means, such as isomorphous replacement, anomalous scattering, and molecular replacement. The research in this thesis was conducted using molecular replacement.

Molecular replacement uses the phases and structure factors from previously solved, similar protein structures, called phasing models, to obtain the phases of the target protein. For example, most if not all immunoglobulin domains are comprised of very similar structures (see Fig. 6). Therefore, it is feasible to use phases from other immunoglobulin domains to estimate the phases of an unsolved immunoglobulin domain; generally an immunoglobulin phase model requires a minimum of 30% sequence identity (Scapin, 2013; Chothia and Lesk, 1986). In this case, the two structures are isomorphous, or share the same crystal structure. The electron density, $\rho(x, y, z)$, of the target structure can be calculated from those of the isomorphous phasing models by the following equation:

$$\rho(x, y, z) = \frac{1}{V} \sum_h \sum_k \sum_l \left| F_{h,k,l}^{target} \right| e^{-2\pi i(hx+ky+lz-\alpha')}$$

In which V is the volume of the unit cell, $F_{h,k,l}^{target}$ is the amplitudes of the scattering function of the target protein, α' is the phases of the model, and the frequencies h along the x-axis, k along the y-axis, and l along the z-axis are given by hx, ky, and lz, respectively (Rhodes, 2006). Using the above equation, the electron density for the entire structure can be obtained giving a map of

the overall structure. To this, the target sequence of amino acids can be fit, giving a model of the overall structure. Given that the first output map will be crude, because the phases of the model are only rough estimates, both the map and model will require iterative manual and computational improvement. However, due to the implementation of the phasing model, a great potential for bias was also introduced— that the calculated phases from the model, rather than the observed phases from the experimental intensities, would dominate the outputted map. To prevent model bias, a new map can be generated by obtaining a contour in which the calculated structure factor amplitudes ($|F_{calc}|$) are subtracted from multiple observed structure factor amplitudes ($n|F_{obs}|$):

$$\rho(x,y,z) = \frac{1}{V}\sum_h\sum_k\sum_l(|F_o| - |F_c|e^{-2\pi i(h_x+k_y+l_z-\alpha'_{calc})}$$

In which α'_{calc} is the phases of the model. The map generated from the previous equation is known as a $F_o - F_c$ map or basic difference map and gives regions of positive and negative densities that require moving atoms towards or away from the regions, respectively (Rhodes, 2006; Rupp, 2010). An amino acid in an unfavored conformation according to the $F_o - F_c$ map will have negative density at its current conformation and positive density nearby, where its preferred conformation would fit.

$F_o - F_c$ maps rely solely on the original data and eliminate bias from the current model so that the errors in it can be determined. Since $F_o - F_c$ maps point out the errors of the current model, it is often not useful for the beginning stages of reconstruction, when there are more errors, because the output is 'noisy' and difficult to read. Therefore, a $2F_o - F_c$ map or combined difference map is more often used, which allows a greater influence from the model but gives a more easily understood map. $2F_o - F_c$ maps are given by:

$$\rho(x,y,z) = \frac{1}{V}\sum_h\sum_k\sum_l(2|F_o| - |F_c|e^{-2\pi i(h_x+k_y+l_z-\alpha'_{calc})}$$

Through the process of model and map refinement, the particular conformation(s) of each amino acid will be found and corrected through adjustment of variables such as clash scores and χ and ϕ angles, definition of the electron density map, and decrease R-factor values, which are defined as:

$$R_{factor} = \frac{\sum_h\sum_k\sum_l|F_{obs} - F_{calc}|}{\sum_h\sum_k\sum_l F_{obs}}$$

There are a variety of R-factors, including the linear merging R value, R_{merge}, defined previously, which compares the average intensity of the original data and current model, and the cross validation R value, R_{free}, which is calculated the same as the normal R-factor but only for approximately 10% of the original data points. R_{free} is given by:

$$R_{free} = \frac{\sum_{h\epsilon free}|F_{obs} - kF_{calc}|}{\sum_{h\epsilon free}F_{obs}}$$

Where $h\epsilon free$ denotes the excluded cross-validation set (Rupp, 2010). A high-resolution crystal structure is defined by an $R_{free} < 20\%$, a resolution of 0.86–1.5 Å, and an $R_{merge} <$ ~4%, though, practically, these values may deviate (Wlodawer *et al.*, 2008). At this point, a structure is considered 'done' and can be published.

In this work, the high resolution structure of obscurin Ig59 was obtained. Work is in progress for the elucidation of high resolution structures of obscurin domains Rho-GEF, Rho-GEF-PH, kinase I (KI), and kinase II (KII).

A Variant in the Obscurin Gene Associated with a Frameshift Mutation in the Filamin C Gene in a Family with Distal Muscular Dystrophy*

*This chapter is based on a manuscript that has been submitted to PLoSONE. The writing of this chapter was a joint effort between our lab and our collaborators in Italy.

Introduction

Distal muscular dystrophies are a group of inherited primary muscle disorders showing progressive muscle atrophy and weakness, usually in the hands and/or feet (Mutoni and Wells, 2007; Ng *et al.*, 2012; Sewry, 2010; Udd, 2012). These dystrophies have diverse etiologies, and are further classified via one of four methods: i) clinical features, i.e. early or late adult onset, onset in the hands or feet; ii) magnetic resonance imaging (MRI)-based evidence of an involvement of the anterior or posterior compartment of the legs; iii) inheritance pattern; and/or iv) histopathological findings (Udd, 2012; Mastaglia and Laing, 1999). Here we will use a combination of all four classification schemes to describe a new gene member (obscurin) that appears to be autosomally-linked with late onset of distal muscular dystrophy (see Table 1 for a complete list of other genes involved).

Table 1. Classification and genes associated with distal muscular dystrophies.

Type of Distal Muscular Dystropy	Associated Gene
Autosomal Dominant: Late Onset	
TIA1 Mutated Welander Distal Myopathy	TIA1
Titin Mutated Tibial Muscular Dystropy	TTN
Distal Myotilinopathy	MYOT
ZASPopathy	LDB3
MATR3 Mutated VCPDM	MATR3
VCP Mutated Distal Myopathy	VCP
aB-crystallin mutated distal Myopathy	CRYAB
Thenar Atrophy with Sarcoplamic Bodies	FHL1
Mutated Distal Myopathy	SQSTM1
Autosomal Dominant: Adult Onset	
Desminopathy	DES
ABD-FLNC Mutated Distal Myopathy	ABD-FLNC
DNAJB6 Mutated Distal Myopathy	DNAJB6
HSPB8 Mutated Neuromyopathy	HSPB8
Finnish MPD3	No known gene
Oculopharyngeal Distal Myopathy	No known gene
Autosomal Dominant: Childhood Onset	
Distal Myosinopathy MYH7	MYH7
KLHL9 Mutated Distal Myopathy	KLHL9
Autosomal Recessive: Early Adult Onset	
Miyoshi Dysferlinopathy	DYSF
Distal Anoctaminopathy	ANO5
GNE Myopathy	GNE
Recessive Distal Titinopathy	TTN
Autosomal Recessive: Childhood Onset	
Distal Nebulin Myopathy	NEB
ADSSL Mutated Distal Myopathy	ADSSL1
Oculopathyngeal Distal Myopathy	PABPN1

In contrast with proximal muscular dystrophies, in which the mutated genes often encode sarcolemmal proteins, many of the genes identified in distal muscular dystrophies encode proteins associated

with the contractile apparatus and Z-disk of the sarcomere (Udd, 2012; Udd, 2001). Both dominant and recessive mutations in the titin gene *(TTN)* have been associated with human distal dystrophies (Evilä, 2014). Titin is the largest protein of the sarcomere extending from the Z-disk to the M-line. A number of sarcomeric and signalling proteins interact with titin (Gautel, 2011). Among these, obscurin, another giant myofibril-associated protein, interacts with titin at both the M-band and the Z-disk (Chauveau *et al*., 2014; Young *et al.*, 2001; Fukuzawa *et al.*, 2008; Gautel and Djinović-Carugo, 2016; Rudloff *et al.,* 2015). Mutations in the M10 domain of titin, which binds the Ig1 domain of obscurin, cause tibial muscular dystrophy (TMD) or Udd myopathy in the heterozygous state and limb girdle muscular distrophy 2J in the homozygous state. These mutations ablate the interaction between titin and obscurin at the sarcomeric M-band and have been proposed to cause a gradual decline in sarcomere stability (Fukuzawa *et al.,* 2008; Pernigo *et al.,* 2010). Oddly, no mutations in the Ig1 domain of obscurin have been reported so far. Obscurin and titin also interact in the Z-disk, at the Ig58/59 domains of obscurin and the Z9/Z10 domains of titin. Moreover, the obscurin variant p.Arg4344Gln, located in the obscurin Ig58 domain, was identified as the likely cause of hypertrophophic cardiomyopathy (HCM) in a Japanese patient (Arimura *et al.,* 2007). This mutation weakens the binding of obscurin to titin, thus suggesting that interactions between these two proteins are critical for optimal sarcomere stability and muscle contraction. In a competing line of evidence, knock-in mice carrying the p.Arg4344Gln variant develop HCM following trans-aortic constriction intervention (Hu *et al.,* 2017, under review). However these studies suggest other molecular mechanisms than ablation of the canonical titin-obscurin interaction. More recently, additional *OBSCN* mutations have been associated with dilated cardiomyopathy (Marston *et al.,* 2015). Finally, knockout mice for the *OBSCN* gene present an altered localization of ankyrin B and dystrophin at costameres that is paralleled by increased sarcolemmal fragility and reduced ability to complete intense running sessions (Randazzo *et al*., 2013). Following heavy exercise, the diaphragm muscle of these mice presented inflammation and hyper-contractures with evidence of wavy and less defined M-band and H-zone (Randazzo *et al.,* 2017). Together, these studies present significant circumstantial evidence that obscurin mutations are linked to muscular dystrophies.

In this current study, we propose a new obscurin mutant that is more directly associated to dystophies. However, this study cannot offer a direct link between obscurin and muscular dystrophy due to a second gene also being mutated in the human cohort studied by our group. This second gene, encoding filamin C (*FLNC*) is linked to myopathies inherited as a dominant trait, which may present with different clinical and histological features (Duff *et al*., 2011; Guergueltcheva *et al.,* 2011; Kley *et al.,* 2012). Patients with *FLNC* mutation have progressive proximal muscle weakness associated with the presence of aggregates of desmin and myotilin, among other proteins within myofibers, thus resembling typical profiles of myofibrillar myopathy (Kley *et al.,* 2012). Interestingly, a non-myofibrillar myopathy with distal muscle involvement has been reported in three related families from Bulgaria carrying a frameshift deletion in *FLNC* (c.5160delC). This mutation was not only detected in all patients of these families, but also in some healthy relatives (Guergueltcheva *et al.,* 2011). Thus, the deletion appears to result in a loss-of-function mechanism leading to haploinsufficiency with absence of protein aggregates.

Based on the evidence that i) *OBSCN* ablation results in structural and functional alterations of skeletal muscles in mice, ii) mutations in the obscurin binding domain of titin domain M10 are causative of TMD and LGMD2J, and iii) mutations in *OBSCN* have been reported in patients with cardiomyopathy, we investigated whether mutations in *OBSCN* could be also involved in skeletal muscle diseases. Our collaborators performed a mutation screening of the *OBSCN* exons encoding the sites of interaction between obscurin and titin at both M-

band and Z-disk in patients affected by distal muscular dystrophy. This screening identified an *OBSCN* c.13330C>T mutation, resulting in a p.Arg4444Trp substitution in the obscurin Ig59 domain. This mutation segregates with muscular dystrophy in a French family. Whole exome sequencing (WES) of this family by our collaborators identified an additional single base deletion in the *FLNC* gene (c.5161delG) causing a frameshift mutation (p.Gly1722ValfsTer61). However, segregation analysis indicated that this *FLNC* mutation did not completely segregate with the disease, as the mutation was also present in one healthy relative. These findings resemble the results previously reported by Guergeltcheva and collaborators (Guergueltcheva *et al.,* 2011), where a deletion in the *FLNC* gene (c.5160delC) was observed in individuals with muscular dystrophy and also in healthy individuals. WES analysis performed on the DNA from four patients, three with the disease and one healthy, from several Bulgarian families in which the *FLNC* c.5160delC was described and did not reveal any additional gene variant shared by affected individuals. Based on our collective findings, we propose that the OBSCN p.Arg4444Trp variant may increase the penetrance of the *FLNC* c.5161delG deletion in the French family. Accordingly, variants in the *OBSCN* gene should be considered as potentially causative of muscular dystrophy, alone or in association with variants in other myopathy genes.

Materials and Methods

Patient Data.† Mutation screening was initially performed in families where the affected members presented with a clear distal myopathy phenotype transmitted as dominant trait. The study was then extended to a cohort of 110 unrelated patients consisting of 11 cases with predominantly proximal muscle weakness, respiratory failure and/or cardiomyopathy, 8 cases with predominantly proximal myopathy, 26 cases with initial distal muscle involvement subsequently progressing to proximal limb weakness, and 65 cases of patients with a clinical history of uncharacterized muscular dystrophy/myopathy. In the French family reported here, the proband (III:3), a woman issued from non consanguineous parents, and her second son (IV:2), had progressive distal lower limb weakness starting at ages 30 and 14, respectively. The proband's father (II:2) had very late-onset walking difficulties, became wheelchair bound at age 75 and subsequently died from respiratory insufficiency and pneumonia. The paternal grandfather (I:1) also became wheelchair-bound at an advanced age. Other family members had no neuromuscular history. The proband and her affected son were followed in Neuromuscular Unit of Salpêtrière Hospital (Paris, France). Among the four children of the proband, one daughter (IV:3) and one son (IV:4), seen at the Neuromuscular Unit at age of 33 and 32, respectively, had a normal clinical examination, with no muscle alteration as shown by MRI.

Ethics committee approval and written informed consent was obtained for all patients. This study complies with the ethical standards stated in the 1964 Declaration of Helsinki.

Mutation Screening and Genotyping.† Mutation screening by conventional Sanger sequencing on specific regions of *OBSCN* was performed in all family members for whom DNA was available. In detail, primers were designed using Primer3 software (http://frodo.wi.mit.edu/primer3) to amplify *OBSCN* exon 2 (coding for the Ig1) and exons 50, 51 and 52 (coding for the Ig58/59 domains), according to sequence NM_052843. Genomic DNA was extracted from peripheral blood leucocytes by standard procedures (Kley *et al.*, 2012). Amplified DNA fragments were directly sequenced using an ABI Prism 310 apparatus (Applied Biosystem). Alternatively, Sanger sequencing was performed using DreamTaq™ DNA Polymerase (Thermo Scientific) according to standard protocol and PCR products were

†Work of Dr. Vincenzo and collaborators

sequenced on an ABI3730xl DNA Analyzer (Applied Biosystems), using the Big-Dye Terminator v3.1 kit and analyzed with Sequencher 5.0 software (Gene Codes Corporation). DNA mutation numbering was based on cDNA reference sequence (NM_052843), taking nucleotide +1 as the A of the ATG translation initiation codon. The mutation nomenclature used follows that described at http://www.hgvs.org./mutnomen/.

Whole Exome Sequencing (WES).† Whole exome sequencing (WES) was performed on patients III:3 and IV:2 at ATLAS Biolabs GmbH using SeqCap EZ Human Exome Library v2.0 (Roche NimbleGen) for DNA capture. The enriched DNA was sequenced with an Illumina HiSeq 2000 platform, 2 x 100 bp. Reads were aligned to the human genome reference GRCh37/hg19 with Burrows-Wheeler Aligner and duplicate reads were removed with Picard. The Genome Analysis Toolkit was used to realign the reads, recalibrate base quality scores and call variants. Variants were annotated using wAnnovar and variants with frequency more than 1% in the 1000 Genomes or Exome Sequencing Project (ESP6500) databases were filtered out. Remaining variants present in both III:3 and IV:2 were analyzed.

WES on 3 patients and a normal relative from the Bulgarian families (Guergueltcheva *et al.*, 2011), was performed at Centro di Ricerca Interdipartimentale per le Biotecnologie Innovative (CRIBI), Padova, Italy. DNA libraries for WES were constructed following the standard protocol of the Ion AmpliSeq™ Exome RDY Kit (ThermoFisher Scientific). Starting from 100 ng of gDNA, a multiplex-PCR with 12 primer pools was performed in order to allow the amplification of 24,000 amplicons per pool, covering the exonic regions of the genomes (about 58 Mb). 9 µl of 100 pM barcoded libraries were amplified by emulsion PCR using a OneTouch2 instrument. Finally, the barcoded samples were loaded into Ion Proton P1 v3 chip and sequenced on the Ion Proton instrument using the Ion Proton HiQ Sequencing kit. The bioinformatic analysis was performed on the Ion Torrent Server and the Torrent SuiteTM was used to base-call and align the reads to the human reference genome (GRCh37/hg19). Alignment BAM files, Coverage Analysis statistics and Variant Analysis VCF files were produced. By default, the variant calling was performed using the "Germ Line-High Stringency" algorithm.

Generation of GST Expression Vectors and Constructs for in vitro *Translation.*† Human *OBSCN* cDNA (NM_052843) coding for Ig58/59 was amplified from total RNA extracted from human skeletal muscle tissue using specific primers (forward primer: 5'- aagaacacggtggtgcggg – 3'; reverse primer: 5'- gaggcccagcagggtgagc-3'). The *OBSCN* cDNA containing the c.13330C>T variant was generated by PCR using primers designed to introduce the cytosine to thymine nucleotide change into the wild-type cDNA (forward primer: 5'- aacgcggcggtcTgggccggcgcacag – 3'; reverse primer: 5'- ctgtgcgccggcccAgaccgccgcgtt-3') and sequenced using an ABI Prism 310 apparatus (Applied Biosystems). The amplified sequences were cloned into the vector pGEX (GE Healthcare) using the EcoRI-SalI sites to generate GST-OBSCN^{WT} and GST-OBSCN^{MUT} fusion proteins. Human *TTN* cDNA (NM_001267550) was amplified from total RNA extracted from human skeletal muscle tissue using specific primers. The *TTN* cDNA containing the Z9/Z10 domains of TTN was generated by PCR using the following primers (forward primer: 5' - gacaaagagaaacaacagaaa – 3'; reverse primer: 5' – atcttccctctgttgaatctc – 3') and sequenced using an ABI Prism 310 apparatus (Applied Biosystems). The amplified sequences were cloned into the vector pGBK-T7 in frame with a myc tag epitope (Clontech) using the EcoRI-SalI sites.

†Work of Dr. Vincenzo and collaborators

Protein Expression and in vitro *Interaction Studies.*[†] GST fusion proteins grown in *Escherichia coli* (*E. coli*) (BL21(DE3)) were induced at OD_{600}=0.6 with 1 mM isopropyl β–D-thiogalactopyranoside (IPTG) for 3 hrs at 30°C. Cells were harvested centrifugation at 4000 xg for 10 min at 4°C. The pellet was resuspended in cold buffer containing Phosphate Buffer Saline (PBS), 1% Triton X-100, 20 mM EDTA and lysed by sonication on ice. The soluble fraction was obtained by centrifugation at 13200 xg for 15 min at 4°C. The fusion proteins were immobilized by incubating 1 ml of the soluble fraction with 100 µl of glutathione-Sepharose 4B resin (GE Healthcare, Buckinghamshire, United Kingdom) for 10 min and washed three times with 1 ml of a buffer containing PBS and 1% Triton X-100 (Rossi *et al.,* 2014a). Beads were finally resuspended with an equal volume of PBS and the protein was eluted from the column with glutathione-PBS buffer.

In vitro translation and transcription experiments were performed using the TNT Quick Coupled Reticulocyte Lysate System as described by the manufacturer (Promega). 5 µl of the translation reaction were incubated with 12 µg of GST fusion protein in a buffer containing 10 mM Tris-HCl pH 7.9, 150 mM NaCl, 0.5% NONIDET P-40, 1 mM DL-Dithiothreitol (DTT), 1 mM phenylmethylsulfonyl fluoride (PMSF) and protein inhibitor mixture for 1.5 hrs at 4° C. After incubation, the GST fusion protein complexes were washed 3 times with interaction buffer. Bound proteins were eluted by boiling in sodium dodecyl sulfate polyacrylamide gel electrophoresis (SDS-PAGE) sample buffer and analysed by SDS-PAGE.

Western Blot Analysis. Protein samples were separated by 10% SDS-PAGE. Filters were incubated with primary antibody (mouse anti-c-myc, Clontech-Zymed Laboratories Inc.), and diluted in blocking buffer overnight at 4°C with agitation. Filters were washed three times with washing buffer (0.5% non-fat dry milk, 50 mM Tris-HCl pH 7.4, 150 mM NaCl, 0.2% Tween-20) for 10 min each, incubated with horseradish peroxidase-conjugated secondary antibody and detected using the ECL system (ECL Western Blot Detection Reagents, Promega).

Nuclear Magnetic Resonance (NMR) Preparation and Data Collection. All chemicals were ACS grade or higher and were typically purchased from Fisher Scientific unless otherwise specified. Recombinant ^{15}N, ^{15}N-^{13}C, and unlabeled protein were purified after overexpression in BL21 cells using a pET24a vector system (Novagen, San Diego CA) in a manner similar to (Rossi *et al*., 2014b). All nuclear magnetic resonance (NMR) experiments were collected on a 600 MHz Bruker Avance II spectrometer equipped with a TXI room temperature 5 mm probe with z-axis pulse field gradient coils. All NMR samples were collected at 25 °C in 20 mM Tris pH 7.5, 20 mM NaCl, 0.35 mM NaN_3, and 0.5-2.5 mM protein with 10% D_2O. All 2D and 3D NMR experiments were collected as previously described (Rossi *et al.,* 2014b). Further description of NMR collection is located in the supplemental information. Chemical shifts for Ig59 have been deposited in the Biological Magnetic Resonance Bank (BMRB) under accession number 26593.

A 2D HSQC was collected, as well as standard triple resonance experiments including HNCACB, CBCA(CO)NH, HNCO, HN(CA)CO, C(CO)NH, H(CCCO)NH, 15N-edited TOCSY, 15N-edited NOESY, 13C-edited NOESY, and pseudo-3D IPAP experiment for H-N residual dipolar couplings, as previously described (Rudloff *et al.,* 2015). Both NOESY experiments used 110 ms mixing time. Most experiments were collected with 128, 64 and 1024 points in the T1, T2, and T3 dimensions, respectively. NMR data were processed with NMRPipe (Muntoni, 2007), extended in the indirect dimension via linear prediction, and the resulting spectra were analyzed via Sparky (Lee *et al.,* 2015).

Standard Bruker IPAP experiments using 256 points for each T1 dimension were used to collect RDC data in isotropic and axially-compressed 5.5% acrylamide gel samples, as

[†]Work of Dr. Vincenzo and collaborators

previously described (Ng *et al.,* 2012). The program PALES was used for RDC alignment tensor fitting with a calculated Aa and Ar component of 0.00163 and 0.000901, respectively (Sewry, 2010). For all experiments, the 1H chemical shifts were referenced to external DSS, the 13C shifts were referenced indirectly to DSS using the frequency ratio 13C/1H = 0.251449527 and 15N shifts were referenced indirectly to liquid ammonia using 15N/1H = 0.101329118.

NMR Structure Calculation. Interproton distance constraints were derived from 3D NOESY experiments (^{15}N-edited and ^{13}C-edited 3D NOESY) as described previously. Dihedral constraints $\psi \pm 20^{\circ}$ and $\phi \pm 15^{\circ}$ for α-helix and $\psi \pm 40^{\circ}$ and $\phi \pm 40^{\circ}$ for β-sheet were included based on TALOS+ and the chemical shift index of ^{1}Hα and ^{13}Cα atoms (Rudloff *et al.,* 2015). Residual dipolar coupling data was included based on splitting values from an IPAP experiment, as previously described (Shen *et al.,* 2009). More information about the structure calculations can be found in the supplemental information. The final 20 structures were selected (from 200) based on lowest Q-values and lowest root mean squared deviation (RMSD) from the average, and were of high quality based on the statistical criteria listed in supplemental Table 3. The coordinates of the human OBSCN Ig59 structure have been deposited in the Protein Data Bank (2N56).

An ensemble of structures without dihedral restraints had a backbone RMSD of 0.85 Å when compared to structures with dihedral constraints (Udd, 2012). We attempted to further verify the structure by performing a H-D exchange experiment, however this Ig domain remains unfolded after lyophilization. Therefore, hydrogen bond constraints were not tested directly but instead were added into the structure only after the secondary structure was completely determined. Structures calculated without hydrogen bonds had an RMSD of 0.59 Å when compared to those calculated with hydrogen bonds, indicating that inclusion of these bonds did not drastically influence the overall structure. Hydrogen bond constraints of rHN-O = 1.5 Å to 2.8 Å and rN-O = 2.4 Å to 3.5 Å were included in the final stage of structure calculations, and were based off regions that were clearly in well-defined secondary structural motifs. Pseudopotentials for secondary 13C α and 13C β chemical shifts and a conformational database potential were included in the final simulated annealing structural calculations using the computer program XPLOR-NIH (Mastaglia and Laing, 1999; Udd and Griggs, 2001). Structures run with and without these pseudopotentials show an RMSD of 0.58 Å. The internuclear dipolar coupling (in Hz) were determined from the difference in J splitting between isotropic and radially compressed polyacrylamide, and were incorporated into the final structure calculation as previously described using an energy constant of 0.50 (Evilä *et al.,* 2014; Gautel, 2011). A comparison of structures run with and without RDC measurements show an RMSD of 0.67 Å. Q-factors were calculated by randomly removing ≈ 10% of the N-HN RDC data, and then comparing these values to those back-calculated from the structure.

Purification of Obscurin Ig59. Protein samples of pet-24a(+) human obscurin Ig59 were expressed in *E. coli* and purified through the following procedure. Starter cultures (~5mL) of Ig59 were made following addition of glycerol stock (500ul Ig59 PEP24A BL-21 cells into 50/50 glycerol) and 10ul of kanamycin. Starter cultures were shaken overnight at 37C, 250rpm, then added to 1L flasks of Luria broth (LB) (10g tryptone, 5g yeast extract, 5g NaCl, dilute to volume with diH_2O) along with 1mL kanamycin. These flasks were also shaken at 37C, 250rpm. Induction occurred ~3hr later, at 0.6-0.8 OD, with the addition of 0.2g IPTG. Approximately 3hr later, flasks were taken out of the incubator/shakers and centrifuged using a JLA 16.250 rotor at 6000rpm, 4°C for 15min. The supernatant and pellet were separated and the pellet was kept at -80°C until ready for further purification. Pellets were resuspended in G75 buffer (20 mM Trist, 50 mM NaCl, azide) and 100ul PMSF was added to prevent degradation during sonication at 100% amplification, 15s pulse, for 30min, then centrifuged

†Work of Dr. Vincenzo and collaborators

using a JA 25.50 rotor at 14000rpm, 4°C for 30min. The supernatant was run over a Nickel column and the eluent was concentrated in a 5K concentrator tube via centrifugation at 4500rpm for 90min intervals until less than 1mL solution remained, then run over a size exclusion column. Contents of column fractions were visualized using gel electrophoresis; fractions containing Ig59 were pooled and concentrated. The concentration of Ig59 in the resulting solution was obtained using a Thermo Scientific Nanodrop 2000 Spectrophotometer using the extinction coefficient (12490 $cm^{-1}M^{-1}$) and molecular weight (11.1 kDa) of Ig59.

Crystallization and X-ray Diffraction. The hanging drop method with 17% tacsimate, 0.1M HEPES pH 7.5, 4% PEG3350, and 10 mg/mL protein was used to obtain Ig59 crystals. Crystals were harvested and frozen in liquid nitrogen after one week using a glucose cryoprotectant and crystallographic reflections were collected at the Structural Biology Center beamline 19-ID-D at the Advanced Photon Source, Argonne National Laboratory. HKL2000 data processing calculated the unit cell to be P 3_1 2 1 (Otwinosky and Minor, 1997).

Table 2. Final refinement statistics of human obscurin domain Ig59. Parentheses indicate the statistics of the outer shell.

Wavelength (Å)	0.97918
Resolution range (Å)	30.49 - 1.177 (1.219 - 1.177)
Space group	P 31 2 1
Unit cell (Å)	60.98 60.98 47.56 90 90 120
Unit cell (°)	90 90 120
Total reflections	662701 (35265)
Unique reflections	33764 (3303)
Multiplicity	19.5 (10.7)
Completeness (%)	98.82 (92.53)
Mean I/sigma(I)	22.98 (5.07)
Wilson B-factor	14.83
R-merge	0.1345 (0.5394)
R-meas	0.1389
CC1/2	0.988 (0.912)
CC*	0.997 (0.977)
R-work	0.1642 (0.2634)
R-free	0.1851 (0.2974)
Number of non-hydrogen atoms	775
macromolecules	678
ligands	0
water	97
Protein residues	90
RMS(bonds)	0.033
RMS(angles)	1.46
Ramachandran favored (%)	99
Ramachandran outliers (%)	0
Clashscore	2.23
Average B-factor	20.5
macromolecules	19.4
ligands	0
solvent	28.3

Structure refinement. Crystal diffraction phasing was determined using the program Phaser-MR in the PHENIX ver 1.72.2-869 program suite via molecular replacement using PDB and reflection files from accession numbers 2YZ8 and 4RSV. The resulting structure was refined using the program PHENIX ver. 1.72.2-869-refine (Afonine *et al*., 2012). COOT was used to manually rebuild the structure in iterative rounds of rebuilding and refinement in PHENIX refine, resulting in a 1.18 Å resolution structure with an R_{free} value of 0.185 (Emsley *et al.*, 2010). More refinement

statistics are given in Table 2. The coordinates of Ig59 have been deposited in the PDB under accession number 5TZM.

Molecular Dynamics Modelling. Coordinates corresponding to the crystal structure of Ig59 were allowed to equilibrate using YASARA 12.7.16, at 310K, 150 mmol/L NaCl, pH 7.4, using the Amber ff03 forcefield in a simulation cell with periodic boundaries until the backbone RMSD no longer changed significantly (Wright *et al.*, 2005). Simulations were run with a timestep of 1.25 fs with the temperature adjusted using a Berendsen thermostat as described by Krieger *et al.* (Krieger *et al.*, 2014; Kireger *et al.*, 2004). Once finished, the p.Arg4444Trp mutation was introduced to the simulation using the 'swap' function in YASARA. This mutated structure was then once again allowed to equilibrate using the same parameters as for the wild-type structure, and the simulation was terminated when the RMSD stabilized. YASARA and Pymol were used to visualize the structures (de Groot *et al.*, 1997; The PyMOL Molecular Graphics System).

Circular Dichroism. All CD experiments were conducted in a 1 mm pathlength cuvette at 15 μM protein in 20 mM Tris buffer, pH 7.5 and 100 mM NaCl. Samples were measured in triplicate at 37°C on a Jasco J-810 spectrophotometer.

Results

Clinical Findings. † Our collaborators performed quantitative studies on human patients with dystrophies in order to investigate the disease. The proband (III:3) of these studies was a 61-year-old female presenting a progressive distal dystrophy since around age 30, affecting successively the right hand and progressing slowly to include both distal upper and lower limbs. At age 45, difficulties in standing up from a chair and a steppage gait appeared. At age 51, ambulation was not limited, but the patient exhibited foot drop (more pronounced on the right side), inabilities to stand on tip toes or heels, and a waddling gait. Hand finger extensors, foot evertors, toe extensors, and calf muscles showed severe weakness, but finger flexors and the tibialis anterior were normal. Glutei maximi, thigh adductors, and hamstrings were also severely affected, but proximal scapular, brachial, and antebrachial involvement was not detected. Hand palmar muscles (mainly thenar ones), calves and tibial muscles were atrophic (Fig. 1A1-5). In addition to the worsening myopathy, a progressive cervical myelitis of unknown aetiology appeared at age 52, manifesting as a sensory defect mainly in left lower limbs and spreading from foot to hip, causing severe pains and impaired balance. At age 61, she could walk slowly a few hundred meters with two aids. The previously described clinical selective pattern was found with severe wasting of hand finger extensors, toes extensors, peroneus lateralis, posterior calf muscles, and hamstrings. Hand finger flexors, tibialis anterior, quadriceps, along with scapular, brachial, antebrachial, axial, facial and oculo-bulbar muscles remained mostly spared. Quantitative measurements are detailed in Table 3. A sensory defect due to the myelopathy was found in both distal and proximal lower limbs (left > right). Creatine kinase (CK) levels were normal. Electromyogram (EMG) showed myopathic changes distally in the upper limbs and both proximally and distally in the lower limbs. Cardiac evaluation

†Work of Dr. Vincenzo and collaborators

(ECG and echocardiography) and spirometry were normal. Spinal cord MRI performed at age 53 revealed a posterior hyperdense signal from C2 to C7 (Fig. 1-C2-C7). Brain MRI and CSF were normal.

Our collaborators reported that the proband's son (IV:2) noticed first symptoms (fatigability in walking and difficulties in standing on tip toe) at age 14. He has been unable to run since the age of 16 years. He could walk a distance of around 1000 meters without aid at age 33. He had marked weakness and atrophy in the calf muscles and minor weakness in the interossei and finger extensors, but otherwise normal muscle strength in the proximal lower limbs and in the upper limbs (Table 3). No facial or bulbar weakness was present. CK levels, spirometry and cardiac evaluation were normal. Electromyography (EMG) showed myopathic changes.

Table 3. Quantitative clinical measurements performed by our collaborators documenting the progressive muscular dystrophy of the proband and her son.

Case Age Sex	Symptom onset (age in years)	Course	Current status: (age) functional ability	Current status Muscle weakness	Current status Muscle atrophy	CPK/ EMG / Cardiac echography/ EKG/ Vital capacity
Case I Proband **61y** **F**	Right hand atrophy / weakness (finger extensors) **(≈ 30y)**	Progressive worsening **Around 30y :** both hands wasting, inability to stand on heels and tiptoes, 35 y difficulties climbing stairs. 46 y Gowers, difficulties standing from a chair, running inability. Increased weakness of foot evertors, hand finger extensors **52y** : cervical myelitis manifesting by left foot extending to whole limb after 6 months. sensory defect without identified cause (Spine MRI T2 sequence hypersignal from C2 to C7) (normal Brain MRI, normal CSF fluid) Increased loss of balance and cordonnal pains **53 y** : fallings (weakness and balance impairment) **59 y** : walk with bilateral aid	**(61y)** Walking distance : few hundreds meters with aid Fallings, four to five times monthly right foot elevator Difficult walk with steppage and tendency to internal rotation of feet 10 m in 15 s with a cane. Inability to stand on heels and tiptoes Rising from chair 9 times in 60 s with two hands Thigh crossing : difficult Arm elevation : normal Painful spinal posterior column syndrome (myelitis)	**<u>Lower limbs</u>** Toes extensors 2, except big toe, 1 , Peroneus 1, , Tibialis anterior 4, Post legs 2+ Hamstrings 2, Quadriceps 5- Adductors 2+, Glutei maximi 2+, Glutei medii 4+, Iliopsoas 4+ **<u>Upper limbs</u>** Finger extensors 3-, index more affected : right index 2, left 2+ Finger flexors 4+ wrist extensors 4 scapular and brachial 5 **<u>Axial and neck</u>** flexors 4- **<u>facial, oculobulbar</u>** normal in addition : hypoesthesia of whole left lower limb due to myelitis	Legs (both compartments) Hand : palmar, mostly thenar region	CK normal EMG : myogenic Distal in Lower limbs, Distal + proximal in lower limbs Nerve : normal No decrement Normal echography and EKG VC : 85%
Case II Son of case I 33 y M	Difficulties standing on tiptoes and heels fatigability in walking (14y)	Mild progression At 16 y, interruption of sport at school and inability to run.	(33y) Walking distance : 1000 m without aid No fallings Climbing stairs with banister 10 m : 12s Rising from a chair : 24 times in 60 s without aid Arm elevation : normal	**<u>Lower limbs</u>** Peroneus 3-, Tibialis anterior 3+ Toes extensors between 4 , and 2 (big toe) Post legs 2 Pelvic and femoral muscles 5 **<u>Upper limbs</u>** Finger extensors 4+, Finger flexors 5 wrist extensors 5 scapular and brachial 5 **<u>Axial and neck</u>** flexors 5 **<u>facial, oculobulbar</u>** normal	Legs, mainly posterior compartment No atrophy of upper limbs	CK normal EMG : diffuse myogenic pattern Nerve : normal Normal echography and EKG VC : 86%

Muscle imaging performed by our collaborators on the mother at the age of 51 showed severe fatty degenerative changes in almost all lower leg muscles, except for tibialis anterior, posterior and long toe flexor muscles. The quadriceps was considerably less affected than the hamstrings and adductors. Glutei maximi and iliopsoas were less affected than glutei minimi and medii. The forearm extensor muscles showed reduced volume. At age of 61 years, this pattern remained mostly unchanged, except that the vastus medialis and vastus internalis fatty degeneration was more marked, particularly in right side. Rectus femoris and vastus lateralis remained spared (Fig. 1). In the 33-year-old son, the changes in CT scan were milder, with the exception of severe fatty replacement in the calf muscles and, less severely, in the lateral compartment peroneal muscles. All other muscles were intact.

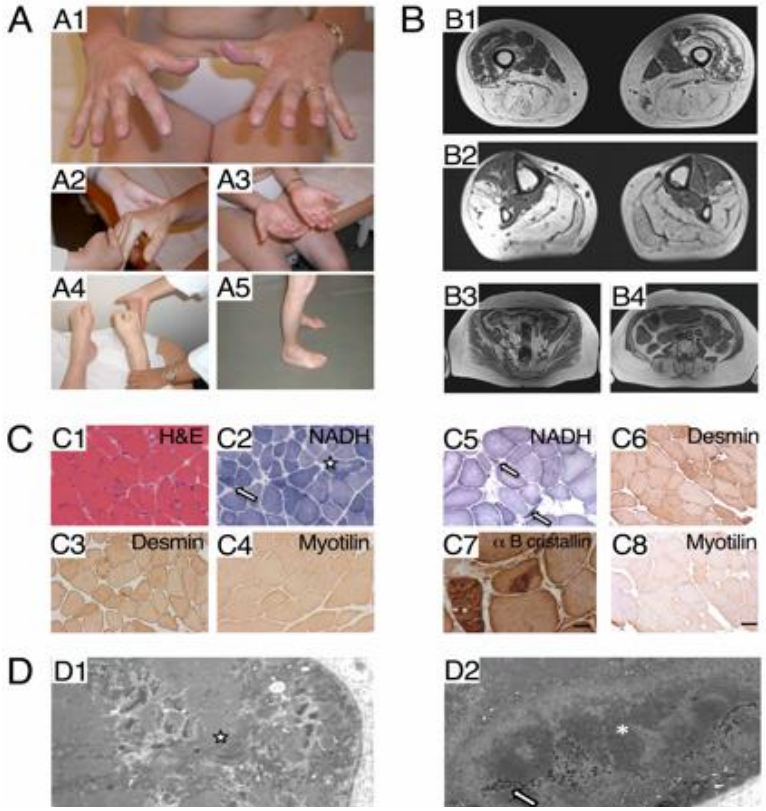

Figure 1. A/B) Clinical data, C) morphological studies, and D) ultrastructutal studies of the proband (III:3). A1-3: Evidence of muscle atrophy in thenar muscles. A4-5: All distal leg muscles of the proband are markedly affected, except for tibialis muscles. B1-4: Computed Tomography (CT) of the proband at the age of 51 showed severe fatty degeneration changes in most leg muscles. C1-C4: Radialis muscle biopsy of proband (III:3). C1. Haematoxylin & Eosin: presence of some nuclear internalization and fiber size variation. C2 NADH: lobulated fibers are indicated by an arrow; uneven staining of the intermyofibrillar network in some fibers is indicated by a star. C3 desmin: mild diffuse desmin surcharge in several fibers C4 myotilin.:ormal staining. C5-C8: Peroneal muscle biopsy from the proband son (IV:2). C5 NADH: atrophic lobulated fibers are indicated by an arrow. C6 desmin: mild diffuse desmin surcharge in several fibers. C7 alpha B cristallin: presence of dense protein aggregates. C4 myotilin: normal staining. D. Radialis muscle biopsy of proband (III:3), EM analysis. D1: presence of numerous abnormal mitochondria harbouring dotty or paracrystallin inclusions, in proximity of the star. D2: presence of a cytoplasmic protein aggregate composed by dark osmiophilic granulo-filamentous material corresponding to desmin, indicated by an arrow, and filamentous material indicated by an asterisk.

The radialis muscle biopsy from the proband (III:3) performed at 51 years showed some nuclear internalization, fiber size variation (Fig. 1B1), and type 1 predominance. Oxidative histoenzymatic reactions disclosed few lobulated fibers and uneven staining of the intermyofibrillar network (Fig. 1-B2). Our collaborators' peroneal muscle biopsy of the son (IV:2) at 33 years showed marked fiber size variability with the presence of some atrophic angulated fibers (Fig. 1C1). A few lobulated fibers were also present. Immunohistochemistry performed in both muscle biopsies revealed some desmin surcharge in both patients (Fig. 1B3, C2). In contrast only patient IV:2 (the son of the proband) harboured alphaB crystallin immunoreactive aggregates (Fig. 1C4). Myotilin immunostaining did not show

specific alterations (Fig. 1B4, C4). Ultrastructural studies performed by our collaborators on the proband (III:3) showed myofibrillar disorganizations resembling targetoid structures in a small percentage of the fibers (not shown). Abnormal mitochondria with some paracristalline inclusions (Fig. 1B5, indicated by a star) and dark dots were observed in numerous fibers. Focal disintegration of myofibrils, dark osmiophilic granulo-filamentous material corresponding to desmin (Fig. 1C5, indicated by an arrow) and filamentous protein aggregates (Fig. 1C5, indicated by an asterisk) were observed in PX (or son of the proband).

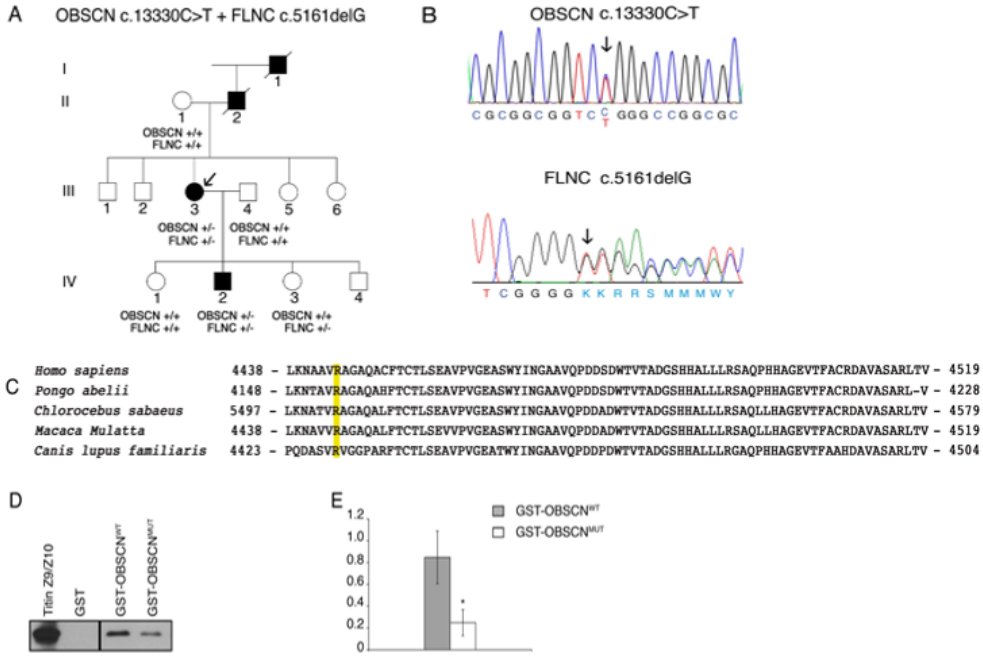

Figure 2. Genetic analysis of *OBSCN* c.13330 C>T and *FLNC* c.5161delG mutations. A) Family pedigree. Black filled symbols represent affected family members. The genotype of individuals is shown as follows: +/+ wild type, OBSCN +/- heterozygous for the c.13330 C>T mutation, FLNC +/- heterozygous for the c.5161delG mutation. Arrow indicates the proband. B) Electropherogram of the *OBSCN* gene sequence (upper panel) and of the FLNC gene sequence (lower panel). C) Phylogenetic alignment of the OBSCN orthologs. Sequences represent the Ig59 domains of OBSCN in distinct mammalian species. The arginine in position 4444 in the human *OBSCN* sequence is highlighted in yellow and is conserved in mammalian species. D) Interaction between titin domains Z9/Z10 and OBSCN domains Ig58/Ig59. *in vitro* transcribed and translated myc-tagged titin domains Z9/Z10 were used in pull-down experiments with GST-fusion proteins containing either wild type OBSCN Ig58/Ig59 domains ($OBSCN^{WT}$) or R4444W mutated OBSCN Ig58/Ig59 domains ($OBSCN^{MUT}$). Proteins were separated by SDS-PAGE, transferred to membranes and detected by mouse anti-myc antibodies. E) Quantification of GST pull-down efficiency. Protein bands intensities of myc-tagged Z9/Z10 titin domains precipitated by either $OBSCN^{WT}$ or $OBSCN^{MUT}$ GST-fusion proteins were evaluated by densitometric analysis and normalized on GST fusion proteins content. Data represent means values ± standard deviation of five independent experiments in triplicate. * $p < 0.01$ following t-test statistical analysis.

However, a subsequent WES analysis, performed by our collaborators using the DNA from the III:3 proband, identified an additional novel frameshift mutation in the *FLNC* gene (NM_001458.4). This was a deletion of a single base in exon 30 (c.5161delG) resulting in a frameshift and a premature stop codon (p.Gly1722Valfs Ter61, Fig. 2B). Sanger sequencing for *FLNC* exon 30 was performed by our collaborators on II:1, III:3, III:4, IV:1, IV:2 and IV:3. The *FLNC* variant c.5161delG was present in the two affected individuals (III:3, IV:2) but also in one healthy individual (IV:3). This deletion is located adjacent to the previously reported c.5160delC deletion, which is linked to distal

myopathy with upper limb predominance in three Bulgarian families (Guergueltcheva *et al.*, 2011). To investigate if the *OBSCN* variant identified in the French family was present also in the Bulgarian families with recurrence of the *FLNC* c.5160delC frameshift, our collaborators initially performed Sanger sequencing of exons 2, 50, 51 and 52 of the *OBSCN* gene in 12 individuals from the three related Bulgarian families [3 unaffected non-carriers of the *FLNC* c.5160delC (2701:IV.1, 2702:III.3; 2703:IV.3), 4 asymptomatic carriers of the *FLNC* c.5160delC (2701:IV16; 2701:V1; 2701:V2; 2702:IV3), and 5 individuals with distal dystrophy carrying the *FLNC* c.5160delC(2701:IV3; 2701:IV.10; 2702:III.1; 2702:IV.1; 2703:III.2)]. Since this initial screening did not identify any variant in the selected exons of *OBSCN*, WES analysis was performed by our collaborators in three affected *FLNC* mutation carriers and one normal relative from the Bulgarian families (patients IV:3 of family 1, III:1 of family 2, III:2 of family 3 and individual IV:1 of family 1) Variants were filtered for a global minor allele frequency ≤0.001, shared by the affected individuals but not present in the asymptomatic member. This analysis identified no mutation (missense, nonsense, indel) shared by the patients and not present in the normal relative of the Bulgarian families.

Structural Studies of the Ig59 Domain of OBSCN. From the above analysis, we reasoned that the dual *OBSCN* and *FLNC* mutations may represent a digenic heterozygous condition, where the *OBSCN* mutation leads to an increased penetrance of the *FLNC* mutation. In order to begin defining the molecular mechanism of the described phenotype, we investigated how the normal and mutated obscurin Ig59 domain interacts with its binding partner titin. We first solved the high-resolution structure of Ig59 (residues 4428-4521). Human obscurin Ig59 was isolated based on the original sequence alignment (CAC44768.1) (Young *et al.*, 2001). After purification, the beta-sheet rich structure was verified by CD, the pure Ig59 was crystallized. The resulting crystals diffracted to a resolution of 1.18 Å (Fig. 3A, Table 2). The resulting structure shows beta sheets extending from Glu 4435 to Lys 4438 (strand A'), Ala 4440 to Arg 4443 (strand A), Ala 4446 to Thr 4453 (strand B), Ser 4464 to Ile 4468 (strand C), Trp 4479 to Asp 4484 (stand D), His 4487 to Leu 4493 (strand E), Gly 4501 to Ala 4506 (stand F), and Ala 4512 to Leu 4519 (strand G). Overall, the structure forms a typical Ig-like fold (Meyer and Wright, 2013).

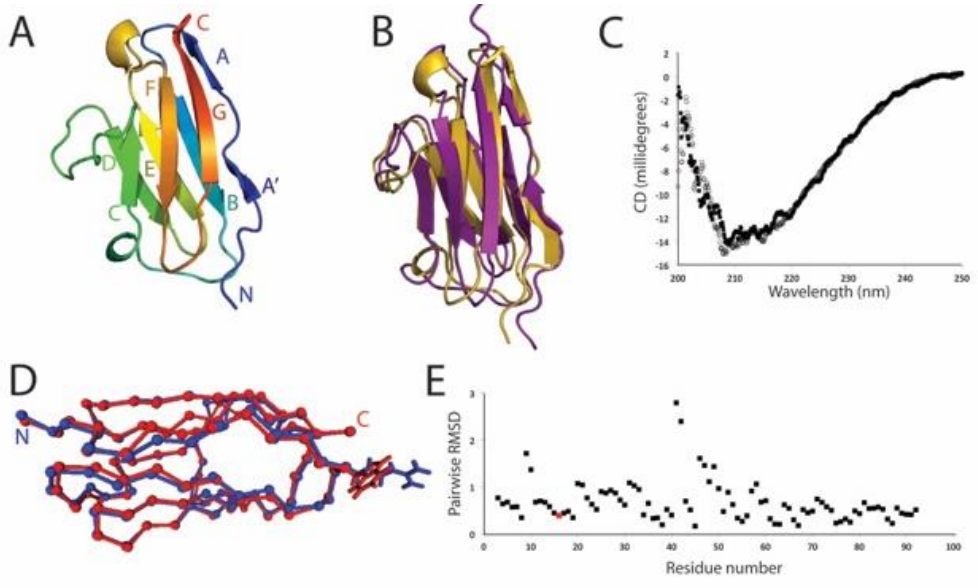

Figure 3: Structure and analysis of human obscurin Ig59. A) Cartoon of the Ig59 crystal structure, showing the typical Ig-like fold. B) Comparison between the Ig59 NMR and X-ray structure. C) CD plot of WT obscurin Ig58-59 (black squares) and p.Arg4444Trp (open circles). D) MD simulated average models of WT (blue) and Arg4444Trp (red) Cα positions. The side chains for Arg4444/Trp4444 are shown. E) RMSD vs residue number comparison of the mutant model to the wild-type model. The Arg444Trp site is shown in red.

An independently solved NMR solution structure of human obscurin Ig59 contains greater than 12 restraints per residue (Fig. 3B, Fig. 4, Table 4). The overall backbone root mean squared deviation (RMSD) of ordered heavy atoms is 0.609 Å. With the exception of Arg 4430, and Arg 4508, every backbone H-N bond and most sidechain C-H shifts are visible in these NMR experiments. H-N residual dipolar coupling experiment values independently verify the validity of this structure, and result in a Q-factor of 0.25 ±0.02. The NMR and X-ray structure have a pairwise RMSD of 1.609 Å (Fig. 3B). The differences between the two structures are most pronounced between residues Asn 4468 and Ser 4478. This area is in a long loop region, and is associated with higher B-factors in the X-ray structure and a lower number of NOE restraints in the NMR structures. Aside from this area, the structures are highly similar to each other.

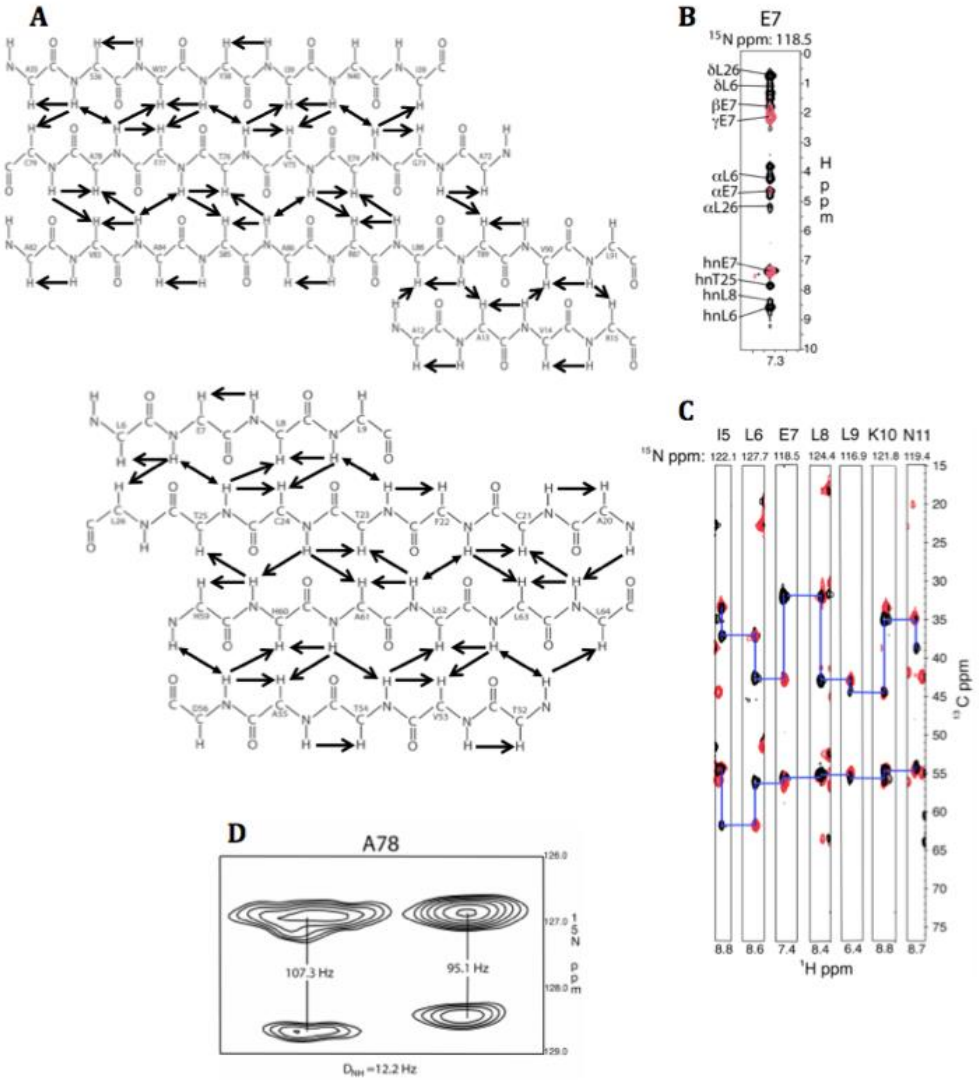

Figure 4. NMR data used to determine the structure of human obscurin Ig59. A) Observed beta sheet interactions of Ig59 as seen in the 15N-edited NOESY. B) NOESY data (in black) overlaid with TOCSY data (in red), showing self-peaks and cross-strand NOEs. C) Example of CBCA(CO)NH (in red) and HNCACB (in black) experiments, showing NMR assignments. D) Example of residual dipolar coupling data showing isotropic (right) and anisotropic (left) examples of the H-N bond from A78.

Table 4. NMR-derived statistics of 20 NMR structures[1] of human obscurin domain Ig59. Parenthesis indicate the number of restraints.

	<20>	**Best**
RMSD from distance constraints (Å)[2]		
total (1061)	0.028 ± 0.002	0.029
intraresidue (228)	0.005 ± 0.004	0.003
sequential ($\|i-j\|=1$) (382)	0.019 ± 0.005	0.022
medium range ($1<\|i-j\|\leq 1$) (95)	0.046 ± 0.006	0.056
long range ($\|i-j\|=1$) (292)	0.031 ± 0.003	0.003
hydrogen bonds (64)	0.056 ± 0.006	0.050
RMSD from exptl dihedral constraints (°)		
Φ,Ψ (144)	0.687 ± 0.116	0.684
RMSD from dipolar coupling restraints (Hz)		
D_{NH} (52)	0.89 ± 0.09	0.93
RMSD from exptl ^{13}C chemical shifts		
^{13}Ca (ppm)	1.59 ± 0.17	1.31
^{13}Cb (ppm)	1.46 ± 0.04	1.47
RMSD from idealized geometry		
bonds (Å)	0.004 ± 0.001	0.004
angles (°)	0.633 ± 0.020	0.640
impropers (°)	0.442 ± 0.036	0.431
Lennard-Jones potential energy (kcal/mol)[3]	-363 ± 10	-359
Q-value[4]	0.27 ± 0.04	0.25
% most favorable region in the Ramachandran plot[5]	74.1± 3.0	72.8
RMSD of the mean structure (Å)[6]		
all backbone atoms (3-91)	0.609 ± 0.063	0.494
all heavy atoms (3-91)	1.2128 ± 0.080	1.157

The p.Arg4444Trp mutation could affect the obscurin-titin interaction in two ways: it may unfold the entire Ig59 domain, or it may maintain the fold and simply perturb the binding event. To examine the effect of the p.Arg4444Trp mutation on the Ig59 structure, we conducted circular dichroism (CD) experiments on the WT and mutant forms of Ig59. As can be seen in Fig. 3C, the CD profiles are virtually identical, suggesting that the mutation does not globally disrupt the overall Ig-like architecture. To gain greater insight into the local effect of the p.Arg4444Trp, the WT and mutant protein structures were examined using molecular dynamics (MD). In each case, the RMSD relative to the starting model was measured until the simulation was fully equilibrated. The resulting models of wild-type and p.Arg4444Trp were then compared (Fig. 3D, E). While the long flexible loop between residues 4468 and 4478 was significantly different between these simulations, regions around the mutation were virtually unchanged in structure. Thus, these *in silico* results are consistent with our CD work showing that the mutation does not change the Ig59 structure significantly. Therefore, the p.Arg4444Trp variant likely directly alters the obscurin-titin interface.

[1] The 20 ensemble structures, <20>, are the results of simulated annealing calculations. The best structure is the closest to the average structure. The values shown for the <20> are the mean ± standard deviation.

[2] None of the 20 structures has a distance violation > 0.35 Å or a dihedral angle violation of > 5°. The force constants used in the SA calculations are as follows: 1000 kcal mol $^{-1}$ Å^{2} for bond length, 500 kcal mol^{-1} rad^{-2} for angles and improper torsions, 4 kcal mol^{-1} Å^{-4} for the quartic van der Waals (vdw) repulsion term (hard-sphere effective vdw set to 0.8 times their values in CHARMm parameters), 50 kcal mole^{-1} Å^{-2} for experimental distance constraints, 1 kcal mol^{-1} Å^{-2} for distance symmetry constraints, 0.5 kcal mol^{-1} ppm^{-2} for the ^{13}C chemical shift constraints, and 1.0 for the conformational database potential. The force constants (in kcal Hz^{-2}) used for dipolar coupling restraints is 0.50.

[3] Lennard-Jones van der Waals energies were calculated using CHARMm parameters and were not used in any stage of the structure determination

[4] Q-values were determined by randomly removing 10% of all RDC values. To ensure accuracy, an ensemble of structures with a second randomly removed subset of RDCs was also run. The Q-value of this second set was similar to the first.

[5] PROCHECK was utilized to generate the Ramachandran plot

[6] Backbone calculations include C$^{\alpha}$, N, and C′ atoms. Only residues 3–91 are included since no long-range NOE correlations were observed for residues 1–2 and 92–104.

The p.Arg4444Trp Variant Reduces the Interaction between Obscurin Ig58/59 and Titin Z9/Z10 Domains. To directly evaluate whether the p.Arg4444Trp variant alters the interaction of the Ig58/59 domains of obscurin with the Z9/Z10 domains of titin, we performed GST-pull down assays with either immobilized GST-obscurin^{WT} or GST-obscurin^{MUT} mixed with *in vitro*-translated titin Z9/Z10, cloned in frame with a myc-tag epitope. Densitometric quantification of the binding between the Z9/Z10 domains of titin and the Ig58/59 domains of obscurin showed that the bound fraction of GST-obscurin^{WT} protein was approximately two-fold higher than that of the GST-obscurin^{MUT}, indicating that the p.Arg4444Trp variant significantly weakens the titin-obscurin interaction (Fig. 2D, 2E). Other groups have suggested that this titin-obscurin interaction helps to strengthen the Z-line (Bang *et al.,* 2001). Our results show that the p.Arg4444Trp variant leads to a partial ablation of titin binding. This event leads to a weaker, less organized cytoskeleton, which in turn contributes to the distal muscular dystrophy phenotype of affected patients. This general mechanism of action is similar to the titin M10 mutations found in TMD and LGMD2J patients, which also serve to ablate a separate titin-obscurin interaction.

Discussion

Based on the evidence that the M10 domain of titin is mutated in patients with TMD and LGMD2J and that this domain interacts with the Ig1 domain of obscurin (Fukuzawa *et al.*, 2008; Pernigo *et al.*, 2010), we hypothesized with our collaborators that the *OBSCN* gene could represent a potential candidate for those cases of muscular dystrophies where a causative gene had not been identified. Screening performed by our collaborators of families with undetermined distal myopathy led to the identification of a novel variant in *OBSCN*, p.Arg4444Trp, which co-segregated with a c.5161delG in *FLNC*, in two individuals of a French family affected by distal muscular dystrophy. The *OBSCN* p.Arg4444Trp variant is conserved across mammalian species and is localized in a region of the protein that mediates the binding to the Z9/Z10 Ig domains of titin which facilitates the localization of obscurin to the Z disk region of the sarcomere (Young *et al.*, 2001).

Our structural studies showed that the previously mentioned variant does not lead to a global Ig59 domain misfolding but instead changes the surface topology of the domain. This mutation may thus affect obscurin binding to other members of the myofibril cytoskeleton. Pull-down experiments showed that this variant specifically weakens the binding between obscurin and titin, which may contribute to altered sarcomere stability and, eventually, disease. In support of this hypothesis, other mutations have been identified in patients with muscular dystrophies that affect the titin-obscurin interaction. For instance, mutations in the titin M10 domain, which mediates interaction with the Ig1 domain of obscurin at the M-band, were found to reduce the affinity of titin for obscurin and cause gradual failure of sarcomere maintenance in muscles of patients affected by TMD and LGMD2J (Fukuzawa *et al.,* 2008; Pernigo *et al.,* 2010). Similarly, the p.Arg4344Gln variant located in the Ig58 domain of obscurin identified in a patient affected by hypertrophic cardiomyopathy, was found to impair the binding of obscurin to the Z9/Z10 Ig domains of titin (Arimura *et al.,* 2007). Moreover, knock-in mice for the p.Arg4344Gln variant, when exposed to stress via trans-aortic constriction, develop a severe cardiac hypertrophy within 4-8 weeks (Hu *et al.*, 2016), further emphasizing the complementary roles of titin and obscurin in maintenance of sarcomere stability.

Interestingly, the two variants of Ig58 and Ig59 mentioned in this text, p.Arg4444Trp of Ig59 and p.Arg4344Gln of Ig58, involve a single point mutation from a charged to an uncharged residue (Arimura *et al.,* 2007; Fukuzawa *et al.,* 2008; Guergueltcheva *et al.,* 2011; Pernigo *et al.,* 2010). The isoelectric points of these regions are approximately 6.34 and 4.16, respectively. However, the point mutations cause a shift in isoelectric point to 4.48 and 3.90, respectively. Therefore, we hypothesize that the binding events between Ig58/59 of obscurin and Z9/10 of titin is electrostatically driven and that the difference pIs account for the reduction in binding affinity observed in the variants. In the future, we will test this hypothesis by creating a titin column and testing its affinity for the obscurin wild types and variants. If a lower concentration of salt is required to wash off the variant compared to the wild type, then we can effectively conclude that the variant affinity is lowered due to a decrease in electrostatic interactions.

FLNC mutations are known to cause adult-onset distal muscular dystrophy (Kley *et al*., 2012; Vorgerd *et al*., 2005; Shatunov *et al*., 2009; Luan *et al.,* 2010). The protein product of *FLNC*, filamin C, is an actin cross-linking protein involved in cytoskeleton organization and signalling (Razinia *et al.,* 2012). Mutations in *FLNC* were reported to destabilize muscle tissue homeostasis via the formation of protein aggregates (Löwe *et al.,* 2007). In addition, mutations in *FLNC* have been detected in patients with myofibrillar myopathy and also in patients with hand muscular dystrophy without myofibrillar aggregates (Duff *et al.,* 2011; Guergueltcheva *et al.,* 2011).

Our collaborators' clinical evaluations of the proband carrying both the *OBSCN* p.Arg4444Trp variant and the *FLNC* deletion indicate a late-onset dominant distal muscle dystrophy as well as the involvement of additional muscle groups than the Udd Myopathy (Duff *et al.,* 2011; Guergueltcheva *et al.,* 2011). The *FLNC* mutation did not completely segregate with the disease, as it was present in the two affected patients as well as one healthy individual in the French family analyzed. This incomplete segregation matches the behavior of a similar *FLNC* deletion reported in Bulgarian families (Guergueltcheva *et al.,* 2011), indicating an incomplete penetrance of the genotype. WES of representative individuals in the Bulgarian families did not reveal the presence of any other gene variants shared by all patients. Thus, the genetics behind the incomplete penetrance of the disease in the Bulgarian families remains unsolved and,

therefore, needs further analysis. In the French family reported by our collaborators, the combination of the *FLNC* c.5161delG frameshift and the *OBSCN* c.13330C>T variant co-segregated with the disease, with the *OBSCN* variant present only in the affected individuals. The healthy relative presenting only the *FLNC* c.5161delG deletion can be regarded as partial asymptomatic carrier.

In conclusion, the data on the French family reported by our collaborators depicts a novel digenic heterozygosity condition in the genetics of distal dystrophy, resulting in a dominant phenotype with quite severe clinical features; individual III:3 was unable to walk and constricted to a wheelchair, and IV:2 was unable to run since the age of 16. This phenotype is caused partially by an altered titin-obscurin interaction, and partially by altered filament C function of unknown molecular etiology.

Studies on the Molecular Motion, Structure, and Elasticity of Titin

Introduction

Titin's ability to both stretch and recoil is fundamental in preventing muscle overstretching and helps myocytes return to their original length. Recent studies have examined titin's mechanosensing abilities using tandem Ig and Fn-III-like domains (Granzier and Labiet, 2004; Linke *et al*., 2008; von Castelmur *et al.*, 2008; Lee *et al.*, 2010; Pernigo *et al*., 2010; Hsin *et al.*, 2011). While many of these domains are closely associated with other parts of the cytoskeleton, there are ~100 tandem domains in the sarcomeric I-band that are relatively free from extensive target protein interactions (reviewed in Kontrogianni-Konstantopoulos et al., 2009). Improta et al. (1998) and von Castelmur et al. (2008) have shown that this I-band region acts as a modified entropic spring whereby each domain behaves as a link in a chain connected by 3-5 residue interdomain linker 'hinges' (Improta *et al.*, 1998; von Castelmur *et al.*, 2008) (Fig. 1).

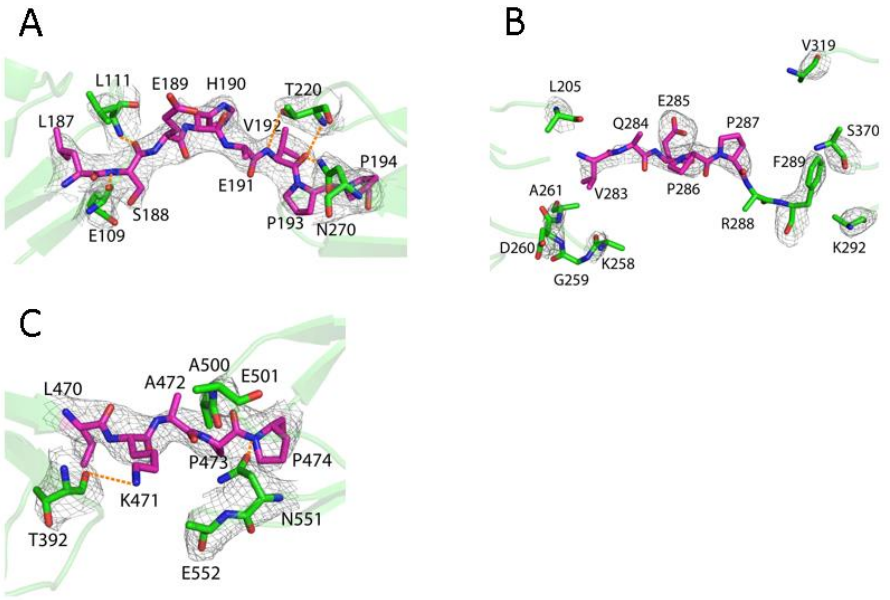

Figure 1. Short linker regions of I6 between A) Ig66-67, B) Ig67-68, and C) Ig69-70.

The further a polypeptide is stretched, the more energy additional stretching requires (Linke, 2000 (1);Linke, 2000 (2)). Through extensive molecular dynamics (MD) simulations, Lee et al. took this idea further and developed a comprehensive mathematical model where tandem Ig domains behave as a kind of entropic-enthalpic spring, termed the 'modified worm-like model' (mWLM) (Lee *et al.*, 2007; Hsin *et al.*, 2011). In this model, the Ig domains can move stochastically relative to one another, though there is also some breaking and forming of transient domain-domain and domain-linker non-covalent bonds. The mWLM agrees extremely well with the experimental data and explains titin's stretch resistance at very low forces (1-5 pN) (Linke, 2000 (1); Ma and Wang, 2003; Hsin *et al*., 2011). At slightly higher forces (~5 pN), the mainly disordered PEVK, N2A, and N2B regions of titin straighten out in an entropic-enthalpic spring mechanism (Frieburg *et al*., 2000; Bang *et al.*, 2001; Ma and Wang, 2001; Ma and Wang, 2003; Li *et al.*, 2002; Lee *et al.*, 2007). At extremely high forces (>50 pN), discrete titin Ig and Fn-III domains completely unfold, although the physiological relevance of such an event is uncertain (Rief *et al.*, 2000; Li *et al.*, 2003; Garcia *et al.*, 2009; Stacklies *et al.*, 2009; Lee *et al.*, 2010; Hsin *et al.*,

2011). Thus, titin displays a continuum of soft elasticity with the application of force (Hsin *et al.,* 2011).

This nuanced view of titin's flexibility at low forces runs somewhat counter to the crystal structure of 6 tandem titin domains, I65-70 (I6), which depict well-formed interactions between the linker regions and Ig domains (von Castelmur *et al.,* 2008). Such fixed interdomain interactions lead to the 'carpenter's ruler' model. This model reconciles several incongruences that arise from thinking of titin as a worm-like model: data collected by cryo-EM show large segments of the I-band region to be in straight lines with only occasional bend points, and SAXS data indicate a mostly elongated structure (Marino *et al.,* 2006; Vazina *et al.,* 2006; von Castelmur *et al.,* 2008; Marchetti *et al.,* 2011). Additionally, the persistence length of the titin I-band region is longer than a worm-like model would suggest (Di Cola *et al.,* 2005; von Castelmur *et al.,* 2008).

In an attempt to resolve the discrepancy between the worm-like and 'carpenter's ruler' models, we re-analyzed the published crystal structure data *(von Castelmur et al., 2008; Lee et al.,* 2007). Many of the linker/domain interactions that are present in the original model and contribute to an elongated overall structure are either absent or ambiguous in our structure (Fig. 1). Examination of symmetry mates suggest that the extended conformation of titin is not based on stabilizing domain-linker interactions but based instead on crystal packing interactions.

Molecular dynamics simulations performed by others and ourselves support the theory that this region of titin can be elongated, however the energy difference between a slightly bent and a straight molecule are below the threshold of thermal noise (Lee *et al.,* 2010). Together, these X-ray and MD analyses structurally validate the mWLM. Titin likely forms transient interdomain interactions, which explains the protein's resistance to stretch and its persistence length. These interactions, combined with limited flexibility due to steric hindrance between Ig domains, serve to keep titin in a mostly elongated orientation. While there is computational and circumstantial evidence for stabilizing interdomain interactions (Matsubara and Maruyama, 1977), their presence in this crystal structure is not definite.

Materials and Methods

Structure Refinement. PDB and reflection files from accession numbers 3B43 and 2RIK were implemented in experimentation. The structure of 3B43 was refined computationally and manually using PHENIX ver 1.72.2-869 and Coot was used for iterative rounds of structure rebuilding and refinement in PHENIX refine (Terwilliger *et al.,* 2008). Amino acids with continuous, clearly defined electron density at $\sigma \geq 1.5$ for at least two residues were included; all others were excluded. Ramachandran outliers were identified using the Molprobity server and Coot. Once identified, outliers were corrected. Refinement statistics are given in Table 1 (Chen *et al.,* 2010; Emsley *et al.,* 2010). The 2RIK structure was used for investigation of crystal packing interactions and the possible effects of packing on rigidity.

Table 1. I6 statistics after refinement. Methods for data collection of I6 are found in von Castelmur *et al.,* 2008.

Resolution range (Å)	16.99-3.30
Spacegroup	$P6_522$
Unit cell dimensions	a=b=141.43Å, c=166.01Å α=β=90°, γ=120°
Solvent content (%)	67.1
Matthews coefficient	3.74
Completeness (%)	98.6
Refinement:	
No. of reflections	14953
No. of protein atoms in asymmetric unit	3371
R factor/R free (%)	28.4/31.0
RMSD bond length (Å)	.0084
RMSD bond angle (°)	1.992
Avg B factor (B factor range) ($Å^3$)	88.5 (19.9-200.2)
Wilson B factor ($Å^3$)	82.6
Ramachandran favored (%)	90.6
Ramachandran outliers (%)	2.2

Molecular Dynamics Simulations. All MD simulations were performed with the PMEMD module of the Amber 12 MD software package, the AMBER 12SB force field, and a generalized Born implicit solvent (Hornak *et al.*, 2006; Case *et al.*, 2012; Nguyen *et al.*, 2013). The non-bonded interaction cutoff distances were set at 100 Å for MD and 150 Å for steered molecular dynamics (SMD). For equilibrium simulations, constant temperature (T = 300K) was enforced using a Langevin thermostat with a collision frequency of 1 ps^{-1}. The integration time step was 2 fs and all covalent bonds to hydrogen were held fixed with the SHAKE algorithm.

Steered Molecular Dynamics Simulations. SMD simulations fixed the α-carbon at the N-terminus of Ig65 (A1) and applied force to the α-carbon at the C-terminus of Ig70 (Q567), moving it closer to the N-terminus (Israleqitz *et al.*, 2001). In this way the protein was compressed at a constant velocity of 15 Å/ns. The SMD spring constant was set at 10 (kcal mol^{-1} $Å^{-2}$).

Results

The original structure of I65-I70 is hook-shaped; the first two domains are oriented 114 degrees relative to the final four domains, which are nearly linear (von Castelmur *et al.,* 2008). The high B factors of the published structure prompted our re-analysis of the electron density in 3B43 to determine if the sections with high B-factors had well-defined electron density. A 1.5 σ cutoff was used to fit the model in Coot. Continuous, unambiguous density for the backbone and side chains was required; all other residues and side chains were removed (Table 1 for fitting statistics and Fig. 2A). This newly refined structure has an RMSD of 0.6 Å compared to the original with several important differences. The overall B-factor is significantly lower than the original structure (88.4 $Å^3$ vs 118.5 $Å^3$; Fig. 2A inset). Furthermore, domain Ig68 is almost completely absent. In our model, interactions between the Ig domains and linker residues, which

were previously postulated to stabilize the structure in an elongated form, are either poorly defined or absent (Fig. 2B). These residues were removed due to poor electron density (see Materials and Methods for details). Analysis of the entire structure reveals a positive correlation between extensive crystal packing interactions and low B-factors (Fig. 2A and C; Fig. 3).

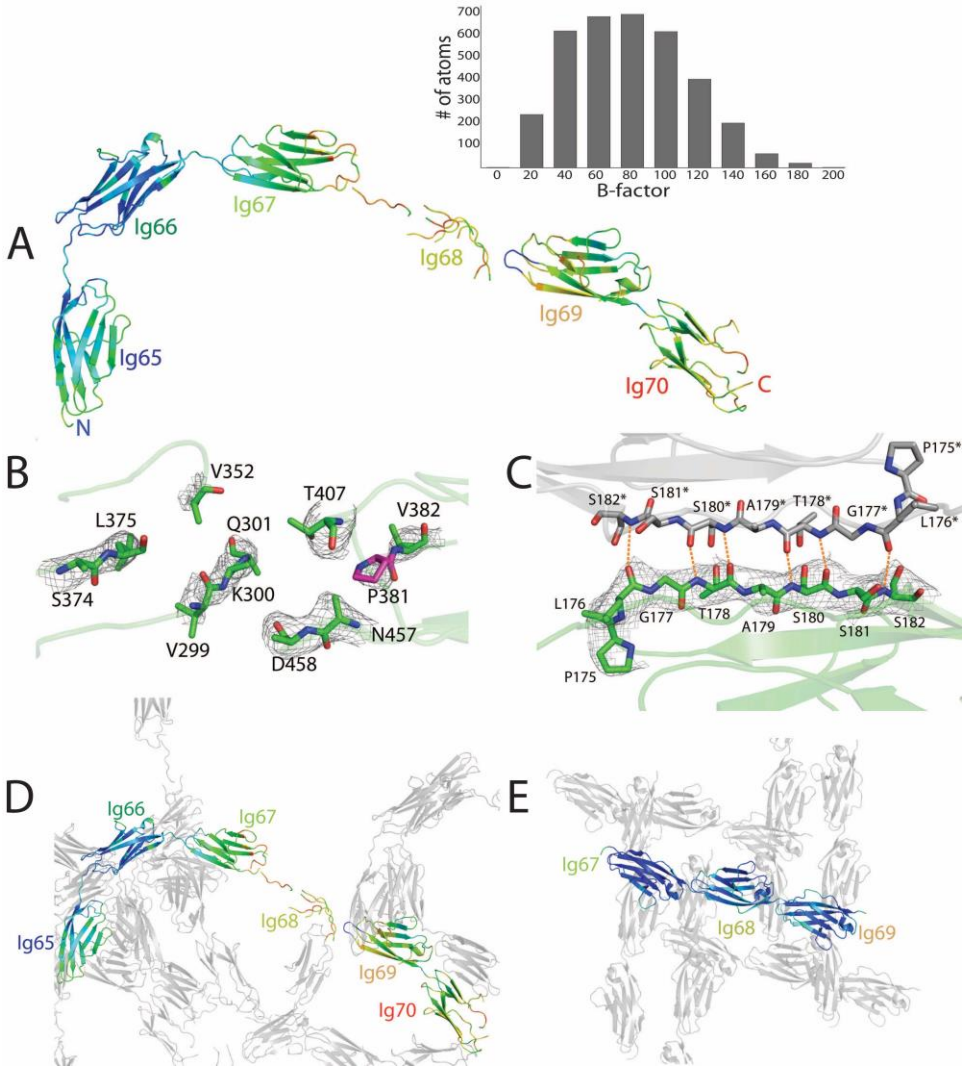

Figure 2. A) Cartoon representation of Ig65-70, colored by B-factor. Inset is the distribution of B-factors within the model. B) Linker region between Ig67 and Ig68, showing a lack of interactions and electron density to keep the molecule rigid. C) Example of the extensive packing of Ig66 against its symmetry mate, denoted with *. D) Global view of the crystal packing of Ig65-Ig70 relative to symmetry mates. E) Global view of the crystal packing of the 2RIK structure with central molecule colored via B-factors (range from 20-65 Å^3).

From this analysis, we reasoned that the overall shape of this region of titin could be explained by crystal packing interactions and not through inter-protein interactions (Fig. 2D). Since titin is predicted to be moderately flexible, this hypothesis could explain the dichotomy between MD simulations and the crystal structures. We therefore investigated the structure of Ig68-69-70 (2RIK), which was previously solved at 1.6 Å resolution to determine if crystal packing may have also contributed to its extended conformation (von Castelmur *et al.*, 2008). As can be seen in Fig. 2E, this construct has extensive packing interactions against its neighbors, and has correspondingly lower overall B-factors. Overlays of the same domain in 2RIK and 3B43 show that, while the tertiary structure of the Ig domains are virtually identical, the orientation of the Ig domains relative to each other vary (Fig. 4). We conclude that the overall shape of I6 observed in the 3B43 crystal structure is most likely dependent on crystal packing, not inter-protein domain-domain or domain-linker interactions.

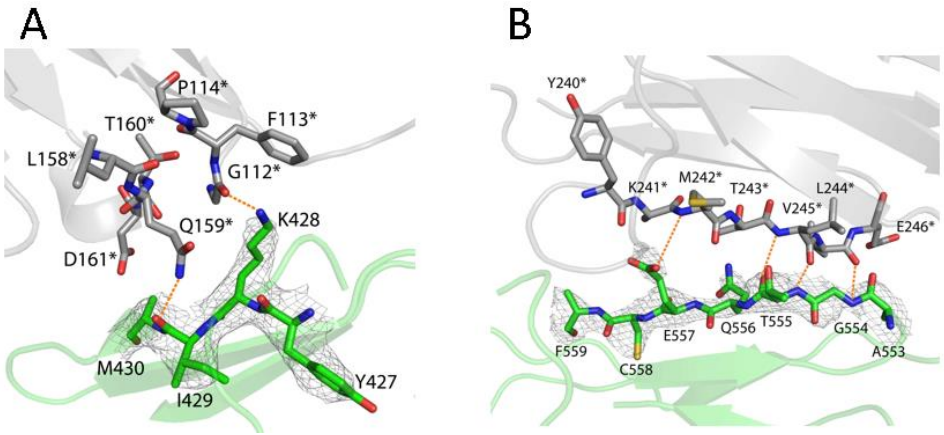

Figure 3. Crystal packing between A) Ig69 and B) Ig70 and their respective symmetry mates (denoted with *).

To examine the flexibility of titin Ig65-Ig70, we performed a series of MD and SMD simulations on the original titin structure. Model equilibration using implicit solvent conditions and the AMBER ff12SB force field showed that each domain displayed significant motions relative to its neighbor over 10 ns (Fig. 5). This is despite the Ig domains themselves being essentially static (average RMSD per domain over 10 ns is about 1.9 Å). This result agrees with similar experiments performed by Lee *et al.* (Lee *et al.*, 2010). To further probe the stiffness of this section, we brought together the two ends of this structure together at a rate of 15 Å/ns, from 232 Å to 141 Å. Analyses show that the straight part of the original structure (Ig67-Ig70) bent readily and that it required less than 0.6 kcal/mol of work (a rough cut-off for noise attributable to random thermal motion) to decrease the end-to-end distance to 200 Å (Fig. 6A-C). Smaller-diameter models required progressively more work. These data suggest that while the last 4 domains are mobile relative to their neighbors, mobility only extends to roughly 140 degrees as measured from the center of mass from each domain, in agreement with previous data (Lee *et al.*, 2010). At smaller angles, these Ig domains begin to run in to each other; thus, this molecule is intrinsically partially elongated. These data agree well with previously published MD bending data, as well as experimental SAXS data, showing that the average length of the I6 region is 220 Å (von Castelmur *et al.*, 2008; Lee *et al.*, 2010).

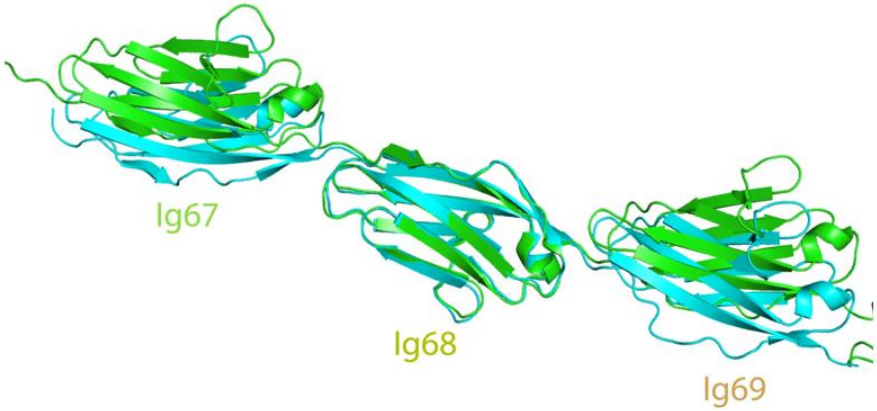

Figure 4. Alignment of Ig68 between the 2RIK (cyan) and 3B43 (green) structure, showing that the neighboring Ig domains are in different orientations between the two structures.

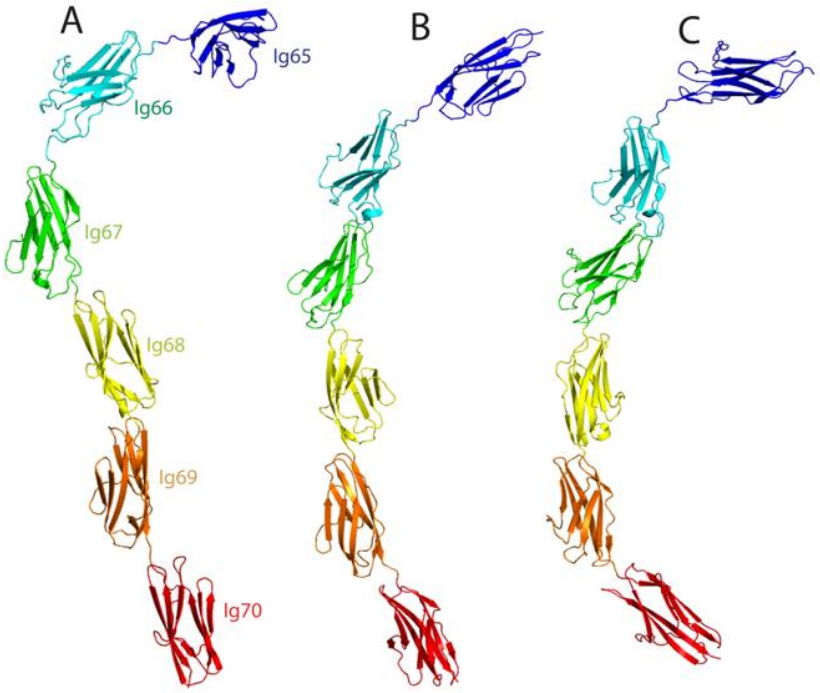

Figure 5. Snapshots of MD simulations for I6 at A) 2 ns, B) 5 ns, and C) 9 ns of equilibration, showing the straightening and bending of the final four domains. The models were aligned from residue 98 to 288.

Discussion

Here we re-analyze the Ig65-Ig70 crystal structure and suggest that the X-ray data do not support the 'carpenter's ruler' model of titin in solution. Instead, these data agree with subsequent MD simulations showing that titin domains move mostly independently of each other, with only transient inter-domain or domain-linker interactions (Lee *et al.*, 2010; Hsin *et al.*, 2011). This is particularly evident in Ig68, whose dynamic movement makes it virtually invisible in the structure. The presence of motion in this region is likely caused by a lack of symmetry mates to pack against, resulting in higher-than-average B-factors.

Our new model of Ig65-70 does not explain EM data that indicate that this region of titin is mostly elongated (von Castelmur *et al.*, 2008). Several possibilities could explain this discrepancy. First, it could be that transient interdomain and domain-linker interactions, while weak, short-lived, and not present in the crystal structure, are present in sufficient quantities as to exert a substantial stabilizing force on the molecule. These interactions could be overwhelmed by thermal motion and crystal packing interactions and might not be seen in crystal structures. Such interactions are built into the mWLM and seem to fit the wet lab stretching data (Lee *et al.*, 2010; Hsin *et al.*, 2011). Previous SMD experiments had problems in explicit solvent with hydrodynamic drag (Lee *et al.*, 2010). Thus, another possible explanation is that titin, once straight, tends to stay straight because of insurmountable solvent drag. Lastly, it may be that in the conditions under which EM experiments were conducted, titin is particularly amenable to forming straight lines.

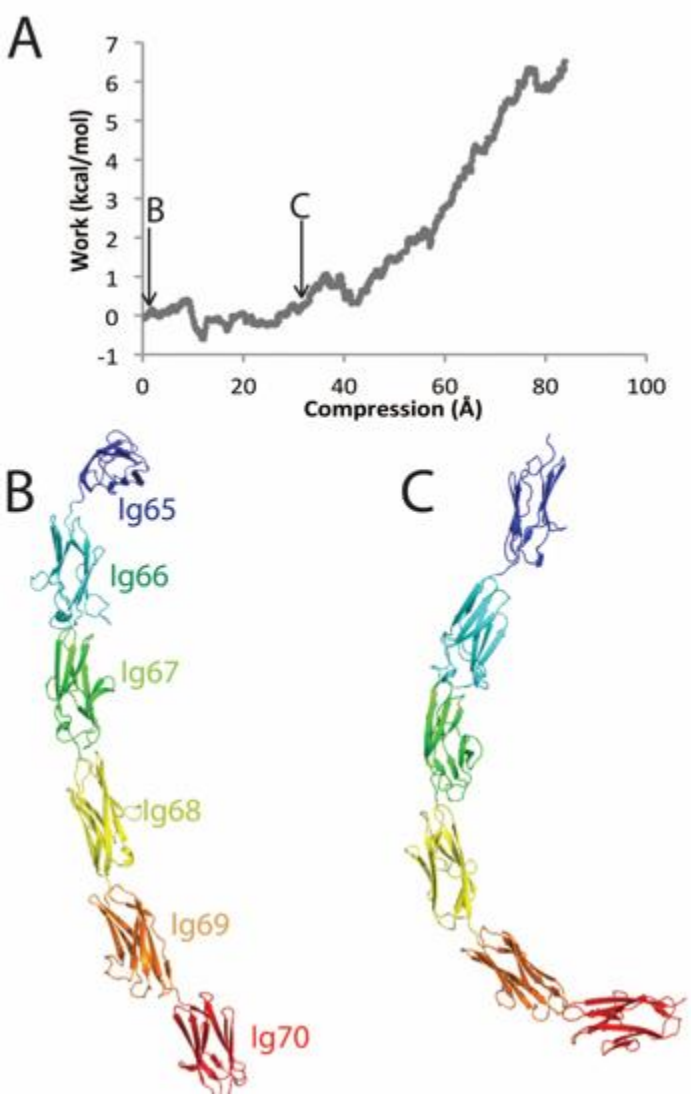

Figure 6. A) Force (in kcal/mol) v. distance (Å) graph of Ig65-70 (PDB 3B43). Images of Ig65-70 at B) 0 and C) 33 Å of compression.

MD simulations argue for a mWLM, yet previous a crystallography structure suggest a more rigid molecule. In this work, we identify crystal-packing artifacts as contributing to the apparent rigidity of the published crystal structure. Thus, the crystallography data in fact also suggest a dynamic system. This more nuanced view of the X-ray data reconciles this structure with the subsequent MD simulations.

Insight into the Auto-inhibitory Mechanism of the Second Kinase Domain of Obscurin

Introduction

Obscurin isoform B is expressed in low levels in a wide variety of non-muscle tissues, including epithelial, brain, liver, pancreas, and kidney tissues (Ackermann *et al.*, 2014; Russell *et al.*, 2002; Stroka *et al.*, 2016). This isoform of obscurin is unique in that it has two serine/threonine kinase domains located near its C-terminus (Russell *et al.*, 2002). Interestingly, these kinase domains are the only direct signaling moieties in obscurin. Obscurin also contains a RhoGEF/PH tandem domain that activates RhoA. All of these three obscurin regions— the two kinase domains and the RhoGEF/PH tandem domain— are involved in cell adhesion and signaling. The obscurin kinase domains phosphorylate cadherins while the activation of RhoA causes downstream effects that influence integrin signaling (Hu and Kontrogianni-Konstantopoulos, 2013; Stroka *et al.*, 2016). Ultimately, the cellular consequences of these signals are increased cell adhesion and stress fiber formation.

Obscurin is normally associated with cytoskeleton stability and dynamics. Thus, these three obscurin signaling domains provide a strong link between the cytoskeleton and cell adhesion. Ablation of this link has considerable (but little-studied) physiological repercussions— obscurin is the second-most mutated gene in breast and colorectal cancers (Wood *et al.*, 2007; Sjoblom *et al.*, 2006; Stroka *et al.*, 2016). Additionally, while non-tumorous tissue is rich in obscurin, biopsies of human breast cancer tumors have shown that obscurin is nearly absent in cancerous tissues (Stroka *et al.*, 2016). Due to these findings, it is paramount to understand the mechanism of action of these signaling domains and how mutations affect the activation, expression, and/or functionality of obscurin.

The overall goal of this project is to obtain high-resolution crystal structures of both human obscurin kinases, KI and KII. However, this goal has run into several significant hurdles. KI does not express well. KII can be expressed, purified and crystallized, but this process is extremely inefficient— protocols recovered an average of 1 mg from 16L of bacterial culture. Therefore, in lieu of a crystal structure, we opted to model the KII domain using computer simulations. Although the obscurin kinase domains have not been well-studied, the structure and mechanism of activation of a similar kinase, the titin kinase, has been extensively studied (Mayans *et al.*, 1998; Mayans *et al.*, 2013). Like all kinase domains, the titin and obscurin kinases have two active sites that neighbor each other: a substrate binding site and an ATP-binding site. These sites undergo cycles of activity and inhibition, depending on the needs of the cell, and as such, have highly specific regulatory and substrate recognition mechanisms (Mayans *et al.*, 1998).

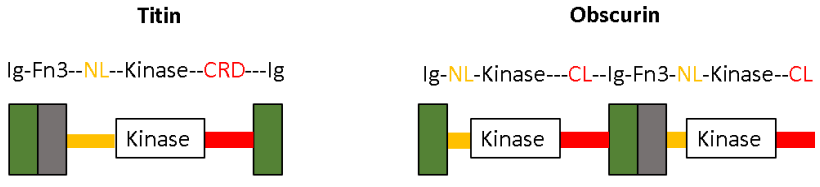

Figure 1. Schematic showing the similarity between titin (left) and obscurin (right) kinase regions. All three kinases are preceded by an Ig domain (green), the titin kinase and KI are also preceded by an Fn-III domain (grey), and all three domains have an N-terminal tail (NL, yellow) and C-terminal tail (CL) in obscurin or C-terminal regulatory domain (CRD) in titin (red) (adapted after Hu and Kontrogianno-Konstantopoulos, 2013).

The titin and obscurin kinases are serine/threonine kinases; they phosphorylate

serine and threonine residues. The two domains have similar surrounding are modular and are linked to the rest of the molecule through a (presumably) unstructured N-terminal and C-terminal linkers (NL and CL, respectively) (Hu and Kontrogianno-Konstantopoulos, 2013; Mayans *et al.*, 2013) (Fig. 1). These domains are catalytically active; they can both auto-inhibit and auto-activate themselves (Mayans *et al.*, 1998; Hu and Kontrogianno-Konstantopoulos, 2013) (Fig. 2). This function is a hallmark of most kinases (Tsai and Nussinov, 2013).

In the context of the entire protein architecture, the obscurin domains mirror titin (Fig. 1). Preceding the titin kinase are an Ig domain, an Fn-III (Fn-3) domain, and the N-terminal tail (NL). Following the titin kinase are the C-terminal regulatory tail (CRD) and another Ig domain. Similarly, in obscurin, the first kinase is preceded by an Ig domain and NL, followed by the CL. The second kinase domain region is also similar in its organization; as it is preceded by an Ig domain, Fn-III domain, and NL, and immediately followed by its CL (Fig. 1). The CL is at the extreme C-terminus of obscurin and, therefore, there is no possibility of an Ig domain following the CL.

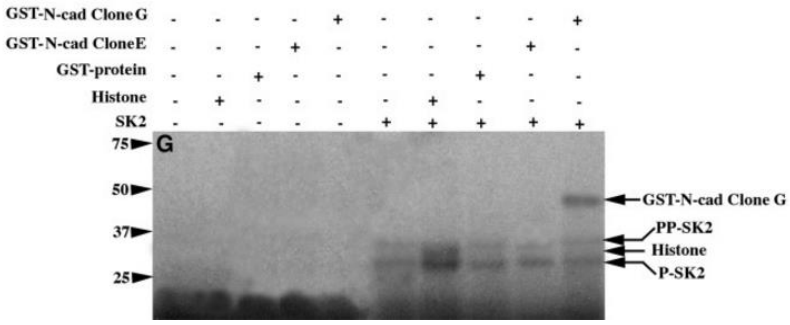

Figure 2. Gel depicting the auto-phosphorylating nature of obscurin KII as well as its ability to phosphorylate cadherins (taken from Hu and Kontrogianni-Konstantopoulos, 2013).

The titin kinase is usually inactive; structural studies have shown that the CRD wraps around the kinase domain and occludes the ATP-binding pocket. In addition, the N-terminal region of the titin kinase can also bind at or near the active site. Together, these domains prevent ATP-binding. (Hu *et al*, 1994; Kobe *et al.*, 1996; Mayans *et al.*, 1998; Gold *et al.*, 2006) (Fig. 3).

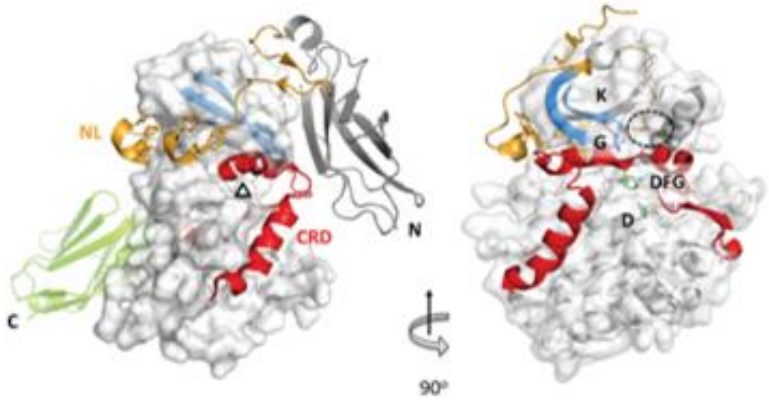

Figure 3. Lateral and frontal surface views of titin kinase showing the inhibited conformation. Note the position of the NL (yellow) and CRD (red) in relation to the active site, Δ (taken from Mayans *et al.,* 2013).

The titin kinase domain's unusual auto-inhibitory structure hints at its mechanism of action. Titin acts like a molecular spring; when stretched, the mechanical stretch physically removes the NL and CRD from the titin active site, freeing it for substrate- and ATP-binding (Grater *et al.*, 2005; Puchner *et al.*, 2008; Puchner and Gaub, 2010; Stahl *et al.*, 2011). The NL and CRD binding each effectively halves the catalytic activity and, therefore, the phosphorylation levels of the titin kinase. Together, the NL and CRD silence phosphorylation levels completely (Johnson *et al.*, 2001; Masterona *et al.*, 2011). This

mechanism is the only known mechanism of how the cytoskeleton directly acts as a mechanosensor- titin stretch results in target phosphorylation through the release of this auto-inhibitory mechanism.

Given that obscurin and titin have a similar overall architecture, perform similar connecting functions within the cytoskeleton, and contain similar kinase domains, we hypothesize that the kinase domains also are stretch-activated mechanosensors. As a first step to testing this hypothesis, we must determine whether the NL and CL regions of the obscurin kinase domains interact with the kinase domains. Towards this beginning goal, we took a two-pronged approach. To further investigate the auto-inhibitory mechanism of KII, the recombinant domain was purified and crystallized. From these crystals, the high-resolution crystal structure KII will be solved, though work is still in progress. Parallel to this wet-lab work, we also study computer simulations of KII. Herein, I describe the binding affinity studies performed on a simulated model of KII obtained by using titin's kinase as a model structure. The data indicate that, although the N-terminal tail of KII cannot bind to the active, site, the C-terminal domain appears to bind.

Materials and Methods

Purification of Obscurin KII. Protein samples derived from a pet-24a(+) construct containing a codon-optimized human obscurin KII domain were expressed in E. coli and purified as follows: Starter cultures (~5mL) of KII were made following addition of glycerol stock (500 µl KII pET24a BL-21 cells into 50/50 glycerol) and 10 µl of kanamycin. Starter cultures were shaken overnight at 37°C, 250 rpm, then added to 1 L flasks of LB (10 g tryptone, 5 g yeast extract, 5 g NaCl, in 1L dH_2O), along with 1 mL kanamycin. These flasks were shaken at 37°C, 250 rpm. Induction occurred ~3 hours later, at 0.6-0.8 OD_{600}, with the addition of 0.2 g isopropyl β-D-1-thiogalactopyranoside (IPTG). Approximately 3 hours later, flasks were taken out of the incubator/shakers and centrifuged using a JLA 16.250 rotor at 6000 rpm, 4°C for 15 min. The supernatant and pellet were separated and the pellet was kept at -80°C until ready for further purification. Pellets were resuspended in His-tag binding buffer ((50 mM NaH_2PO4, pH 8.0, 0.3 M NaCl, 100mM imidazole)) and 100 µl phenylmethane sulfonyl fluoride or phenylmethylsulfonyl fluoride (PMSF) was added to prevent degradation during sonication at 100% amplification, 15 s pulse, for 30 min, then centrifuged using a JA 25.50 rotor at 14000 rpm, 4°C, for 30 min. The resulting pellet underwent two cycles of 8 M urea resuspension and centrifugation under the same conditions as described previously. PMSF (100 µl) was added to the resulting supernatant, which was then dialyzed in a buffer containing 50 mM NaCl and 20 mM Tris pH 7.5 at 4°C for 2-3 hours. This solution was centrifuged again using a JA 25.50 rotor at 14000 rpm, 4°C for 30 min, then the supernatant was run over a Nickel column. The eluent was concentrated in a 5K concentrator tube via centrifugation at 4500 rpm, 4°C for 90 min intervals until less than 1 mL solution remained, then run over a size exclusion column. Contents of column fractions were visualized using gel electrophoresis; fractions containing KII were pooled and concentrated. The concentration of KII in the resulting solution was obtained using a Thermo Scientific Nanodrop 2000 Spectrophotometer using the extinction coefficient (42330 $cm^{-1}mol^{-1}$) and molecular weight (30.3 kDa) of KII.

Crystallization. The hanging drop method with various crystallizing solutions was used to obtain KII crystals. Crystals were harvested and frozen in liquid nitrogen until X-ray diffraction analysis using a glucose cryoprotectant.

Model Creation and Verification. The sequence of KII was modeled using PHYRE homology modeling. Verification of the model was performed in YASARA under explicit solvent conditions for ~15 ns (Krieger *et al.*, 2014; Krieger *et al.*, 2004). The N-terminal and C-terminal tails were not modeled using PHYRE as they were predicted to be relatively unstructured regions.

```
7621                                          eeesqg rsaqplpstk tfafqtqiqr
7681 grfsvvrqcw ekasgralaa kiipyhpkdk tavlreyeal kglrhphlaq lhaaylsprh
7741 lvlilelcsg pellpclaer asysesevkd ylwqmlsatq ylhnqhilhl dlrsenmiit
7801 eynllkvvdl gnaqslsqek vlpsdkfkdy letmapelle gqgavpqtdi waigvtafim
7861 lsaeypvsse gardlqrglr kglvrlsrcy aglsggavaf lrstlcaqpw grpcassclq
7921 cpwlteegpa csrpapvtfp tarlrvfvrn rekrrallyk rhnlaqvr
```

Figure 4. Sequence of KII showing active residues (magenta), NL (yellow), and CL (red). Sequence of KII obtained from PubMed obscurin isoform B, where numbers to the left indicate the residue number in the obscurin isoform.

Active Site Determination. Active residues in KII were determined via COACH analysis protein/ligand binding site prediction meta-server (Yang *et al.*, 2013) (Fig. 4).

N-terminal Binding Affinity Tests. The NL was modeled by hand as a random coil in YASARA and allowed to equilibrate for ~10 ns (Krieger *et al.*, 2014; Krieger *et al.*, 2004). The N-terminal tail and KII domain were the run through HADDOCK2.2 web docking prediction interface server (van Zundert *et al.*, 2016). Ligand 1 was KII, with active residues as predicted by COACH and ligand 2 was the N-terminal tail.

C-terminal Binding Affinity Tests. The CL of KII was modeled by taking the PHYRE model and fusing it to the C-terminal regulatory domain of titin. The titin sequence was then swapped out and replaced with the obscurin KII sequence. The CL and KII domain were the run through HADDOCK2.2 web docking prediction interface server (van Zundert *et al.*, 2016). Ligand 1 was KII, with active residues as predicted by COACH. Ligand 2 was the CL. Five runs were run in total with each run marking a different active segment of the CL. Runs were structured to run 10 CL residues as active with each sequential run overlapping by four residues. For the purposes of these tests, only the first 26 residues of the CL were tested; the CL wraps almost entirely around the main chain of KII and it would be nearly impossible for the residues directly behind the catalytic core to bind.

Results

The obscurin KII model was made using the PHYRE homology program with the titin kinase as a template (Fig. 5A). The original PHYRE-based model is seen in Fig. 5B. To verify the stability of this model, the model was equilibrated for 15 ns in explicit solvent at 310K using YASARA. At this point, no significant conformation changes were observed and the ATP-binding pocket remained intact (Fig. 6). The average structure and last structure, shown overlaid in Figure 5, have an RMSD of 1.436. Therefore, this equilibrated model was deemed of sufficient quality to move forward with binding affinity simulations.

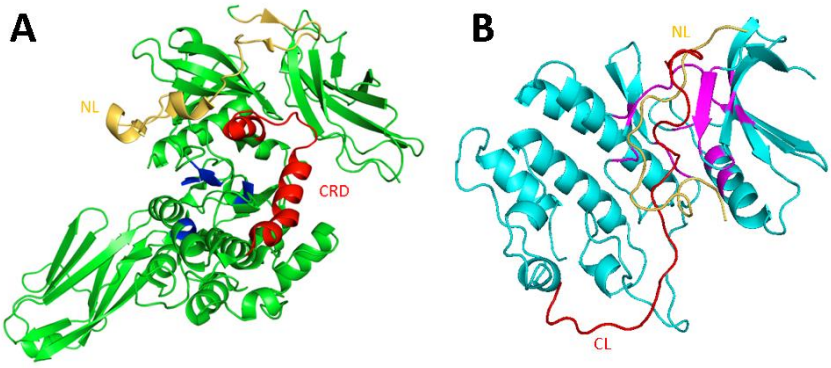

Figure 5. A) Cartoon representation of titin kinase showing the (yellow), CRD (red), and active residues (taken from PDB). B) Model of KII showing active residues (magenta), CL (red), and NL (yellow).

Following structure validation, the N-terminal tail was modeled by hand using the add residue function in YASARA. This procedure was chosen due to the small size of the NL; it is only 20 residues and is not predicted to have any regular secondary structure. Therefore, a random coil, allowed to equilibrate in solution, was a good starting point for initial binding studies. The NL and KII were then sent through a HADDOCK prediction binding web server to determine the likelihood of binding between the N-terminal tail and the active site of KII. HADDOCK is an information-driven flexible docking approach that predicts binding energies from predicted protein interfaces using ambiguous interaction restraints. Thus, this is an off-shoot of other *ab initio* binding algorithms. As an output, HADDOCK primarily uses a Z-score. This number represents the separation from the mean of all clusters tested. Thus, the lower the Z-score, the better a certain target docks into the protein binding site, as measured against a random insertion event (van Zundert *et al.*, 2016).

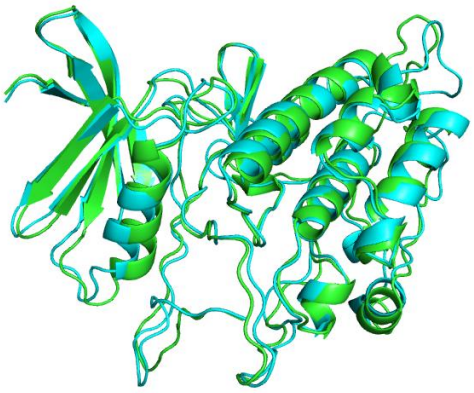

Figure 6. Average (green) and last (cyan) structures obtained from the YASARA verification of the KII model during ~15 ns of equilibration in explicit solvent.

While the RMSD for NL binding to KII is large, the overall Z-score is moderately good, suggesting that the NL can bind to the kinase domain. However, close examination of the structure reveal that these models require the removal of a critical beta strand in the kinase domain in order to bind. Given that this strand is a central part of the kinase domain, we suspect that this binding event would not occur in reality. HADDOCK runs with this beta strand intact demonstrate poor binding. (Fig. 7A-C). Similar results were obtained with an increased size in the KII binding pocket, indicating that even a large binding area did not improve NL binding. In

total, these data strongly suggest that, despite its close proximity, the N-terminus does not substantially interact with the KII active site (Fig. 7A-C).

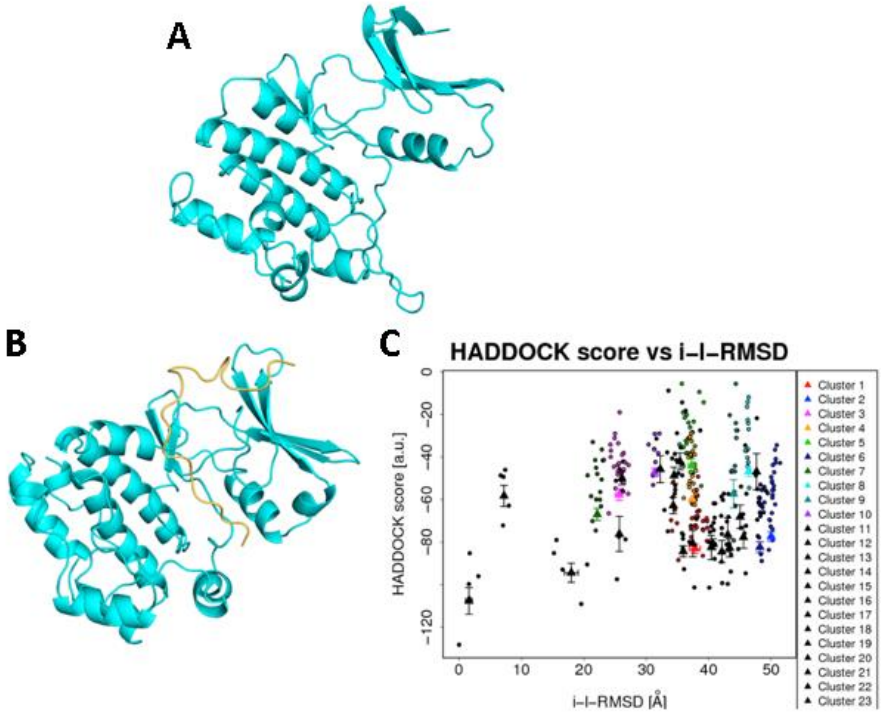

Figure 7. A) Model of KII (cyan) with all β-strands intact. The NL not shown to more clearly see all five β-strands. B) Model of KII (cyan) and NL (yellow) after the fifth β-strand was removed. C) HADDOCK results of Z-score vs RMSD showing large, variable RMSD between the two structures. The structure shown in B is Cluster 23, displayed by black triangles in the plot.

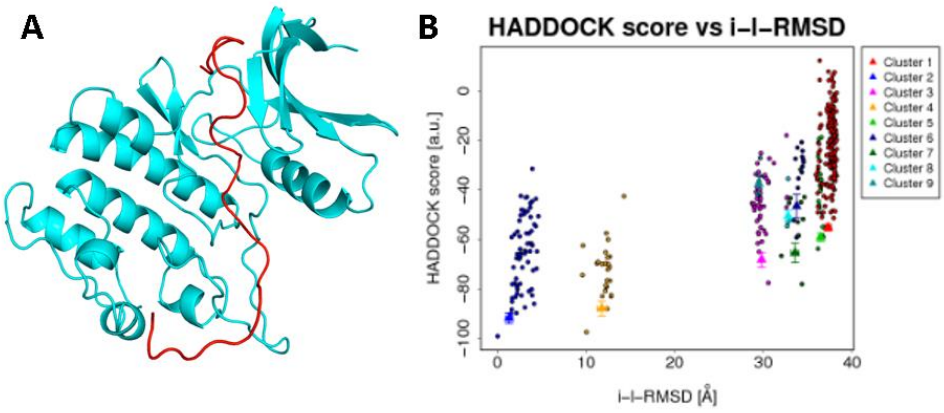

Figure 8. A) Model of KII (cyan) and C-terminal tail (red). B) HADDOCK results for the test of KII ATP-binding site with residues 4-14 of the CL showing Z-score vs RMSD showing small, stable RMSD between the two structures. The structure shown in A is Cluster 2, displayed by blue triangles in the plot.

Although the N-terminal tail could not bind to KII's active site, this would not necessarily be the case for the CL. This tail is longer than the N-terminus at 44 residues. This long region precluded modeling by hand. Since this tail may act similar to the titin domain, the CL sequence was threaded through the titin CRD Structure. As the CL begins on the opposite side of the molecule from the active site, only the end of this stretch was tested. Proximal residues would be to far away to bind to the active site.

We tested this binding in two ways. First, we threaded the obscurin C-terminal domain through the titin CRD region and docked this onto our obscurin KII model. We then let this region equilibrate in explicit solvent

using YASARA for 50 ns. Analysis from this simulation indicated multiple regions of the obscurin CL could bind to our KII model. Next, we took overlapping sequences of the KII CL and performed HADDOCK runs into the KII active site, in a similar way to how we tested the N-terminal region. In total, 5 separate KII/CL runs were completed, each considering 9 possible clusters. Consecutive runs differed in the 'active' region of the CL, beginning with the first ten residues and overlapping by 4 residues each time. In other words, residues 1-10, 4-14, 8-18, 12-22, and 16-26 were run separately. HADDOCK results consistently predicted binding between the CL and KII's active site with low RMSDs and reasonable Z-scores (generally >-1.7) (Fig. 8). The run in Figure 8 considered the ATP-binding site and residues 4-14 of the CL as active and shows cluster 2 from the 4-14 run. The interactions between the NL and active site tended to be electrostatic interactions.

Discussion

HADDOCK analysis determined that the NL was able to bind to the active site of KII but only if there was significant displacement of the fifth β-strand, which is unlikely due to the extensive hydrogen-bonding amongst β-sheets. Binding occurred via electrostatic interactions between the KII active site and NL when this fifth β-strand was removed. Consistent binding was observed between the CL and the active site, as shown by HADDOCK analysis. This binding occurred electrostatically between the ATP-binding site of KII and the CL and is presumably similar in nature to that of the CRD binding to the ATP-binding site of the titin kinase. However, the *in vivo* and *in vitro* validity of the obscurin KII/CL binding event has yet to be tested. If the binding is relatively strong, then it is likely that the CL has some inhibitory nature on the active site. If not, then KII must be auto-activated and auto-inhibited by some other mechanism. Given that not all proteins in the titin-like family are activated in the same manner as each other, nor as titin itself (Mayans *et al.*, 2013; Greene *et al.*, 2008), coupled with our findings regarding the NL and KII, this possibility may be even more likely as the possibility that obscurin and titin kinases hold similar mechanisms of activation.

In the future, we hope to quantify the strength of the KII/CL binding using YASARA to determine how much force is required to break the electrostatic bond between the two structures. To complement this computer research with wet-lab work, we will design and implement an affinity column to test the affinity of the CL for the kinase domain as well as the ability of the CL to displace substrate and/or ATP from the active site(s) of KII. Lastly, we will continue to crystallize KII in order to solve its crystal structure.

Appendix A: Methods for Additional Projects

Materials and Methods (KI)

Purification of Obscurin KI. Protein samples of pet-24a(+) human obscurin KI were expressed in *E. coli* and purified through the following procedure. Pet-24a(+) KI was transformed onto BL-21 cells and starter cultures (~5mL) of KI were made from these with the addition of 10ul of kanamycin. Starter cultures were shaken overnight at 37C, 250rpm, then added to 1L flasks of LB (10g tryptone, 5g yeast extract, 5g NaCl, dilute to volume with diH_2O), along with 1mL kanamycin. These flasks were also shaken at 37C, 250rpm. Induction occurred ~3hr later, at 0.6-0.8 OD, with the addition of 0.2g IPTG. Approximately 3hr later, flasks were taken out of the incubator/shakers and centrifuged using a JLA 16.250 rotor at 6000rpm, 4C for 15min. The supernatant and pellet were separated and the pellet was kept at -80C until ready for further purification. Pellets were resuspended in G75 buffer (20 mM Tris pH 7.5, 50 mM NaCl, diH_2O), 100ul PMSF was added to prevent degradation during sonication at 100% amplification, 15s pulse, for 30min, then centrifuged using a JA 25.50 rotor at 14000rpm, 4C for 30min. The resulting pellet was resuspended in 8M urea and centrifuged under the same conditions as described previously. PMSF (100ul) was added to the resulting supernatant, which underwent fast dialysis 20mL of G75 buffer at (4°C). This solution was centrifuged again using a JA 25.50 rotor at 14000rpm, 4C for 5min, then the supernatant was run over a Nickel column. All fractions of the Nickel column were visualized using gel electrophoresis.

Materials and Methods (Rho-GEF)

Purification of Obscurin Rho-GEF. Protein samples of pet-24a(+) human obscurin Rho-GEF were expressed in *E. coli* and purified through the following procedure. Pet-24a(+) Rho-GEF was transformed onto BL-21 cells and starter cultures (~5mL) of Rho-GEF were made from these with the addition of 10ul of kanamycin. Starter cultures were shaken overnight at 37C, 250rpm, then added to 1L flasks of LB (10g tryptone, 5g yeast extract, 5g NaCl, dilute to volume with diH_2O), along with 1mL kanamycin. These flasks were also shaken at 37C, 250rpm. Induction occurred ~3hr later, at 0.6-0.8 OD, with the addition of 0.2g IPTG. Approximately 3hr later, flasks were taken out of the incubator/shakers and centrifuged using a JLA 16.250 rotor at 6000rpm, 4C for 15min. The supernatant and pellet were separated and the pellet was kept at -80C until ready for further purification. Pellets were resuspended in His-tag binding buffer ((500mM NaH_2PO_4, pH 8.0, 3M NaCl, 100mM imidazole for 10x)) and 100ul PMSF was added to prevent degradation during sonication at 100% amplification, 15s pulse, for 30min. Then the solution was centrifuged using a JA 25.50 rotor at 14000rpm, 4C for 30min and the supernatant was run over a Nickel column followed by a DEAE column. The eluent from the DEAE column was visualized using gel electrophoresis and then concentrated in a 5K concentrator tube via centrifugation at 4500rpm for 90min intervals until less than 1mL solution remained.

Materials and Methods (Rho-GEF-PH)

Purification of Obscurin Rho-GEF-PH. Protein samples of pet-24a(+) human obscurin Rho-GEF-PHwere expressed in *E. coli* and purified through the following procedure. Pet-24a(+) Rho-GEF-PH was transformed onto BL-21 cells and starter cultures (~5mL) of Rho-GEF-PH were made from these with the addition of 10ul of kanamycin. Starter cultures were shaken overnight at 37C, 250rpm, then added to 1L flasks of LB (10g tryptone, 5g yeast extract, 5g NaCl, dilute to volume with diH_2O), along with 1mL kanamycin. These flasks were also shaken at 37C, 250rpm. Induction occurred ~3hr later, at 0.6-0.8 OD, with the addition of 0.2g IPTG. Approximately 3hr later, flasks were taken out of the incubator/shakers and centrifuged using a JLA 16.250 rotor at 6000rpm, 4C for 15min. The supernatant and pellet were separated and the pellet was kept at -80C until ready for further purification. Pellets were resuspended in His-tag binding buffer ((500mM NaH_2PO_4, pH 8.0, 3M NaCl, 100mM imidazole for 10x)) and 100ul PMSF was added to prevent degradation during sonication at 100% amplification, 15s pulse, for 30min. Then the solution was centrifuged using a JA 25.50 rotor at 14000rpm, 4C for 30min and the supernatant was run over a Nickel column followed by a DEAE column. The eluent from the DEAE column was visualized using gel electrophoresis and then concentrated in a 5K concentrator tube via centrifugation at 4500rpm for 90min intervals until less than 1mL solution remained.

Appendix B: Tutorial on How to Solve a Crystal Structure using HKL2000, Phenix, and Coot

HKL Steps:

Step 0: Open HKL2000
Open a terminal window, go all the way up in directories. Then go through 'usr' to 'local' to 'bin' and open HKL2000. To do this type:
cd ..
cd ..
cd usr
cd local
cd bin
hkl2000

Step 1: Load Data
Once HKL2000 has opened fully, look under the space titled 'directory tree' and click on 'berndsce,' 'Desktop,' 'APS4102014,' then on the data folder you will be working on (eg. 'JMU113' or 'JMU211').

Designate your input folder, which is the data folder you just chose. This is where HKL will scan for data files. Create or assign where the output files will go and click 'load data sets.' To create a new folder, click 'Create Directory' and type the name.

Click 'Load Data Sets.' You will choose the file with 'data' in the name, and NOT with 'scan' in the name. Once this has opened, record your wavelength and frame width. Then, click on the tab entitled 'Index.'

If there is more than one data set, you will have to do run HKL twice, once with each data set. DO NOT try to do one HKL using both data sets. You can merge them later in CCP4.

Step 2: Indexing
Click on 'fit basic' and make sure that there are exactly 6 red boxes. Set resolution maximum to 'corner' if you think there is data that was not included and to 'edge' if you only want to go to the user set boundaries of the original data. For Synchrotron data**, 'corner'** is more appropriate. The minimum resolution should be 50.00. Click on **'Peak Search,'** then, in the new window that appears, click on 'Peak Sear,' and minimize the random peaks. This will usually involve lessening your peaks until they fall within the range 300-800. Record the number of peaks. Once this is done, click 'OK' then **'Index.'**

Step 3: Choosing a Space Group
When the window appears for you to choose a space group, choose the group that has the highest symmetry with the lowest percent (usually it is green and closest to the top). Then click **'Apply and Close.'**

Step 4: Refining
Your χ^2 values should be less than 2. Click 'Refine' and continue to refine until your χ^2 values level out (are constant). At this time, the 'Integrate' button should be green (ideally). If it is, press it.

If not, click **'Fit All'** then 'Refine' again until the χ^2 values level out. You may also need to change you space group, the values of which will have change due to your refining. Click 'Bravais Lattice' to open up your space group options. Again, choose the one with the most symmetry. If you do change your space group, you will need to refine again. Record the space group at the top of this screen. 'Integrate' should be green now, so press it.

Step 5: Integrate
Your mosaicity value should be less than 1. Record both it and your resolution range. Ideally, the graph on the left should look like one downward slope while the graph on the right should be fairly constant. Record your positional, partiality, X- χ^2, Y- χ^2, and χ^2 values.

Step 6: Scale
Click on the 'Scale' tab at the top and make sure your space group matches with the one you previously chose. Make sure that the box next to 'Small Slippage, Imperfect Goniostat' is red. Click **'Fix B'** and make sure that 'Write Rejection File' is red also. Then click 'Scale Sets,' which should be green.

Pay close attention to the graphs titled Completeness vs. Resolution and I/Sigma and CC1/2 vs. Resolution. These will aid you in determining the minimum value of your resolution. On the Completeness vs. Resolution graph, move your cursor to where the blue line begins to drop and remember this number. Scroll down to the CC1/2 vs. Resolution graph and move your cursor along the grey limit to where the grey meets the blue. This number should match up fairly decently with the number from before. However, to be more accurate, click on the 'Show Log File' button at the bottom and scroll down on the window that opens to the bottom. Compare the values in the Average I column to those in the Average error column and record the Shell lower limit for the line in which the Average I is approximately 2 times that of the Average error. This will be the minimum value of your resolution. Hit 'Close' on this window when done, set your minimum resolution, and the maximum for 50.

Click 'Delete Rejection File' then 'Scale Sets.'

Record a, b, c and alpha, beta, gamma.

Your output file will have the name output.sca and will be wherever you specified it to go in the 'Data' tab. This is what you will use in CCP4.

CCP4 Steps:

Step 0: Opening CCP4
From the Finder, go to 'Applications,' then 'ccp4-6.4.0' and 'ccp4.' (If it is not already down on the tabs, which it should be)

Step 1: Running CCP4
On the right side of the screen there is a program list. Under 'Data Reduction and Analysis,' click 'Symmetry, Scale, and Merge (Aimless).'

In the window that pops up, make sure that 'Option to skip scaling & just merge' is black. Also, make sure the FreeR column has 0.05 in the blank and that 'Copy FreeR from another file' is grey. Change the Input reflection file type to 'Scalepack file' and choose your input/output destinations. SCA #1 is your input. You must input the 'output.sca' file, NOT the 'scalepack.sca' file.

HKLOUT is where you type/choose the output destination. When choosing your output destination, you will have to name the file. To do this, choose the folder destination, click 'OK' and then add to the blank a /_____.mtz where the ____ is the desired file name. Then click 'Run' and 'Run Now.'

If the process is finished quickly, chances are that you did something wrong. It should at least take a few seconds.

Phenix Steps:

Step 0: Opening Phenix
Go to the 'Finder' icon and click 'Applications,' 'Phenix 1.8.4.' This will open the Phenix Home window.

Step 1: Select Project
You will need to create a new project file that will store your data. On the Phenix Home screen, click 'New project,' then give the project an ID and a directory. There can only be one project per directory, so you may need to create a new folder in Finder that will become your directory. When done, click 'OK' and make sure there is a green check by your new project ID. If there isn't one, double click on the ID.

Step 2: Xtriage
On the right side of the Phenix Home screen, look under 'Reflection tools,' and click on 'Xtriage.' In the bar next to 'Reflections,' you will browse to find the .mtz file you created in CCP4. Then click 'Run.'

In the new tab, there will be a subtab called 'Twinning analysis.' Click this and scroll down to 'Likely point groups.' Choose your point group and record it in your lab notebook. Then, save the file with a file name as ____reindexed.mtz where ___ is the desired name of the file. MAKE SURE TO ADD THE .mtz TO THE END.

Step 3: Molecular Replacement
Back at the Phenix Home window, under 'Molecular replacement,' click on 'Phaser-MR (simple interface).' Add your reindexed file by clicking 'Add file.' It should be in a folder labeled Xtriage. This will be your X-ray data file.

Put 95 in the 'Sequence identities' bar then look under
'Search options.' Here, change 'Also try alternative space group(s)' to 'All possible in same point group.'

You will also need to add a .pdb file, which will be your input model. Click 'Run' and 'Run locally.' When Phenix has finished, click 'Run phenix.refine.'

Step 4: Refining
In 'Refinement settings,' make sure the following are checked: 'XYZ coordinates,' 'Real-space,' 'Rigid body,' 'Individual B-factors,' 'Automatically correct N/Q/H errors.' All else should be left unchecked.

If this is your first time refining, under 'Input data' go to Options…' and make sure that 'Generate new R-free flags' is checked. Also, change 'Fraction of reflections in test set' is .05.

If this is your second time refining, you should check 'TLS parameters,' 'Simulated annealing (Cartesian),' and 'Simulated annealing (Torsion angles)' under the 'Refinement settings' tab. You will also need to go back to 'Options…' and uncheck 'Generate new R-free flags.' Also, you will replace the .mtz file from Xtriage and instead use the file ending in ____data.mtz as your new X-ray data file.

Once you have refined significantly, you may want to do the following...

Uncheck 'Rigid body,' which will rotate your structure within the electron density. Do this if you find that, when refining, the computer flips or turns you structure in a way you don't want it to.

Check 'Optimize X-ray/stereochemistry weight' and 'Optimize X-ray/ADP weight,' which will have the program put more emphasis on the data you already have.

Uncheck both 'Simmulated annealing…' once your loops are in good shape, as this part checks your loops.

Check 'Update waters' to put in waters to your structure. ONLY do this when your structure is as good as you can get it (or near so). In other words, only towards the end of refinement.

Once you think you are done, record the refinement number and the Rfree value for that refinement.

COOT Steps:

The figure below shows the electron density map for the protein. You need to make the sequence fit into the blue or green parts of the map. To do this follow the steps provide below.

Step 0: Opening a Structure in Coot
Click on 'Open Coords…' and select the .pdb file you received in the above steps. It will probably either be in an Xtriage folder or a Refine folder. You can also do this by clicking on

‘File’ then ‘Open Coordinates’ and selecting your .pdb file. This will open the chain of amino acids.

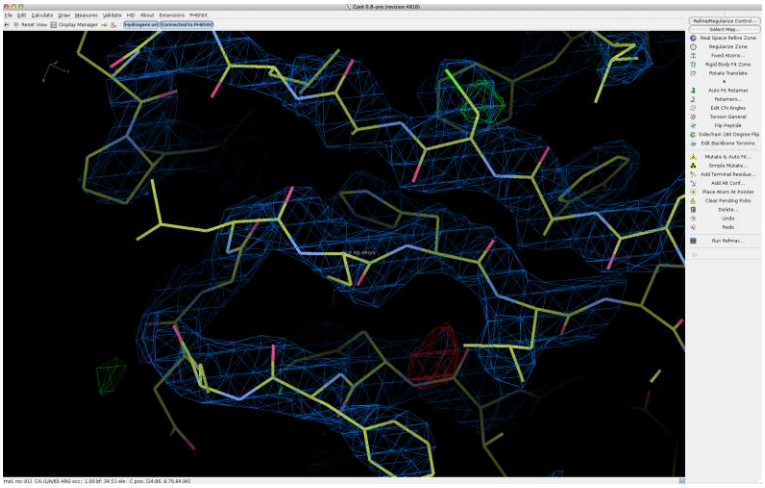

You will then need to open up the electron density map. To do this, click on ‘File,’ then ‘Auto Open .mtz’ and select the .mtz file that does NOT contain data in the name.

Go to ‘Draw,’ then ‘Cell and Symmetry,’ ‘Yes,’ ‘Show,’ and ‘Apply’ to show the unit cells.

Step 1: Basic Coot

Right clicking and scrolling will allow you to zoom in and out of your structure.

Left scrolling will allow you to change how much electron density it shown. The numerical value will be displayed at the top of the structure picture. You should operate within the 1.5-2 range of these values.

Left clicking on an amino acid will label it. To remove labels, go to ‘Measures,’ ‘Distances and Angles’ and click ‘Clear All Atom Labels.’

Left clicking and dragging will allow you to rotate the x-, y-, and z-axes around the center of your screen, which is represented by a pink square in the center of Coot.
Holding down the control button on your keyboard while left clicking and dragging will allow you to move the center of your screen.

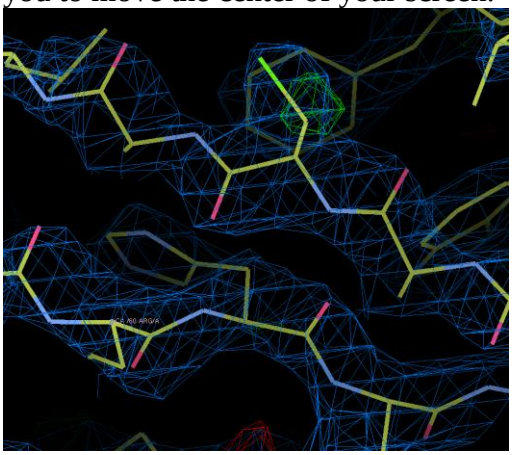

When you are manually fitting the sequence into the density map, you want to get the sequence into the blue or green density as shown above. When there is red density, this means that the sequence is not favorable to be in that area. You want to AVOID the red density*. The blue density is the occupied area that is acceptable.

*When there is red density within your blue density, to use Dr. Berndsen's words, "cry." There is not much you can do here except use the 'Real Space Refine Zone' feature to move it out of the way as best as possible. This feature will auto fit your amino acid to the electron density map.

Step 2: Navigating the Structure

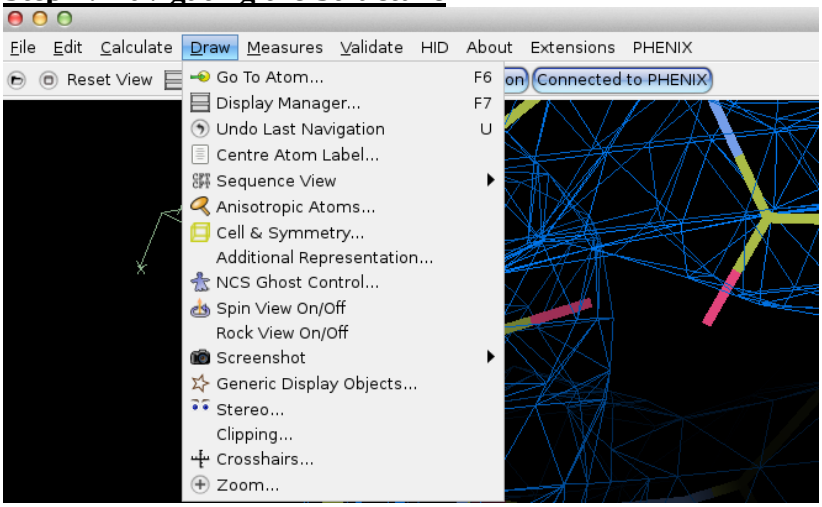

To move from amino acid to amino acid, select the 'Go To Atom' under the 'Draw' pulldown menu. This will allow you to move throughout the sequence one amino acid to the next. If there is more than one chain, it may be necessary to designate which one you want to navigate through.

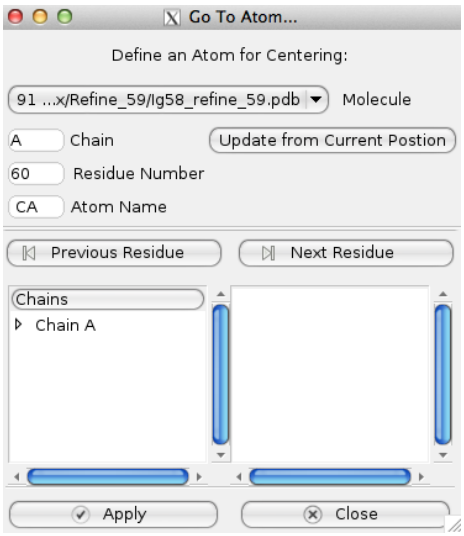

The 'Go To Atom' screen looks like the figure above. You can move forward in the chain by clicking "Next Residue". To move backward click on "Previous Residue."

An easier way to do this is to go to ‘Draw’ then ‘Sequence View’ and your .pdb file. This will display the entire chain in a window. Moving this window to the side will allow a quick jump from amino acid to amino acid. Clicking on the desired amino acid number will place you at that spot.

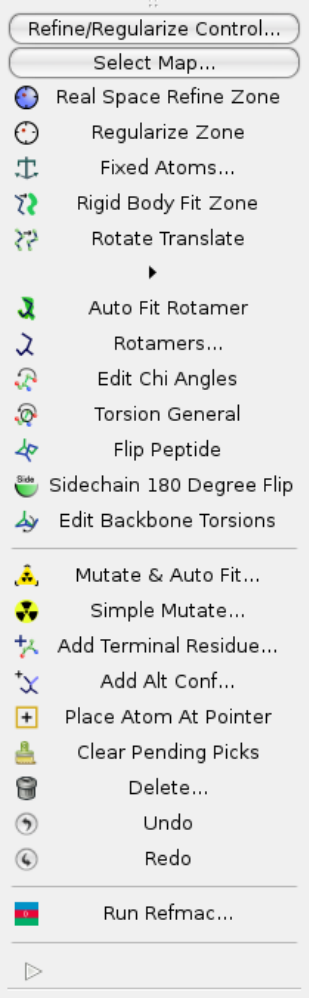

Step 3: Real Space Refine Zone

The ‘Real Space Refine Zone’ may be the most helpful tool that Coot has to fit your structure. This will fit your amino acid to the electron density and allow you to position it the way you want.

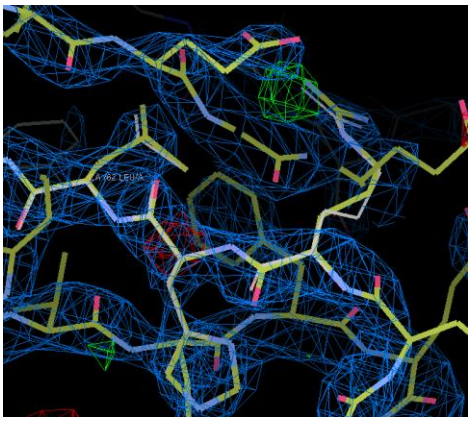

The ‘Real Space Refine Zone’ will auto fit an area that you select. This will get the angles and bonds in optimal orientations for the sequence. To select one amino acid to refine, double click on some part of the amino acid. To select a larger region, single click on each side of the region. . Dragging an amino acid or region will allow you to finagle the region where you want it. It is easiest to grab the region by clicking and dragging from a “corner” or “bend” of the region. You will then have to accept or reject the refinement. Ideally, all of the categories below will be green.

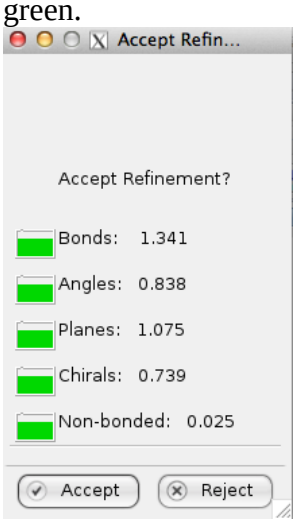

Once the bonds and angles are in the optimal orientation press the accept button to keep the changes you made on the structure. Use discretion to determine whether or not an orientation is suitable. It is more important to match an amino acid to the given electron density than it is to have the orientation be optimal (have everything be green).

There will be many green and blue regions surrounding the atom where waters, calcium, etc. will eventually go. Do not panic if you see these seemingly random regions go unfilled.

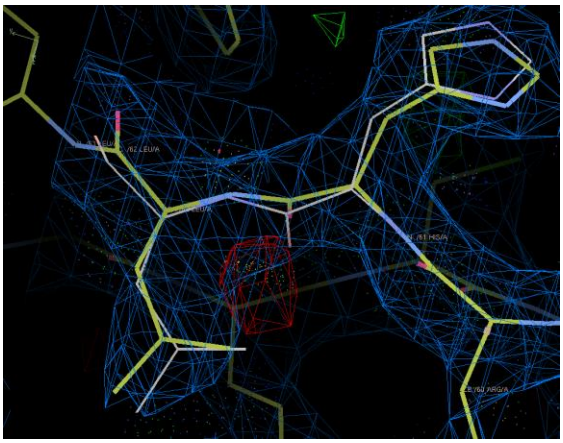

‘Regularize Zone’ is similar to ‘Real Space Refine Zone’ but may make more drastic changes. If you are having a lot of difficulty with a region, this may be good place to go as more of a last resort and may point you in the right direction.

Step 4: Mutate and Auto Fit

If you want to change an amino acid, use the ‘Mutate & Auto Fit’ button from the side menu that is shown above then select the amino acid you want to change it to. This can also be done with the ‘Simple Mutate…’ feature, but this will not fit the amino acid to your electron density.

Step 5: Add Terminal Residue

If there is an amino acid missing from the sequence you can add in an amino acid by using the ‘Add Terminal Residue’ button. After clicking it, click on the terminal carbon of your structure and then on ‘Accept’ in the window that pops up. Make sure that the added amino acid (it will be faded grey) is inside the electron density on your screen (you can move it by clicking on the grey amino acid and dragging it) before hitting ‘Accept.’

If the amino acid appears and is not connected to the rest of your chain, simply click ‘Real Space Refine Zone’ and select an area containing the terminal residue and the newly added amino acid. The amino acid should then connect.

Step 6: Ramachandran Plots

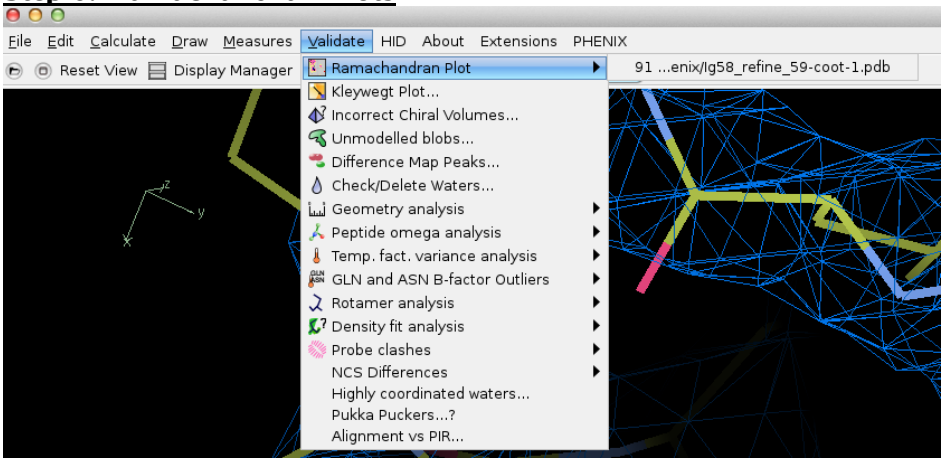

To view the Ramachandran Plot, go to Validate, then Ramachandran Plot, then click on the .pdb file that you would like to view in the Ramachandran plot. You need to check the Ramachandran plot before you run the comprehensive validation because to have a good structure meaning that all the amino acids are in the pink regions on the Ramachandran plot.

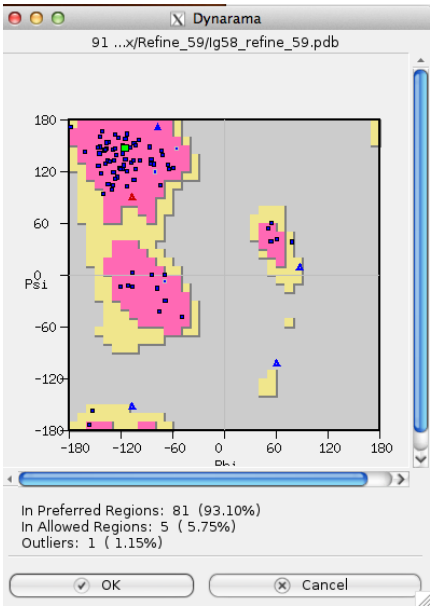

As shown in the Ramachandran plot, all the residues need to be in the pink regions (ideally). If they are not you need to move the residue into the pink region, or at least the yellow region. When hovering your mouse over a square or triangle, it will show which amino acid that shape relates to. Those amino acids with squares have different Ramachandran favored regions than those with triangles.

For a structure to be considered good, you need to have zero "Ramachandran outliers" and minimal "in allowed regions" (maximum in "favored" regions). Once you have checked this plot than you can go forward with validating your structure.

A red shape means that the amino acid is a Ramachandran outlier, and should be fixed. A blue shape means that the amino acid is not an outlier, although it may or may not be in the favored region. A green shape represents the amino acid you currently have your screen's focus on. Note that fixing an amino acid may involve moving the amino acids immediately before and after it. To fix or move an amino acid's configuration, you can use the 'Real Space Refine Zone,' 'Regularize Zone,' or 'Edit Backbone Torsions.' All of these can be found on the right side of the Coot window, and 'Edit Backbone Torsions' may be the most helpful.

Step 7: Edit Backbone Torsions

Once in the 'Edit Backbone Torsions' window, you can either rotate from the peptide or the carbonyl. Note that this will change the Ramachandran plot for both the amino acid you are rotating and the one(s) around it. Try to get both shapes in the desired pink region, but make sure that they stay within the electron density.

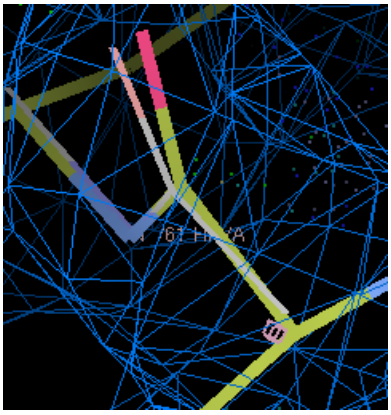

Step…: Check/Delete Waters

When you have refined a structure using the 'Update Waters' feature in the refinement settings, the program will place waters in spots they do not actually belong. One way to check whether or not these are likely water spaces, click on 'Validate,' then on 'Check/Delete Waters' and 'OK.' This will bring up a small window in which questionable waters are displayed. Check to see if the waters in these spots are too close or have too small of an electron density to constitute true waters. Note that there may be more incorrect waters than those in the questionable water window and that not all of the questionable waters may be incorrect. Use your best abilities to discern whether or not there should be waters in each place.

Back to Phenix: Generating Table 1

Step 0: Opening Table 1

On the Phenix home page, navigate to the project you for which you wish to generate a Table 1. This will give you many values of your structure, including the Rfree, Rwork, correlation coefficient, resolution, and percent completeness. Under the 'Utilities' tab on the Phenix homepage, click 'Generate "Table 1" for journal.' Under the 'Options' tab that pop up, make sure that 'CSV' is checked. A .csv file is compatible with Excel and will allow you to view it there. In the 'Structure data' tab, designate the .pdb file, .mtz file, and unmerged data.

Step 1: Unmerge Data

To get an unmerged file of your data, you will need to run HKL2000 again on that project. Run HKL2000 normally as you did before. Then, after you have scaled your sets (you may want to put these output files into a different folder or name them something different to tell the difference between your previous ones), go to the 'Macros' tab and input the follow macro to both the 'During Integration' and 'During Scaling' lines: no merge original index You will have to click 'Add Macro' when done.

Then, delete the rejection file and re-scale your sets. You will get a message that says something along the lines of 'unable to read file… may be because of no merge.' This is fine since you did ask HKL to not merge.

Step 2: Using Multiple Data Sets

If you had more than one data set for this project, you will again have to run HKL twice and get two unmerged output files. Like before, you will merge them using CCP4.

Open CCP4 and open 'Symmetry, Scale, Merge (Aimless).' Then, in the Aimless window, make sure that 'Option to skip scaling and just merge,' 'Customize output options,' 'Assign to the same dataset as the previous file,' and 'Cell Dimensions' are checked. Change 'Input reflection file type' to 'Scalepack file.' Change 'MTZ Output' to 'scaled, unmerged & no outliers' and change 'Scalepack Output' to 'No output.' You should have SCA #1 and SCA #2 available for input. Choose your files, set your cell dimensions, and click 'Run' and 'Run Now.'

This will be the 'Unmerged data' file in Phenix for generating the Table 1.

Step 3: .pdb and .mtz for Table 1

Your .pdb file will be that of your best refinement. The .mtz file will be the data.mtz file that you used to refine your .pdb file against. If you can't remember which ones these were, you can view it by doing the following. Under the 'Job history' tab of Phenix home, double click your best refinement. Under 'Configure,' you can see the files that Phenix used to refine.

Appendix C: Tutorial on How to Make Publication Quality Images in PyMOL

Command	Description
Color grey50, map	Colors the electron density map grey
Set mesh_width, 0.5	Sets the width of the electron density map mesh
Bg_color white	Sets the background color to white
Set ray_trace_fog, 0	Turns off fog
Set depth_cue, 0	Turns off depth cues
Ray	Produces a rayed image
Ray 1024, 1024	Produces a rayed image of size 1024x1024

References

Ackermann, MA; Shriver, M; Perry, NA; Hu, LR; Kontrogianni-Konstantopoulos, A (2014). Obscurins: Goliaths and Davids Take Over Non-muscle Tissues. PLoS ONE, 9(2), 1-18.

Afonine, PV; Grosse-Kunstleve, RW; Echols, N; Headd, JJ; Moriarty, NW; Mustyakimov, M; Terwilliger, TC; Urzhumtsev, A; Zwart, PH; Adams PD (2012). Towards Automated Crystallographic Structure Refinement with Phenix.Refine. *Acta Crystallogr. D Biol. Crystallogr.*, 68(Pt 4), 352-367.

Arimura, T; Matsumoto, Y; Okazaki, O; Hayashi, T; Takahashi, M; Inagaki, N; Hinohara, K; Ashizawa, N; Yano, K; Kimura, A (2007). Structural Analysis of Obscurin Gene in Hypertrophic Cardiomyopathy. Biochem. Biophys. Res. Commun., 362(2), 281-287.

Armani, A; Galli, S; Giacomello, E; Bagnato, P; Barone, V; Rossi, D; Sorrentino, V (2006). Molecular Interactions with Obscurin are involved in the Localization of Muscle-specific Small Ankyrin1 Isoforms to Subcompartments of the Sarcoplasmic Reticulum. *Exp. Cell. Res*., 312(18), 3458-3465.

Bang, ML; Centner, T; Fornoff, F; Geach, AJ; Gotthardt, M; McNabb, M; Witt, CC; Labeit, D; Gregorio, CC; Granzier, H; Labeit, S (2001). The Complete Gene Sequence of Titin, Expression of an Unusual Approximately 700-kDa Titin Isoform, and its Interaction with Obscurin Identify a Novel Z-line to I-band Linking System. *Circ. Res.*, 89(11), 1065-1072.

Case, DA; Darden, TA; Cheatham, TE, 3rd; Simmerling, CL; Wang, J; Duke, RE; Luo, R; Walker, RC; Zhang, W; Merz, KM; Roberts, B; Hayik, S; Roitberg, A; Seabra, G; Swails, J; Goetz, AW; Kolossváry, I; Wong, KF; Paesani, F; Vanicek, J; Wolf, RM; Liu, J; Wu, X; Brozell, SR; Steinbrecher, T; Gohlke, H; Cai, Q; Ye, X; Wang, J; Hsieh, M-J; Cui, G; Roe, DR; Mathews, DH; Seetin, MG; Salomon-Ferrer, R; Sagui, C; Babin, V; Luchko, T; Gusarov, S; Kovalenko, A; Kollman, PA (2012). AMBER 12. In: University of Califonia SF, Ed. University of Califonia, San Fransisco.

Chauveau, C; Rowell, J; Ferreiro, A (2014). A Rising Titan: TTN Review and Mutation Update. *Hum. Mutat.*, 35(9)1046-1059.

Chen, VB; Arendall, WB, 3rd; Headd, JJ; Keedy, DA; Immormino, RM; Kapral, GJ; Murray, LW; Richardson, JS; Richardson, DC (2010). MolProbity: All-atom Structure Validation for Macromolecular Crystallography. *Acta Crystallogr. D Biol. Crystallogr*., 66(1), 12-21.

Chothia, C and Lesk, AM (1986). The Relation between the Diverge of Sequence and Structure in Proteins. *EMBO J.*, 5(40), 823-826.

Chu, M; Gregorio, CG; and Pappas, CT (2016). Nebulin, a Multi-functional Giant. *J. Exp. Biol*., 219, 146-152.

Cooper, GM (2000). The Cell: A Molecular Approach. 2nd Edition, Actin, Myosin, and Cell Movement. *Sinauer Associates*, Sunderland, MA.

de Groot, BL; van Aalten, DMF; Scheek, RM; Amadei, A; Vriend, G; Berendsen, HJC (1997). Prediction of Protein Conformational Freedom from Distance Constraints. *Proteins* 29, 240-251.
Dessau, MA and Modis, Y (2011). Protein Crystallization for X-ray Crystallography. *JoVE*, 47, 1-6.

Di Cola, E; Waigh, TA; Trinick, J; Tskhovrebova, L; Houmeida, A; Pyckhout-Hintzen, W; Dewhurst, C (2005). Persistence Length of Titin from Rabbit Skeletal Muscles Measured with Scattering and Microrheology Techniques. Biophys. J., 88(6), 4095-4106.

Duff, RM; Tay, V; Hackman, P; Ravenscroft, G; McLean, C; Kennedy, P; Steinbach, A; Schöffler, W; van der Ven, PF; Fürst, DO; Song, J; Djinović-Carugo, K; Penttilä, S; Raheem, O; Reardon, K; Malandrini, A; Gambelli, S; Villanova, M; Nowak, KJ; Williams, DR; Landers, JE; Brown, RH, Jr; Udd, B; Laing, NG (2011). Mutations in the N-terminal Actin-binding Domain of Filamin C Cause a Distal Myopathy. *Am. J. Hum. Genet.*, 88(6), 729-740.

Elliot, P and McKenna, WJ (2004). Hypertrophic Cardiomyopathy. *Lancet*., 363(9424), 1881-1891.

Emsley, P; Lohkamp, B; Scott, WG; Cowtan, K (2010). Features and Development of Coot. Acta Crystallogr. D Biol. Crystallogr., 66(Pt 4), 486-501.

Evilä, A; Vihola, A; Sarparanta, J; Raheem, O; Palmio, J; Sandell, S; Eymard, B; Illa, I; Rojas-Garcia, R; Hankiewicz, K; Negrão, L, Löppönen, T; Nokelainen, P; Kärppä, M; Penttilä, S; Screen, M; Suominen, T; Richard, I; Hackman, P; Udd, B (2014). Atypical Phenotypes in Titinopathies Explained by Second Titin Mutations. *Ann. Neurol*., 75(2), 230-240.

Freiburg, A; Trombitas, K; Hell, W; Cazorla, O; Fougerousse, F; Centner, T; Kolmerer, B; Witt, C; Beckmann, JS; Gregorio, CC; Granzier, H; Labeit, S (2000). Series of Exon-skipping Events in the Elastic Spring Region of Titin as the Structural Basis for Myofibrillar Elastic Diversity. *Circ. Res.*, 86(11), 1114-1121.

Frenneaux, MP (2004). Assessing the Risk of Sudden Cardiac Death in a Patient with Hypertrophic Cardiomyopathy. *Heart*, 90, 570-575.

Fukuzawa, A; Idowu, S; Gautel, M (2005). Complete Human Gene Structure of Obscurin: Implications for Isoform Generation by Differential Splicing. *J. Muscle Res. Cell Motil.*, 26, 427–434.

Fukuzawa, A; Lange, S; Holt, M; Vihola, A; Carmignac, V; Ferreiro, A; Udd, B; Gautel, M (2008). Interactions with Titin and Myomesin Target Obscurin and Obscurin-like 1 to the M-band: Implications for Hereditary Myopathies. *J. Cell. Sci.*, 121(11), 1841-1851.

Garcia, TI; Oberhauser, AF; Braun, W (2009). Mechanical Stability and Differentially Conserved Physical-chemical Properties of Titin Ig-domains. Proteins 75(3), 706-718.

Gautel, M (2011). The Sarcomeric Cytoskeleton: Who Picks Up the Strain? *Curr. Opin. Cell Biol.*, 23(1), 39-46.

Gautel, M; Djinović-Carugo, K (2016). The Sarcomeric Cytoskeleton: From Molecules to Motion. *J. Exp. Biol.*, 219(Pt 2), 135-145.

Gold, MG; Barford, D; Komander, D (2006). Lining the Pockets of Kinases and Phosphatases. *Curr. Opin. Struct. Biol*., 16, 693-701.

Granzier, HL; Labeit, S (2004). The Giant Protein Titin: A Major Player in Myocardial Mechanics, Signaling, and Disease. *Circ. Res.*, 94(3), 284-295.

Granzier, HLM; Wang, K (1993). Passive Tension and Stiffness of Vertebrate Skeletal and Insect Flight Muscles: Contribution of Weak Cross-bridges and Elastic Filaments. *Biophys. J.*, 65, 2141-2159.

Grater, F; Shen, J; Jiang, H; Gautel, M; Grubmuller, H (2005). Mechanically Induced Titin Kinase Activation Studied by the Force-probe Molecular Dynamics Simulations. *Biophys. J.*, 88, 790-804.

Greene, DN; Garcia, T; Sutton, RB; Gernert, KM; Benian, GM (2008). Single-molecule Force Spectroscopy Reveals a Stepwise Unfolding of Caenorhabiditis elegans Giant Protein Kinase Domains. *Biophys. J.*, 95, 1360-1370.

Guergueltcheva, V; Peeters, K; Baets, J; Ceuterick-de Groote, C; Martin, JJ; Suls, A; De Vriendt, E; Mihaylova, V; Chamova, T; Almeida-Souza, L; Ydens, E; Tzekov, C; Hadjidekov, G; Gospodinova, M; Storm, K; Reyniers, E; Bichev, S; van der Ven, PF; Fürst, DO; Mitev, V; Lochmüller, H; Timmerman, V; Tournev, I; De Jonghe, P; Jordanova, A (2011). Distal Myopathy with Upper Limb Predominance Caused by Filamin C Haploinsufficiency. *Neurology*, 77(24), 2105-2114.

Hackman, JP; Vihola, A; Haravuori, H; Marchand, S; Sarparanta, J; De Seze, J; Labiet, S; Witt, C; Peltonen, L; Richard, I; Udd, B (2002). Tibial Muscular Dystrophy is a Titinopathy Caused by Mutations in TTN, the Gene Encoding the Giant Skeletal-Muscle Protein Titin. *Am. J. Hum. Genet.*, 71, 492-500.

Hornak, V; Abel, R; Okur, A; Strockbine, B; Roitberg, A; Simmerling, C (2006). Comparison of multiple Amber force fields and development of improved protein backbone parameters. *Proteins*, 65, 712-725.

Hsin, J; Strumpfer, J; Lee, EH; Schulten, K (2011). Molecular Origin of the Hierarchical Elasticity of Titin: Simulation, Experiment, and Theory. *Annu. Rev. Biophys*., 40, 187-203.

Hu, LR and Kontrogianni-Konstantopoulos, A (2013). The Kinase Domains of Obscurin Interact with Intercellular Adhesion Proteins. *FASEB J.*, 27(5), 2001-2012.

Hu, SH; Parker, MW; Lei, JY; Wilce, MC; Benian, GM; Kemp, BE (1994). Insights into Autoregulation from the Crystal Structure of Twitchin Kinase. *Nature*, 369, 581-584.

Hu, YR; Ackermann, M; Hecker, P; Prosser, B; King, B; O'Connell, K; Asico, L; Jose, P; Wright, N; Lederer, J; Kontrogianni-Konstantopulous, A (2016). A Missense Mutation in the Obscurin Gene Leads to Hypertrophic Cardiomyopathy due to Deregulated Calcium Cycling. *Biophys. J.*, 110, 618a.

Improta, S; Krueger, JK; Gautel, M; Atkinson, RA; Lefevre, JF; Moulton, S; Trewhella, J; Pastore, A (1998). The Assembly of Immunoglobulin-like Modules in Titin: Implications for Muscle Elasticity. *J. Mol. Biol.*, 284, 761-777.

Isralewitz, B; Gao, M; Schulten, K (2001). Steered Molecular Dynamics and Mechanical Functions of Proteins. *Curr. Opin. Struct. Biol.*, 11(2), 224-230.

Johnson, DA; Akamine, P; Radzio-Andzelm, E; Madhusudan, M; Taylor, SS (2001). Dynamics of cAMP-dependent Protein Kinase. *Chem. Rev.*, 101, 2243-2270.
Kley, RA; Serdaroglu-Oflazer, P; Leber, Y; Odgerel, Z; van der Ven, PF; Olivé, M; Ferrer, I; Onipe, A; Mihaylov, M; Bilbao, JM; Lee, HS; Höhfeld, J; Djinović-Carugo, K; Kong, K; Tegenthoff, M; Peters, SA; Stenzel, W; Vorgerd, M; Goldfarb, LG; Fürst, DO (2012). Pathophysiology of Protein Aggregation and Extended Phenotyping in Filaminopathy. *Brain*, 135(Pt 9), 2642-2660.

Kobe, B; Heierhorst, J; Feil, SC; Parker, MW; Benian, GM; Weiss, KR; Kemp, BE (1996). Giant Protein Kinases: Domain Interactions and Structural Basis of Autoregulation. *EMBO J.*, 15, 6810-6821.

Kontrogianni-Konstantopoulos, A and Bloch, RJ (2005). Obscurin: A Multitasking Muscle Giant. *J. Muscle Res. Cell Motil.*, 26(6-8), 419-426.

Kontrogianni-Konstantopoulos, A; Ackermann, MA; Bowmann, AL; Yap, SV; and Bloch, RJ (2009). Muscle Giants: Molecular Scaffolds in Sarcomerogenesis. *Physiol. Rev.*, 89(4), 1217-1267.

Kopot, A (2014). Contraction of Skeletal Muscle. *AK Lectures*.

Krieger, E; Darden, T; Nabuurs, SB; Finkelstein, A; Vriend, G (2004). Making Optimal Use of Empirical Energy Functions: Force-field Parameterization in Crystal Space. *Proteins*, 57(4), 678−683.

Krieger, E; Vriend, G (2014). YASARA View - Molecular Graphics for All Devices - from Smartphones to Workstations. *Bioinformatics*, 30(20), 2981-2982.

Lee, EH; Hsin, J; Mayans, O; Schulten, K (2007). Secondary and Tertiary Structure Elasticity of Titin Z1Z2 and a Titin Chain Model. *Biophys. J.*, 93(5), 1719-1735.

Lee, W; Tonelli, M; Markley, JL (2015). NMRFAM-SPARKY: Enhanced Software for Biomolecular NMR Spectroscopy. Bioinformatics, 31, 1325-1327.

Li, H and Fernandez, JM (2003). Mechanical Design of the First Proximal Ig Domain of Human Cardiac Titin Revealed by Single Molecule Force Spectroscopy. *J. Mol. Biol.*, 334(1), 75-86.
Li, H; Linke, WA; Oberhauser, AF; Carrion-Vazquez, M; Kerkvliet, JG; Lu, H; Marszalek, PE; Fernandez, JM (2002). Reverse Engineering of the Giant Muscle Protein Titin. *Nature*, 418, 998-1002.

Linke, WA (2000). Stretching Molecular Springs: Elasticity of Titin Filaments in Vertebrate Striated Muscle. *Histol. Histopathol.,* 15(3), 799-811.

Linke, WA (2000). Titin Elasticity in the Context of the Sarcomere: Force and Extensibility Measurements on Single Myofibrils. *Avd. Exp. Med. Biol.*, 481, 179-202; discussion 203-176.

Linke, WA (2008). Sense and Stretchability: The Role of Titin and Titin-associated Proteins in Myocardial Stress-sensing and Mechanical Dysfunction. *Cardiovasc. Res.*, 77, 637-648.

Linke, WA; Popov, VI; Pollack, GH (1994). Passive and Active Tension in Single Cardiac Myofibrils. *Biophys. J.*, 67, 782-792.

Löwe, T; Kley, RA; van der Ven, PF; Himmel, M; Huebner, A; Vorgerd, M; Fürst, DO (2007). The Pathomechanism of Filaminopathy: Altered Biochemical Properties Explain the Cellular Phenotype of a Protein Aggregation Myopathy. *Hum. Mol. Genet.,* 16(11), 1351-1358.

Luan, X; Hong, D; Zhang, W; Wang, Z; Yuan, Y (2010). A Novel Heterozygous Deletion-insertion Mutation (2695-2712 del/GTTTGT ins) in Exon 18 of the Filamin C Gene Causes Filaminopathy in a Large Chinese Family. *Neuromuscul. Disord.,* 20(6), 390-396.

Ma, K; Kan, L; Wang, K (2001). Polyproline II Helix is a Key Structural Motif of the Elastic PEVK Segment of Titin. *Biochemistry*, 40(12), 3427-3438.

Ma, K; Wang, K (2003). Malleable Conformation of the Elastic PEVK Segment of Titin: Non-co-operative Interconversion of Polyproline II Helix, Beta-turn and Unordered Structures. *Biochem. J.*, 374(Pt 3), 687-695.

Marchetti, S; Sbrana, F; Toscano, A; Fratini, E; Carla, M; Vassalli, M; Tiribilli, B; Pacini, A; Gambi, CM (2011). Beta-connectin Studies by Small-angle X-ray Scattering and Single-molecule Force Spectroscopy by Atomic Force Microscopy. *Phys. Rev. E Stat. Nonlin. Soft Matter Phys.*, 83(5 Pt 1), 051919.

Marino, M; Zou, P; Svergun, D; Garcia, P; Edlich, C; Simon, B; Wilmanns, M; Muhle-Goll, C; Mayans, O (2006). The Ig Doublet Z1Z2: a Model System for the Hybrid Analysis of Conformational Dynamics in Ig Tandems from Titin. *Structure*, 14(9), 1437-1447.

Marston, S; Montgiraud, C; Munster, AB; Copeland, O; Choi, O; Dos Remedios, C; Messer, AE; Ehler, E; Knöll, R (2015). OBSCN Mutations Associated with Dilated Cardiomyopathy and Haploinsufficiency. *PLoS One,* 10(9), e0138568.

Mastaglia, FL; Laing, NG (1999). Distal Myopathies: Clinical and Molecular Diagnosis and Classification. *J. Neurol. Neurosurg. Psychiatry.*, 67(6), 703-707.

Mastersona, LR; Masterson, LR; Shi, L; Metcalfe, E; Gao, J; Taylor, SS; Veglia, G (2011). Dynamically Committed, Uncommitted, and Quenched States Encoded in Protein Kinase A Revealed by NMR Spectroscopy. *Proc. Natl. Acad. Sci. U.S.A.*, 108, 6969-6974.

Matsubara, S; Maruyama, K (1977). Role of Connectin in the Length-tension Relation of Skeletal and Cardiac Muscles. *Jpn J. Physiol.,* 27(5), 589-600.

Mayans, O; Benian, GM; Simkovic, F; Rigden, DJ (2012). Mechanistic and Functional Diversity in the Mechanosensory Kinases of the Titin-like Family. Biochem. Soc. Trans., 41(Pt 4), 1066-71.

Mayans, O; van der Ven, PFM; Wilm, M; Mues, A; Young, P; Fürst, DO; Wilmanns, M; Gautel, M (1998). Structural Basis for Activation of the Titin Kinase Domain during Myofibrillogenesis. *Nature,* 395, 863-869.

McNally, EM and Pytel, P (2007). Muscle Diseases: the Muscular Dystrophies. *Annu. Rev. Pathol*., 2, 87-109.

Meyer, LC and Wright, NT (2003). Structure of Giant Muscle Proteins. *Front. Physiol.,* 4, 368, 1-12.

Muntoni, F; Wells, D (2007). Genetic Treatments in Muscular Dystrophies. *Curr. Opin. Neurol.*, 20(5), 590-594.

Nagase, T; Kikuno, R; Hattori, A; Kondo, Y; Okumura K, Ohara, O (2000). Prediction of the Coding Sequences of Unidentified Human Genes. XIX. The Complete Sequences of 100 New cDNA Clones from Brain which Code for Large Proteins *in vitro*. *DNA Res*., 7, 347–355.

Nagase, T; Kikuno, R; Ishikawa, KI; Hirosawa, M; Ohara, O (2000). Prediction of the Coding Sequences of Unidentified Human Genes. XVI. The Complete Sequences of 150 New cDNA Clones from Brain which Code for Large Proteins *in vitro*. *DNA Res*., 7, 65-73.

Nagase, T; Kikuno, R; Nakayama, M; Hirosawa, M; Ohara, O (2000). Prediction of the Coding Sequences of Unidentified Human Genes. XVIII. The Complete Sequences of 100 New cDNA Clones from Brain which Code for Large Proteins *in vitro*. *DNA Res*., 7, 273-281.

Ng, R; Banks, GB; Hall, JK; Muir, LA; Ramos, JN; Wicki, J; Odom, GL; Konieczny, P; Seto, J; Chamberlain, JR; Chamberlain, JS (2012). Animal Models of Muscular dystrophy. *Prog. Mol. Biol. Transl. Sci*., 105, 83-111.

Nguyen, H; Roe, DR; Simmerling, C (2013). Improved Generalized Born Solvent Model Parameters for Protein Simulations. J. Chem. Theory Comput., 9(4), 2020-2034.

Otwinowski, Z; Minor, W (1997). Processing of X-ray Diffraction Data Collected in Oscillation Mode. *Methods Enzymol*., 276, 307-326.

Pernigo, S; Fukuzawa, A; Bertz, M; Holt, M; Rief, M; Steiner, RA; Gautel, M (2010). Structural Insight into M-band Assembly and Mechanics from the Titin-obscurin-like-1 complex. *Proc. Natl. Acad. Sci. USA*, 107(7), 2908-2913.

Perry, NA; Vitolo, MI; Martin, SS; Kontrogianni-Konstantopoulos, A (2014). Loss of Obscurin-RhoGEF Downregulates RhoA Signaling and Increases Microtentacle Formation and Attachment of Breast Epithelial Cells. *Oncotarget*, 5(18), 8558-8568.

Puchner, EM and Gaub, HE (2010). Exploring the Conformation-regulated Function of Titin Kinase by Mechanical Pump and Probe Experiments with Single Molecules. *Angew. Chem. Int. Ed*., 49, 1147-1150.

Puchner, EM; Alexandrovich, A; Kho, AL; Hensen, U; Schafer, LV; Brandmeier, B; Grater, F; Grubmuller, H; Gaub, HE; Gautel, M (2008). Mechanoenzymatics of Titin Kinase. *Proc. Natl., Acad. Sci. U.S.A.*, 105, 13385-13390.

Randazzo, D; Blaauw, B; Paolini, C; Pierantozzi, E; Spinozzi, S; Lange, S; Chen, J; Protasi, F; Reggiani, C; Sorrentino, V (2017). Exercise-induced Alterations and Loss of Sarcomeric M-line Organization in the Diaphragm Muscle of Obscurin Knockout Mice. *Am. J. Physiol. Cell. Physiol.*, 312(1), C16-C28.

Randazzo, D; Giacomello, E; Lorenzini, S; Rossi, D; Pierantozzi, E; Blaauw, B; Reggiani, C; Lange, S; Peter, AK; Chen, J; Sorrentino, V (2013). Obscurin is Required for AnkyrinB-dependent Dystrophin Localization and Sarcolemma Integrity. *J. Cell. Biol.*, 200(4), 523-536.

Razinia, Z; Mäkelä, T; Ylänne, J; Calderwood, DA (2012). Filamins in Mechanosensing and Signaling. *Annu. Rev. Biophys.*, 41, 227-46.

Rhodes, G (2006). Crystallography Made Crystal Clear, Third Edition. *Elsevier Inc.*, Burlington, MA.

Rief, M; Gautel, M; Gaub, HE (2000). Unfolding Forces of Titin and Fibronectin Domains Directly Measured by AFM. *Adv. Exp. Med. Biol*., 481:129-136; discussion 137-141.

Rossi, D; Bencini, C; Maritati, M; Benini, F; Lorenzini, S; Pierantozzi, E; Scarcella, AM; Paolini, C; Protasi, F; Sorrentino, V (2014). Distinct Regions of Triadin are Required for Targeting and Retention at the Junctional Domain of the Sarcoplasmic Reticulum. *Biochem. J.*, 458(2), 407-417.

Rossi, D; Palmio, J; Evila, A; Galli, L; Barone, V; Caldwell, TA; Policke, RA; Berndsen, CE; Wright, NT; Romero, N; Malfatti, E; Brochier, G; Stokkovic, T; Jordanova, A; Guergueltcheva, A; Hackman, P; Romero, NB; Eymard, B; Udd, B; Sorrentino, V (submitted). Digenic Inheritance of a FLNC Frameshift and an OBSCN Variant in a Family with Distal Muscular Dystrophy.

Rossi, D; Vezzani, B; Galli, L; Paolini, C; Toniolo, L; Pierantozzi, E; Spinozzi, S; Barone, V; Pegoraro, E; Bello, L; Cenacchi, G; Vattemi, G; Tomelleri, G; Ricci, G; Siciliano, G; Protasi, F; Reggiani, C; Sorrentino, V (2014). A Mutation in the CASQ1 Gene Causes a Vacuolar Myopathy with Accumulation of Sarcoplasmic Reticulum Protein Aggregates. *Hum. Mutat.*, 35(10), 1163-1170.

Rudloff, MW; Woosley, AN; Wright, NT (2015). Biophysical Characterization of Naturally Occurring Titin M10 Mutations. *Protein Sci.*, 24(6), 946-955.

Rupp, B (2010). Biomolecular Crytallography. Garland Science, Taylor and Francis Group, New York, New York.

Russell, MW; Raeker, MO; Korytkowski, KA; Sonneman, KJ (2002). Identification, Tissue Expression and Chromosomal Localization of Obscurin-MLCK, a Member of the Titin and Dbl Families of Myosin Light Chain Kinases. *Gene.*, 282, 237-246.

Satoh, M; Takahashi, M; Sakamoto, T; Hiroe, M; Marumo, F; Kimura, A (1999). Structural Analysis of the Titin Gene in Hypertrophic Cardiomyopathy: Identification of a Novel Disease Gene. *Biochem. Biophys. Res. Commun.*, 262, 411-417.

Scapin, G (2013). Molecular Replacement Then and Now. *Acta. Crystallogr. D. Biol. Crystallogr.*, 69(11), 2266-2275.

Sewry, CA (2010). Muscular Dystrophies: An Update on Pathology and Diagnosis. *Acta Neuropathol.*, 120(3), 343-358.

Shatunov, A; Olivé, M; Odgerel, Z; Stadelmann-Nessler, C; Irlbacher, K; van Landeghem, F; Bayarsaikhan, M; Lee, HS; Goudeau, B; Chinnery, PF; Straub, V; Hilton-Jones, D; Damian, MS; Kaminska, A; Vicart, P; Bushby, K; Dalakas, MC; Sambuughin, N; Ferrer, I; Goebel, HH; Goldfarb, LG (2009). In-frame Deletion in the Seventh Immunoglobulin-like Repeat of Filamin C in a Family with Myofibrillar Myopathy. *Eur. J. Hum. Genet.*, 17(5), 656-663.

Shen, Y; Delaglio, F; Cornilescu, G; Bax, A (2009). TALOS+: A Hybrid Method for Predicting Protein Backbone Torsion Angles from NMR Chemical Shifts *J. Biomol. NMR,* 44(4), 213-223.

Shriver, M; Marimuthu, S; Paul, C; Geist, J; Seale, T; Konstantopoulos, K; Kontrogianni-Konstantopoulos, A (2016). Giant Obscurins Regulate the PI3K Cascade in Breast Epithelial Cells via Direct Binding to the PI3K/p85 Regulatory Subunit. *Oncotarget,* 7(29), 45414-45428.

Sjoblom, T.; Jones, S.; Wood, L. D.; Parsons, D. W.; Lin, J.; Barber, T. D.; Mandelker, D.; Leary, R. J.; Ptak, J.; Silliman, N.; Szabo, S.; Buckhaults, P.; Farrell, C.; Meeh, P.; Markowitz, S. D.; Willis, J.; Dawson, D.; Willson, J. K.; Gazdar, A. F.; Hartigan, J.; Wu, L.; Liu, C.; Parmigiani, G.; Park, B. H.; Bachman, K. E.; Papadopoulos, N.; Vogelstein, B.; Kinzler, K. W.; Velculescu, V. E (2006). The Consensus Coding Sequences of Human Breast and Colorectal Cancers. *Science*, 314 (5797), 268-74.

Stacklies, W; Vega, MC; Wilmanns, M; Grater, F (2009). Mechanical Network in Titin Immunoglobulin from Force Distribution Analysis. *PLoS Comput. Biol*., 5(3), e1000306.
Stahl, SW; Puchner, EM; Alexandrovich, A; Gautel, M; Gaub, HE (2011). A Conditional Gating Mechanism Assures the Integrity of the Molecular Force-sensor Titin Kinase. *Biophys. J*., 101, 1978-1986.

Stroka, KM; Wong, BS; Shriver, M; Phillip, JM; Wirtz, D; Kontrogianni-Konstantopoulos, A; Konstantopoulos, K (2016). Loss of Giant Obscurins Alters Breast Epithelian Cell Mechanosensing of Matrix Stiffness. *Oncotarget*, Advanced Publications, 1-17.

Tsai, CJ; Nussinov, R (2013). The Molecular Basis of Targeting Protein Kinases in Cancer Therapeutics. *Semin. Cancer Biol*., 23(4), 235-242.

Teekakirikul, P; Padera, RF; Seidman, JG; Seidman, CE (2012). Hypertrophic Cardiomyopathy: Translating Cellular Cross Talk into Therapeutics. J. Cell. Biol., 199(3), 417-421.

Terwilliger, TC; Grosse-Kunstleve, RW; Afonine, PV; Moriarty, NW; Zwart, PH; Hung, LW; Read, RJ; Adams, PD (2008). Iterative Model Building, Structure Refinement and Density Modification with the PHENIX AutoBuild Wizard. *Acta Crystallogr. D Biol. Crystallogr.*, 64(1), 61-69.

The PyMOL Molecular Graphics System, Version 1.3 Schrödinger, LLC.
Trinick, J (1992). Understanding the Functions of Titin and Nebulin. *FEBS Lett.*, 307(1), 44-48.

Udd, B (2012). Distal Myopathies- New Genetic Entities Expand Diagnostic Challenge. *Neuromuscul. Disord.*, 22(1), 5-12.

Udd, B; Griggs, R (2001). Distal Myopathies. *Curr. Opin. Neurol*., 14, 561-566.

van Zundert, GCP; Rodrigues, JPGLM; Trellet, M; Schmitz, C; Kastritis, PL; Karaca, E; Melquiond, ASJ; de Vries, SJ; Bonvin, AMJJ (2016). The HADDOCK2.2 Web Server: User-friendly Integrative Modeling of Biomolecular Complexes. *J. Mol. Biol*., 428(4), 720-725.

Vazina, AA; Lanina, NF; Alexeev, DG; Bras, W; Dolbnya, IP (2006). The Structural Principles of Multidomain Organization of the Giant Polypeptide Chain of the Muscle Titin Protein: SAXS/WAXS Studies during the Stretching of Oriented Titin Fibres. *J. Struct. Biol.*, 155(2), 251-262.

von Castelmur, E; Marino, M; Svergun, DI; Kreplak, L; Ucurum-Fotiadis, Z; Konarev, PV; Urzhumtsev, A; Labeit, D; Labeit, S; Mayans, O (2008). A Regular Pattern of Ig Super-motifs Defines Segmental Flexibility as the Elastic Mechanism of the Titin Chain. *Proc. Natl. Acad. Sci. U.S.A.*, 105(4), 1186-1191.

Vorgerd, M; van der Ven, PF; Bruchertseifer, V; Löwe, T; Kley, RA; Schröder, R; Lochmüller, H; Himmel, M; Koehler, K; Fürst, DO; Huebner, A (2005). A Mutation in the Dimerization Domain of Filamin C Causes a Novel Type of Autosomal Dominant Myofibrillar Myopathy. *Am. J. Hum. Genet.*, 77(2), 297-304.

Wlodawer, A; Wladek, M; Dauter, Z; Jaskolski, M (2008). Protein Crystallography for Non-crystallographers, or How to Get the Best (but not more) from Published Macromolecular Structures. *FEBS J.*, 275(1), 1-21.

Wlodawer, A; Wladek, M; Dauter, Z; Jaskolski, M (2013). Protein Crystallography for Aspiring Crystallographers or How to Avoid Pitfalls and Traps in Macromolecular Structure Determination. *FEBS J.*, 280(22), 5705-5736.

Wood, L. D.; Parsons, D. W.; Jones, S.; Lin, J.; Sjoblom, T.; Leary, R. J.; Shen, D.; Boca, S. M.; Barber, T.; Ptak, J.; Silliman, N.; Szabo, S.; Dezso, Z.; Ustyanksky, V.; Nikolskaya, T.; Nikolsky, Y.; Karchin, R.; Wilson, P. A.; Kaminker, J. S.; Zhang, Z.; Croshaw, R.; Willis, J.; Dawson, D.; Shipitsin, M.; Willson, J. K.; Sukumar, S.; Polyak, K.; Park, B. H.; Pethiyagoda, C. L.; Pant, P. V.; Ballinger, D. G.; Sparks, A. B.; Hartigan, J.; Smith, D. R.; Suh, E.; Papadopoulos, N.; Buckhaults, P.; Markowitz, S. D.; Parmigiani, G.; Kinzler, K. W.; Velculescu, V. E.; Vogelstein, B (2007). The Genomic Landscapes of Human Breast and Colorectal Cancers. *Science*, 318 (5853), 1108-13.

Wright, NT; Varney, KM; Ellis, KC; Markowitz, J; Gitti, RK; Zimmer, DB; Weber, DJ (2005). The Three-dimensional Solution Structure of Ca(2+)-bound S100A1 as Determined by NMR Spectroscopy. *J. Mol. Biol.*, 353(2), 410-426.

Yang, J; Roy, A; Zhang, Y (2013). Protein-ligand Binding Site Recognition using Complementary Binding-specific Substructure Comparison and Sequence Profile Alignment. *Bioinformatics*, 29(20), 2588-2595.

Young, P; Ehler, E; Gautel, M (2001). Obscurin, a Giant Sarcomeric Rho Guanine Nucleotide Exchange Factor Protein Involved in Sarcomere Assembly. *J. Cell. Biol*., 154, 123-136.

Zheng, W; Chen, H; Deng, X; Yuan, L; Yang, Y; Song, Z; Yang, Z; Wu, Y; Deng, H (2015). Identification of a Novel Mutation in the Titin Gene in a Chinese Family with Limb-Girdle Muscular Dystrophy 2J. *Mol. Neurobiol*., [Epub ahead of print].